Integrated Erbium Lasers in Silicon Photonics

by

Purnawirman

Submitted to the Department of Electrical Engineering and Computer Science
in partial fulfillment of the requirements for the degree of

Doctor of Philosophy

at the

MASSACHUSETTS INSTITUTE OF TECHNOLOGY

February 2017

Signature redacted

Author .....
Department of Electrical Engineering and Computer Science
January 31, 2016

Signature redacted

Certified by .....
Michael R. Watts
Associate Professor
Thesis Supervisor

Signature redacted

Accepted by .....
Leslie A. Kolodziejski
Chair, Department Committee on Graduate Theses

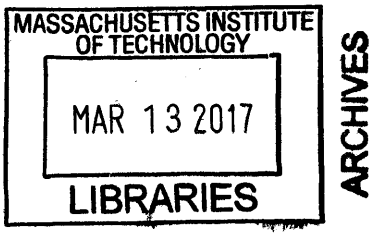

Integrated Erbium Lasers in Silicon Photonics

by

Purnawirman

Submitted to the Department of Electrical Engineering and Computer Science
on January 31, 2016, in partial fulfillment of the
requirements for the degree of
Doctor of Philosophy

Abstract

We present results on the development of integrated erbium-doped aluminum oxide lasers on a silicon photonics platform. A key achievement in this work is a scalable laser design for high output power and ultra-narrow linewidth performance. Using a novel wavelength-insensitive design, a CMOS compatible waveguide structure is proposed to achieve high confinement factor and intensity overlap for both the pump (980 nm) and signal (1550 nm) wavelengths. Laser operation in the C- and L- bands of the erbium gain spectrum is obtained with both a distributed Bragg reflector and a distributed feedback structure. We demonstrate power scaling with output power greater than 75 mW and obtain an ultra-narrow linewidth of 5.3 $\pm$ 0.3 kHz. We investigate the influence of gain film thickness uniformity in distributed feedback laser performance and show a compensation scheme based on a curved cavity design. We then consider the application in optical communications by demonstrating a multi-wavelength cascaded laser to generate wavelength division multiplexing (WDM) light sources. Finally, we propose an integration scheme of laser in full silicon photonics platform by using an erbium trench. The approach is alignment free and allows the erbium-doped film deposition to be the last backend process, providing a pathway to a scalable CMOS compatible laser device.

Thesis Supervisor: Michael R. Watts
Title: Associate Professor

Acknowledgments

I would like to thank Prof. Michael R. Watts as my thesis advisor and for providing funding support for my PhD. He also helped me in the technical design, but more importantly, mentorship for my professional and personal development. He has been very supportive in allowing me to go for several company internships during my stay in MIT. I can not think of anyone who can be a better match for my PhD "style" than Mike, we have developed mutual understanding that goes beyond student and advisor.

I would like to thank Prof. Erich Ippen for serving as my thesis committee member. He provided us with the high power 1480 nm fiber laser for our demonstration of high power scaling. He also served as my RQE committee. I still remember about five years ago, Prof. Ippen is the first MIT professor that I interacted with. I remember I felt nervous whenever we had technical discussion, but he is always been so helpful and unbelievably humble.

I would like to thank Prof. Franz Kaertner for serving as my thesis committee member. Prof. Kaertner provided insightful guidances on the laser and double chirped mirror design. Before coming to MIT, I have read his work on double chirped mirror and was very impressed by the idea. I am very happy that I get the chance to implement the design in integrated photonics platform during my PhD. Like Prof. Ippen, Prof. Kaertner is also very helpful in discussion and I am impressed by his devotion to his work.

I would like to thank Prof. Rajeev Ram for serving as my RQE referee. His comments are very helpful in shaping the research direction, and it is not uncommon for me to find plenty of resources from his lab and group members.

I would like to thank Ehsan Shah Hosseini, Jie Sun, and Jonathan Bradley. In the first two years of my PhD work, they have provided great mentorships on the fundamental of photonics. I remember spending many hours bugging Ehsan and Jie so that I can learn more about electromagnetic waves concept. I really appreciate your patience. Jonathan has passed his knowledge about erbium laser from his PhD

work, and he is probably the only person that has carefully read all my papers and publications. Their roles are monumental for the foundation of my PhD work, without them, I would have a hard time figuring things out on my own.

Michele Moresco and Ben Moss for their help in organizing the tape out.Together with CNSE at Albany, they are always so patient in catering my sometimes funky design.

Anna Baldycheva, Salih Magden, and Nanxi Li for their help in fabrication. Fabrication work is a tedious task that requires long hours dedication and commitment. I truly appreciate their roles and contributions, it allows me to focus on the "fun" part of the work, the design and experiment.

Gurpreet Singh for his contribution in resonant pumping scheme and laser simulation. He and Nanxi helped me tremendously in most of the later chapters in this PhD thesis. I thank both of them for their full trust in my unconventional approach, I'm really glad most of them worked out! It would have been impossible for me to finish my PhD in a high note without you guys.

Erman Timurdogan and Zhan Su for their contribution in ring resonator design and microdisk laser. I admire their work ethic and contribution to the group. Starting the PhD about the same time, they are both strong and competitive colleagues that has inspired me to keep my pace up.

Patrick Callahan for his contribution in double chirped mirror measurement. I have been involved in early mode locked laser design that Patrick is leading now. We had good discussions and exchanged some resources that has helped me in my project.

Cheryl Sorace and Katia Shtyrkova for their work in mode locked laser that inspire some of my own laser design.

I would also like to extend my gratitude to members and alumni of the photonics group. For new members, Diedrik Vermeulen, Chris Poulton, Manan Raval and Matthew Bird, good luck in the next coming years in MIT. Alumni, Christos Samolis, David Cole, Sasha Biberman, Brad Cordova, Matteo Cherchi, Ami Yaacobi, and Jerry Zhou for making the stay in MIT a diverse and wonderful experience.

Dave and Ami has been always a great mentor, like a big brother to talk to. They have helped me in sharing their experiences in thesis preparation. Brad for being an amazing friend and roomate, providing me a smooth transition to life in United States. Jerry for sharing many WWE videos and fun office mate. I wish you guys good luck for all your future endeavors.

I would like to thank Prof. Phua Poh Boon for his guidance. Without him, I probably would not have come to MIT in the first place. He is an inspiring mentor and a role model for a family guy. I remember his advice on writing acknowledgement section to be as candid as possible. This is my candid response, thank you for everything you have done! I hope I can pay it forward to the next generation one day.

I would like to thank folks and companies that has given me internship opportunities during my PhD. Compass Engineering in Singapore have provided an interesting externship experience. Jason Orcutt and IBM Silicon Photonics group have given me a taste of silicon photonics industry experience. Some of the work with Jason has inspired the double chirped mirror design. Brad and TrueMotion have given me opportunity on to work on internet startups. It also opens the door for wider career choices for me. Henry Tan and Microsoft Research team have given me the opportunity to work with world leading software engineers. All of these opportunities would be an integral and unforgettable part of my stay in MIT.

Lastly, I would like to thank my friends and family that have always been supporting me. I won't name each of you, you know who you are. You have stayed with me through ups and downs. I really appreciate it. This work is dedicated to you all.

Contents

List of Figures

Chapter 1

Introduction

We present an introduction to our work on the development of integrated erbium doped aluminum oxide (Al_2O_3:Er^{3+}) laser. We discuss the motivation of Al_2O_3:Er^{3+}as silicon photonics light source and provide a review of the development. Lastly, a guideline for designing Al_2O_3:Er^{3+}laser is calculated from rate equation modeling.

1.1 Motivation

The development of silicon photonics technology has been rapid in these recent years. The premise of silicon photonics is that silicon would provide the most mature integration technology and product platform. Tremendous amount of research and development can be observed not only in academic setting, but also in industry environment [1, 2]. Throughout the course of my PhD work in MIT, I have come across many annual meetings, DARPA fundings, and a strong collaboration effort from many groups and institutions. Several references [3, 4, 5, 6] have provide comprehensive views on the feasibility of the technology. Here, we highlight three examples of application of silicon photonics that we pursue in our group.

Figure 1-1 shows the schematic of on-chip microwave signal oscillators proposed by MIT team for Electronic-Photonic Heterogeneous Integration (EPHI) project [7], a research supported by DARPA. The project goal is to develop chip-scale electronic-photonic/mixed-signal integrated circuits on a common silicon substrate. The pro-

posed platform combine the CMOS electronic components and photonics integrated circuit by using common substrate (Silicon). The integrated photonics components include a low phase noise continuous-wave (CW) distributed feedback (DFB) laser master oscillator and a mode-locked laser (MLL) frequency divider to achieve ultra-low phase noise microwave carrier in an integrated, low-power, vibration immune and highly manufacturable silicon photonic platform. This could enable complex microphotonic coherent systems, such as chip-size optically enabled RADAR front end.

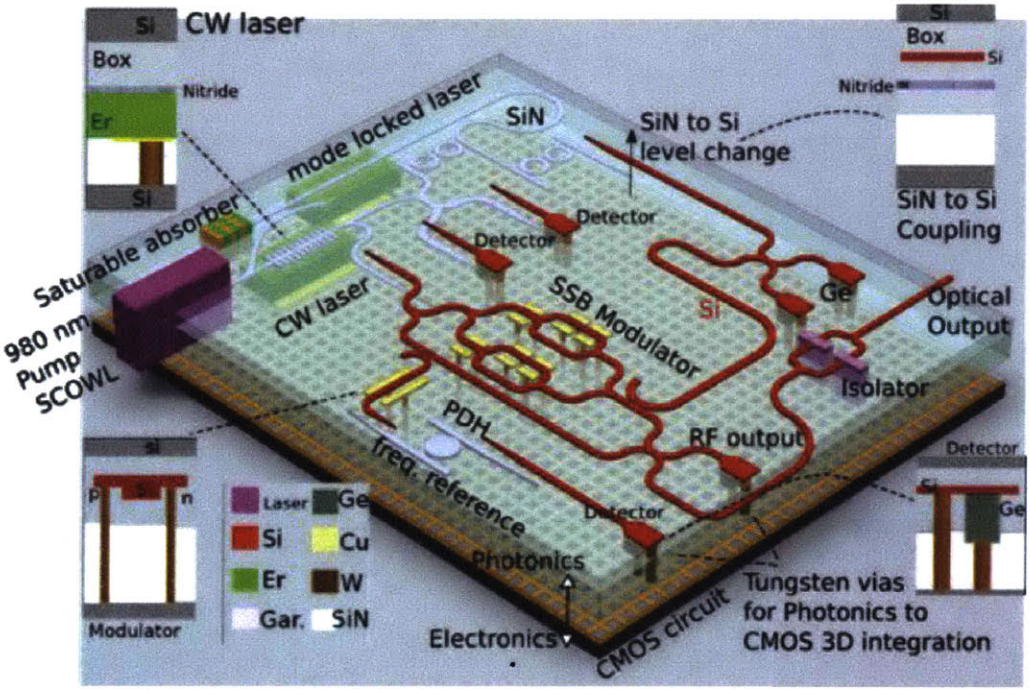

Figure 1-1: Schematic of on-chip microwave signal oscillators proposed by MIT team for Electronic-Photonic Heterogeneous Integration (EPHI) project. The project goal is to develop chip-scale electronic-photonic/mixed-signal integrated circuits on a common silicon substrate.

Figure 1-2 shows the schematic of on-chip optical clock proposed by MIT team for Direct On-Chip Digital Optical Synthesizer (DODOS) project [8]. The project goal is to create technological revolution in optical frequency control. The proposed platform utilizes a high peak power short-pulse (100−−200 fs) generator with a repetition rate locked to the microwave clock to seed a Kerr nonlinear mixer and generate an octave-spanning comb. The long-wavelength end of the comb is then filtered out, frequency

doubled, and locked to the short-wavelength region of the comb, fixing the carrier-envelope-offset (CEO) and ensuring that the microwave source represents the only reference in the system. The final output is generated by locking an on-chip C-band tunable laser to the comb and generating frequencies in-between the comb lines using a microwave synthesizer coupled to a single-side-band (SSB) modulator.

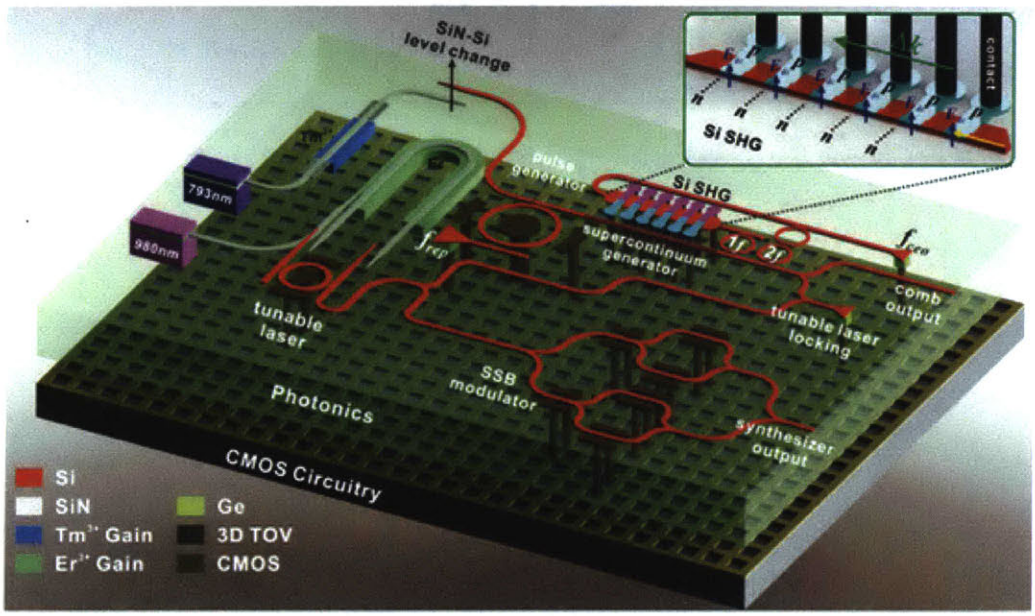

Figure 1-2: Schematic of on-chip optical clock proposed by MIT team for Direct On-Chip Digital Optical Synthesizer (DODOS) project. The project goal is to create technological revolution in optical frequency control.

Lastly, figure 1-3 shows the schematic of the optical transmitter and receiver for the application in communications. The transmitter consists of multi-wavelengths light source that can be independently modulated by modulator driver to transmit information in parallel. The receiver end consists of filters and detectors to decode those independent optical frequencies. This platform hold the promise for application in next generation low-energy, high-speed computing and communication systems.

Thus, silicon photonics platform provide an obvious evolution of optical technology. The general trend of the innovation lies in the strength of silicon photonics to be scalable, chip-sized, and still maintaining high quality performance. One of the most important components that enable all these applications is the integrated light souce. The common requirements of the light source are the **scalability, high power, and**

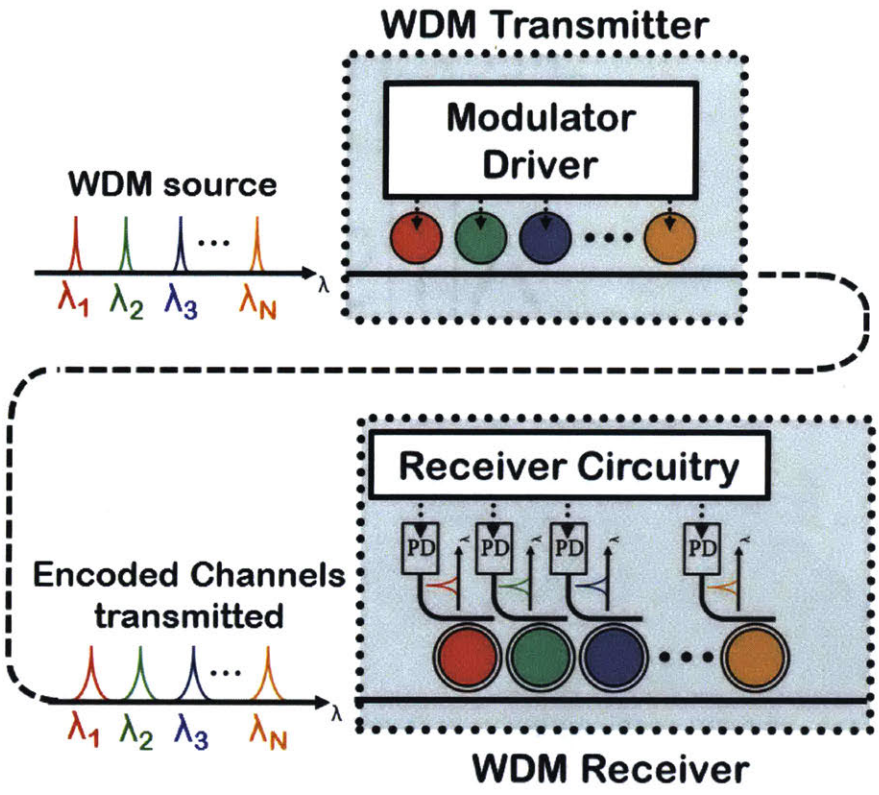

Figure 1-3: Schematic of optical interconnects architecture in silicon photonics platform. The transmitter consists of WDM light source that can be independently modulated. The receiver consists of filters and detectors to decode the independent optical frequencies.

low phase noise/ultra-narrow linewidth source. In the next section, we would provide a review on the integrated silicon photonics light source.

1.2 Literature review on on-chip lasers

Integrated lasers in a silicon photonics platform have been intensively researched because silicon itself is a poor light emitter [9]. Several methods have been applied to realize integrated lasers, including Germanium-on-Silicon heterojunctions [10], hybrid integration with III-V semiconductor materials [11], stimulated Raman scattering [12] and erbium-doped glass on silicon [13].

Of these approaches, hybrid III-V laser approach is undoubtedly the most pop-

ular integrated light source in silicon platform. First demonstrated in UC Santa Barbara, hybrid III-V laser has the advantage of electrically pumped, high gain, and well studied approach with large amount of both silicon and III-V photonics community support. However, hybrid III-V lasers suffer from complex fabrication process with yield challenges, expensive temperature management cost, and amplitude-phase coupling in high gain structure [14]. Figure 1-4a shows one of the hybrid III-V laser approach reproduced from reference [15].

Erbium-doped glass laser on the other hand provides a promising alternative for high performance integrated light source. One of the major concern of integrated erbium laser is the necessity of an optical pump, but an alternative view is to integrate the high quality erbium laser in complement with hybrid III-V laser (e.g. as pump source). The laser can be monolithically integrated in a compatible process with only a single backend deposition required. Figure 1-4b illustrates the structure of Al_2O_3:Er^{3+}laser in silicon photonics platform.

Previously, Al_2O_3:Er^{3+}laser has been demonstrated in racetrack [16] and distributed feedback (DFB) lasers [17]. While the gain medium has been co-sputtered [18] onto oxidized silicon wafers with relatively low loss and a broad gain spectrum, the waveguide design faces some challenges for scaling. Figures 1-5 show the channel and ridge waveguide designed by group in University of Twente. In both designs, the gain medium requires an extra etching step that is hard to be incorporated in CMOS compatible process. In addition, to form the Bragg grating (not shown here), the process includes the interference lithography that is unscalable for wafer processing.

In this work, we demonstrate a design that minimizes the Al_2O_3:Er^{3+}layer process to only a single backend deposition process. This still holds true even for a more complicated layer (chapter 5 and chapter 6), where we substitute the isolation of the Al_2O_3:Er^{3+}layer by constructing a erbium trench in CMOS compatible process. We show a scalable design of erbium doped aluminum oxide laser (Al_2O_3:Er^{3+}) with high power, reliable, and ultra-narrow linewidth performance with no temperature control.

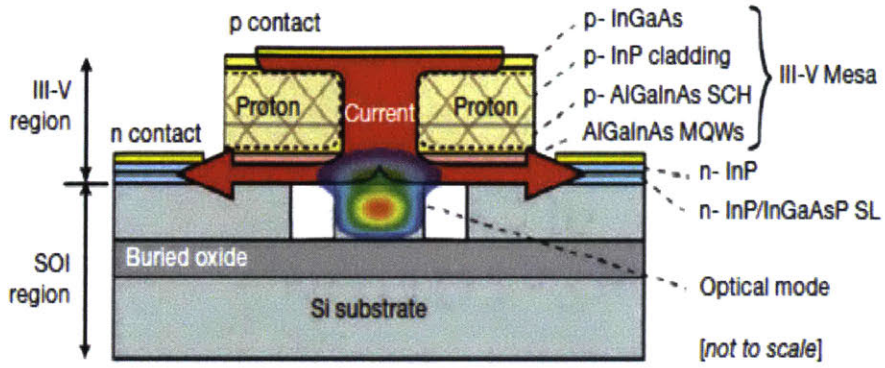

(a) Hybrid III-V Silicon

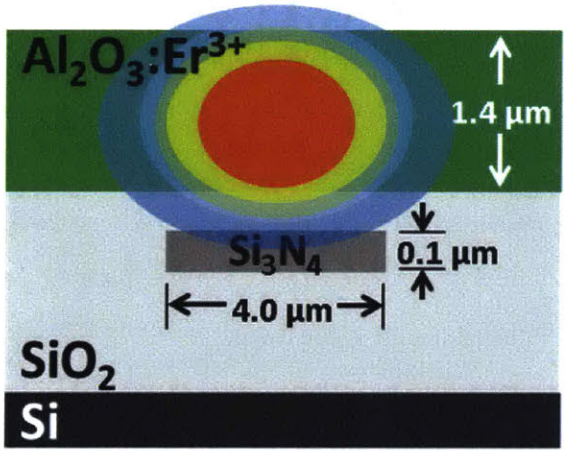

(b) Al_2O_3:Er^{3+}Laser

Figure 1-4: Schematic of (a) hybrid III-V silicon laser and (b) integrated Al_2O_3:Er^{3+}laser on silicon.

1.3 Laser simulation results

In this section, we provide a guideline of designing Al_2O_3:Er^{3+}laser by simulating the laser performance from rate equation modeling. Reference [19] has provided a comprehensive article for the rate equation parameters of Al_2O_3:Er^{3+}laser. One of the distinct characteristics of Al_2O_3:Er^{3+}laser that differs from ideal three-level system is the presence of quenched ion. The quenched ions result in reduce of active agent in stimulated emission process. The ions are instead excited into higher energy state and produce characteristic green light emission when pumped. In addition, this also become the source of instability in CW laser operation. The quenched ion fraction

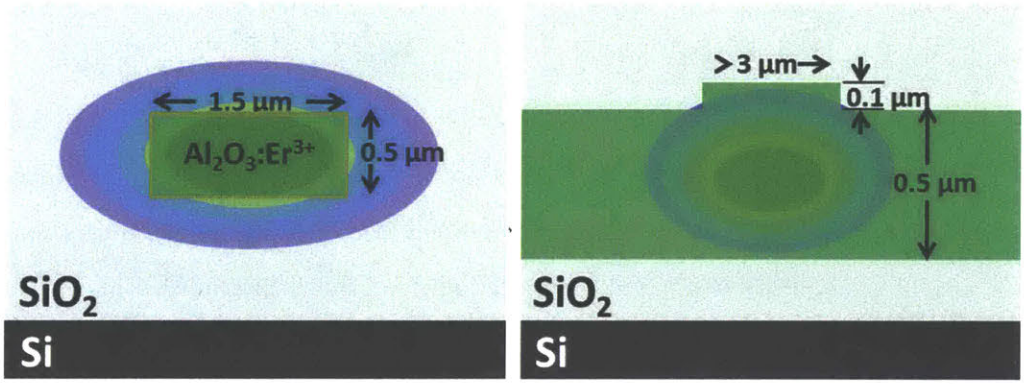

(a) Channel waveguide (b) Ridge waveguide

Figure 1-5: Previous designs for integrated $Al_2O_3:Er^{3+}$laser. (a) Channel waveguide structure. (b) Ridge waveguide structure.

is dependent as the function of erbium doping concentration, as shown in figure 1-6. The rate equation modeling of $Al_2O_3:Er^{3+}$laser taking into account the quenched ion fraction is discussed in detail in appendix A.

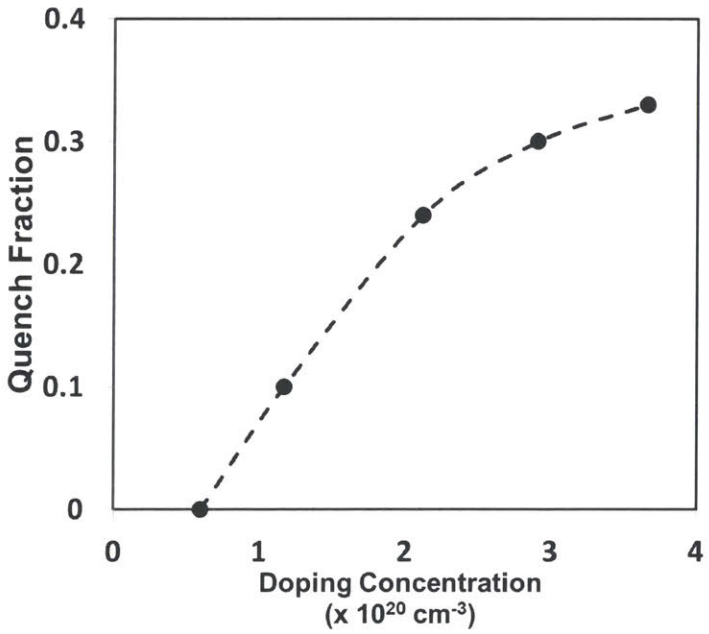

Figure 1-6: Plot of quenched ion fraction as a function of erbium doping concentration, measured.

Here, we show two simulation results as the guideline in designing the laser

cavity. Figure 1-7 show the threshold power requirement and slope efficiency in Al_2O_3:Er^{3+}laser. By using standard parameters (doping concentration 1.5 $\times$ 10^{20} cm^{-3}, length 2.0 cm, quenched ion fraction 0.1), we show that there exist a minimum cavity Q to allow the laser to reach lasing threshold. As the Q factor increase, the threshold power requirement drops and saturate at the "transparent" pump power requirement. The slope efficiency on the other hand has an optimum Q value that maximizes the value. This optimum value can be understood similar to the Q-matching condition for a resonator.

In summary, the guidelines for designing an optimum laser are as following. The doping concentration has to be chosen carefully by taking into account the erbium clustering. The cavity Q should be designed by considering the trade off between the threshold power requirement and desired efficiency. Thus, keeping the cavity intrinsic loss at the same value, increasing the cavity Q factor may not be the best approach as the threshold power improvement may be offset by the drop in efficiency.

1.4 Summary

We have presented an introduction to the development of integrated Al_2O_3:Er^{3+}laser on silicon photonics platform. We demonstrated how Al_2O_3:Er^{3+}laser is a crucial component in the platform for various applications. We discuss the advantages of Al_2O_3:Er^{3+}over hybrid III-V laser in terms of the fabrication complexity, scalability, temperature management, and laser linewidth. Lastly, we analyze the rate equation modeling to provide a general laser design guideline for optimum operation.

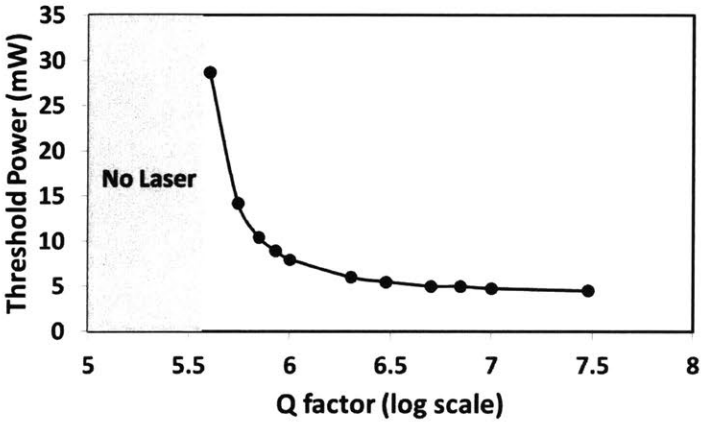

(a) Threshold pump

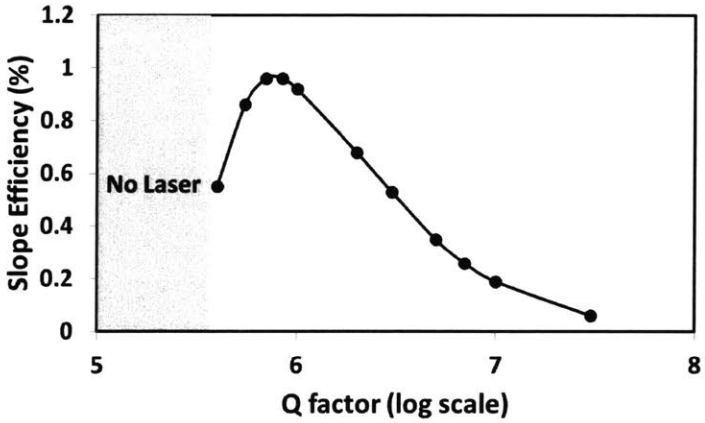

(b) Slope efficiency

Figure 1-7: Simulation results of (a) threshold power P_{th} of laser and (b) laser slope efficiency η with different Q factor of DFB.

Chapter 2

Scalable Laser Design

We present results on scalable laser design for Al_2O_3:Er^{3+}laser. The cavities consist of silicon nitride (single or multi-segments) waveguides and grating features defined by wafer-scale immersion lithography and a top Al_2O_3:Er^{3+}layer deposited as a final backend step in the fabrication process. The resulting waveguides yield high confinement factor ($> 85\%$) and intensity overlap ($> 90\%$) for an octave-spanning range across near infra-red wavelengths ($950 - 2000$ nm). We demonstrated C- and L-bands laser operations for both distributed Bragg reflector and quarter phase shifted distributed feedback lasers. The large mode size lasers allows demonstration of power scaling with output power of > 75 mW without any thermal damage.

2.1 Waveguide design

The first step in constructing an on-chip laser starts from designing the laser waveguide. To define a scalable laser waveguide and cavity, fabrication compatibility with CMOS foundry has to be considered, in addition to high confinement factor and pump-signal intensity overlap for an optically pumped laser.

Previous works [17, 16] in Al_2O_3:Er^{3+}laser have used interference lithography and etching of the gain material, both of which are difficult to incorporate within standard wafer-scale silicon photonics process flows. A preferable approach would be to define laser cavities using standard CMOS processing techniques while reducing unnecessary

fabrication steps on the erbium-doped layer. Silicon nitride (SiN_x) is a low-loss, frontend of line, CMOS compatible material [20] that can be used in the formation of high-resolution photonics features, including waveguides, gratings, and even laser cavities. An erbium-doped glass layer can then be deposited as a backend process step without further etching or processing required. This approach enables large-scale production of erbium-doped waveguide lasers and integration with silicon nitride passive components on silicon photonic chips.

One of the main challenges in the waveguide design is the relatively high refractive index contrast of SiN_x($n_{SiN_x} \approx 1.99$) and Al_2O_3:Er^{3+}($n_{Al_2O_3:Er^{3+}} = 1.65$). The intensity distribution of the fundamental transverse-electrical (TE) mode tends to be more confined in the high-index material, especially for shorter wavelengths. This trend is contrary to the design approach for an efficient erbium-doped laser waveguide, where high confinement in the active material and high intensity overlap between the pump ($\lambda = 980$ nm) and signal ($\lambda = 1550$ nm) modes are preferred. Furthermore, any additional optical intensity localized in the SiN_xwaveguide may introduce detrimental intra-cavity losses from scattering and the intrinsic absorption of the material.

To overcome this, we proposed a novel waveguide design that includes a layer of SiO_2($t = 100$ nm, $w = 4000$ nm) and Al_2O_3:Er^{3+}film ($t_{AlO} = 1.4$ μm), as shown in figure 2-1a. The oxide gap reduces the guiding effect of the high refractive index SiN_xridge and increases the confinement within Al_2O_3:Er^{3+}layer. The distance between the Si to the bottom layer of SiN_x($> 2.5\mu$m) is sufficient to ensure the fundamental TE mode is not affected by the substrate. The dimensions of the structure can be varied to optimize for the confinement factor and intensity overlap in pump and signal wavelengths. Figure 2-1b shows the intensity distributions of the fundamental TE mode at 980 nm (pump p) and 1550 nm (signal s) calculated by finite difference mode solver.

To calculate the confinement factor (γ_p) and intensity overlap (Γ_{sp}), we define the following formulas.

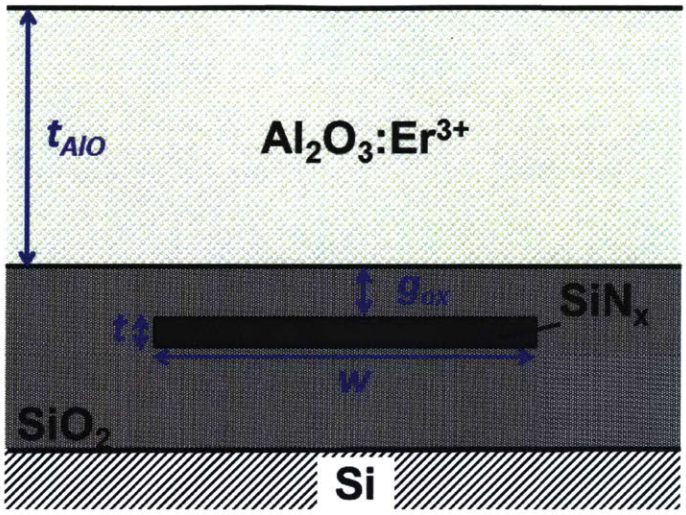

(a) Thin SiN_xwaveguide design

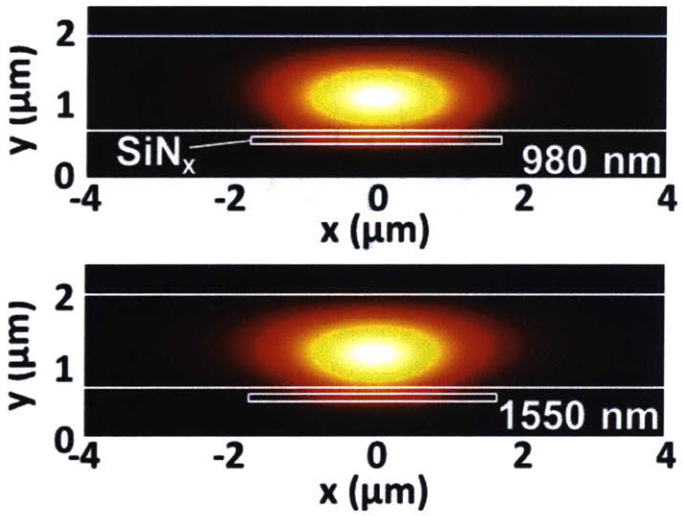

(b) Mode calculation

Figure 2-1: (a) Cross section view of the laser waveguide structure for thin (~100 nm) SiN_xlayer. (b) The calculated intensity distribution of the fundamental TE mode at 980 nm and 1550 nm.

$$\gamma_{s,p} = \frac{\int_A I_{s,p} dA}{\int_\infty I_{s,p} dA} = \frac{\sum_{active(ij)} I_{ij}^{(s,p)}}{\sum_{ij} I_{ij}^{(s,p)}} \tag{2.1}$$

$$\Gamma_{sp} = \frac{\int_A I_p I_s dA}{\sqrt{\int_\infty I_p^2 dA}\sqrt{\int_\infty I_s^2 dA}} = \frac{\sum_{active(ij)} I_{ij}^{(p)} I_{ij}^{(s)}}{\sqrt{\sum_{ij} I_{ij}^{2\,(p)}}\sqrt{\sum_{ij} I_{ij}^{2\,(s)}}} \tag{2.2}$$

For waveguide dimensions specified above, we obtain $\gamma_s = 87\%$, $\gamma_p = 89\%$, and $\Gamma_{sp} = 93\%$. Note that the integration of the mode intensity is approximated by the summation over discrete space coordinate i and j. Thus our waveguide design yields high intensity confinement factors in the active medium and is wavelength insensitive for broad wavelengths (980 $--$ 1550 nm), permitting either resonant pumping around 1480 nm or pumping near 980 nm.

We extend the waveguide design to work for a thicker SiN_x(e.g. $t = 200$ nm). A thicker SiN_xallows integration into a more general silicon photonics wafer-scale process where compact, higher-confinement SiN_xstructures might be preferred [21]. For thick layer, the fundamental TE mode of shorter wavelength ($\lambda < 1000$ nm) tend to be confined in the SiN_xstructure. To obtain a similar property to the thin SiN_xdesign, we use a multi-segment waveguide structure to mimic the weak confinement in the SiN_x.

Figure 2-2a shows a schematic of the multi-segmented waveguide design. It consists of a silicon (Si) substrate, five SiN_xsegments (thickness t of 200 nm, width w of 450 nm, and gap g of 400 nm), enclosed by a SiO_2layer (oxide gap g_{ox} of 200 nm), and Al_2O_3:Er^{3+}gain film (thickness $t_{AlO} = 1100$ nm). The layers are similar as before, with the only difference is in the thicker SiN_xlayer. With these parameters, we obtain the same high confinement factor ($> 85\%$) and a near perfect intensity overlap ($> 98\%$) for pump and signal wavelengths.

We perform wavelength sensitivity analysis of the multi-segmented structure for a selection of near infrared (NIR) wavelengths range; 800 nm, 950 nm and 980 nm (diode pump lasers), 1050 nm (Yb- and Nd-doped lasers), 1300 nm (Nd-doped lasers), 1550 nm (Er-doped lasers), and 2000 nm (Tm- and Ho-doped lasers). The intensity distributions of the fundamental TE modes at the various wavelengths are calculated by a finite-difference mode solver, as shown in figure 2-3. By inspection, we observe

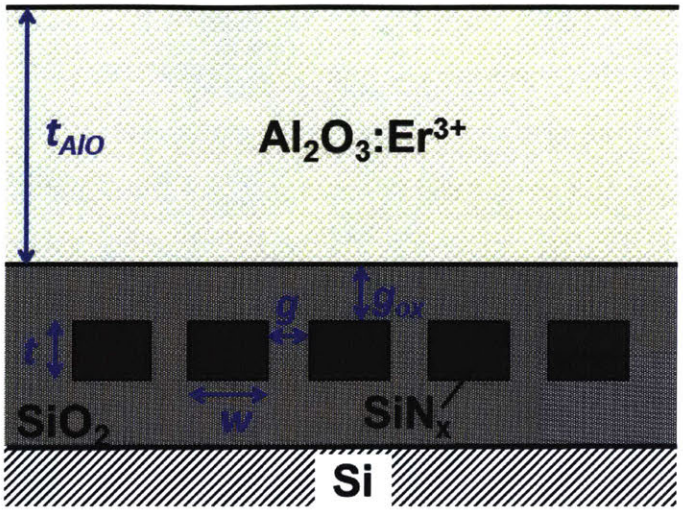

(a) Thick SiN_x waveguide design

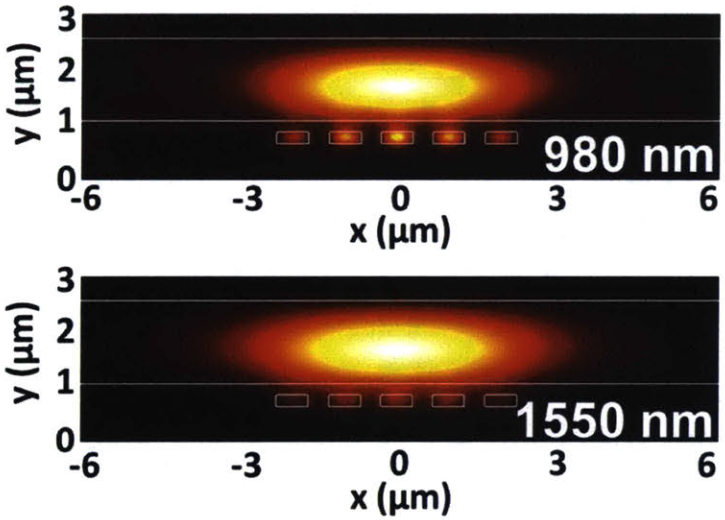

(b) Mode calculation

Figure 2-2: (a) Cross section view of the laser waveguide structure by multi-segmented design for thick (~200 nm) SiN_x layer. (b) The calculated intensity distribution of the fundamental TE mode at 980 nm and 1550 nm.

that the mode distribution at shorter wavelengths tends to concentrate in the silicon nitride layer. Starting from 950 nm, the mode is distributed almost exclusively in the gain layer.

The confinement and overlap factors (with 980 nm chosen as a reference pump wavelength) for these wavelengths are shown in figure 2-4. We obtain > 85% confine-

ment factor for all wavelengths longer than 950 nm and > 98% intensity overlap factor with a 980 nm pump mode over an octave of near-infrared wavelength light sources, demonstrating the wavelength insensitivity of the waveguide. While here we present a design specifically optimized for 980-nm pumping, the wavelength-insensitive range and lower wavelength cutoff can also be shifted by adjusting the waveguide dimensions. Such properties allows the design to be used for a variety of rare earth doped lasers; so far, we have demonstrated its application for Yb (1030 nm) [22], Er (1560 nm) [23], and Tm (1800 nm) [24].

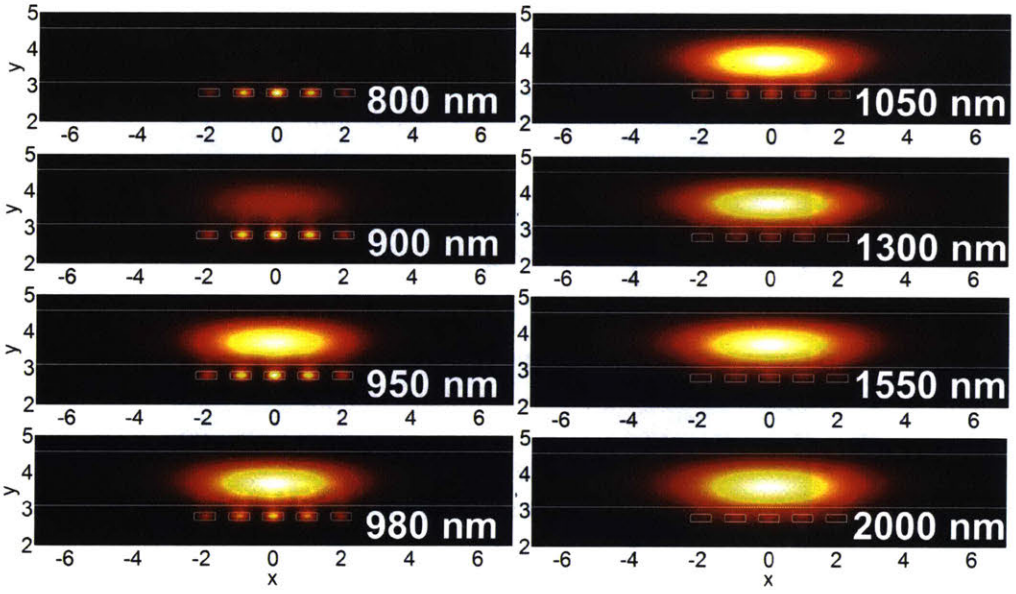

Figure 2-3: Broadband mode-solver intensity distribution

To form the on-chip laser, we use various Bragg grating designs to construct the resonator. The standard approach of defining a grating structure consists of a main waveguide structure and periodic perturbations. The periodic perturbations can take the form of side wall etching [25], periodic side pieces [26], or combination of both. For our more unique multi-segmented design, we show various ways of contructing the Bragg grating in figure 2-5. The grating strengths κ can be tuned by choosing the appropriate type of perturbation.

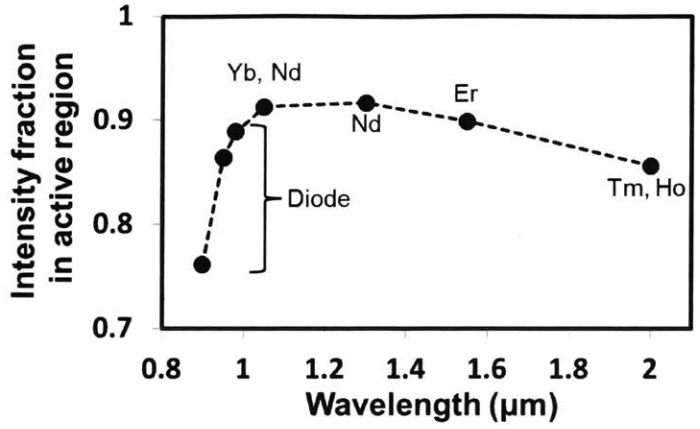

(a) Confinement factor

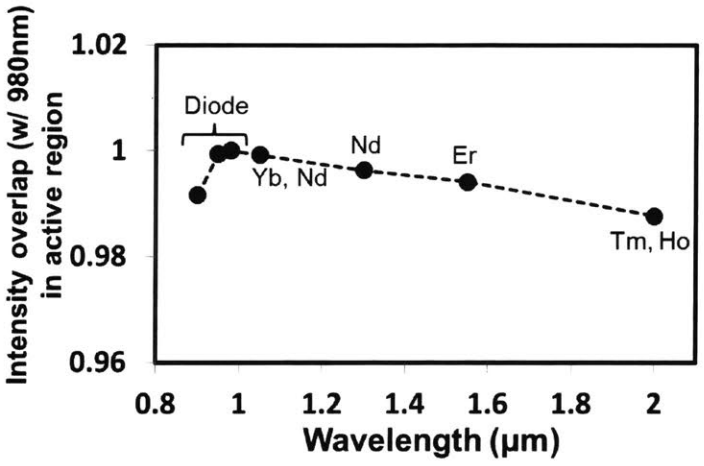

(b) Intensity overlap

Figure 2-4: (a) Calculation of confinement factor and (b) intensity mode overlap for 980 nm for various laser sources in NIR wavelengths using waveguide design in 2-2a.

2.2 Waveguide fabrication

In this section, we will provide an overview of the laser waveguide fabrication. Most of the fabrication efforts have been performed in collaboration with other group members and subcontracted to external CMOS foundry, hence we only provide a brief review here.

The laser waveguide fabrication steps are described by the following. A 4 μm thick plasma-enhanced chemical vapor deposition (PECVD) SiO_2layer was grown, followed

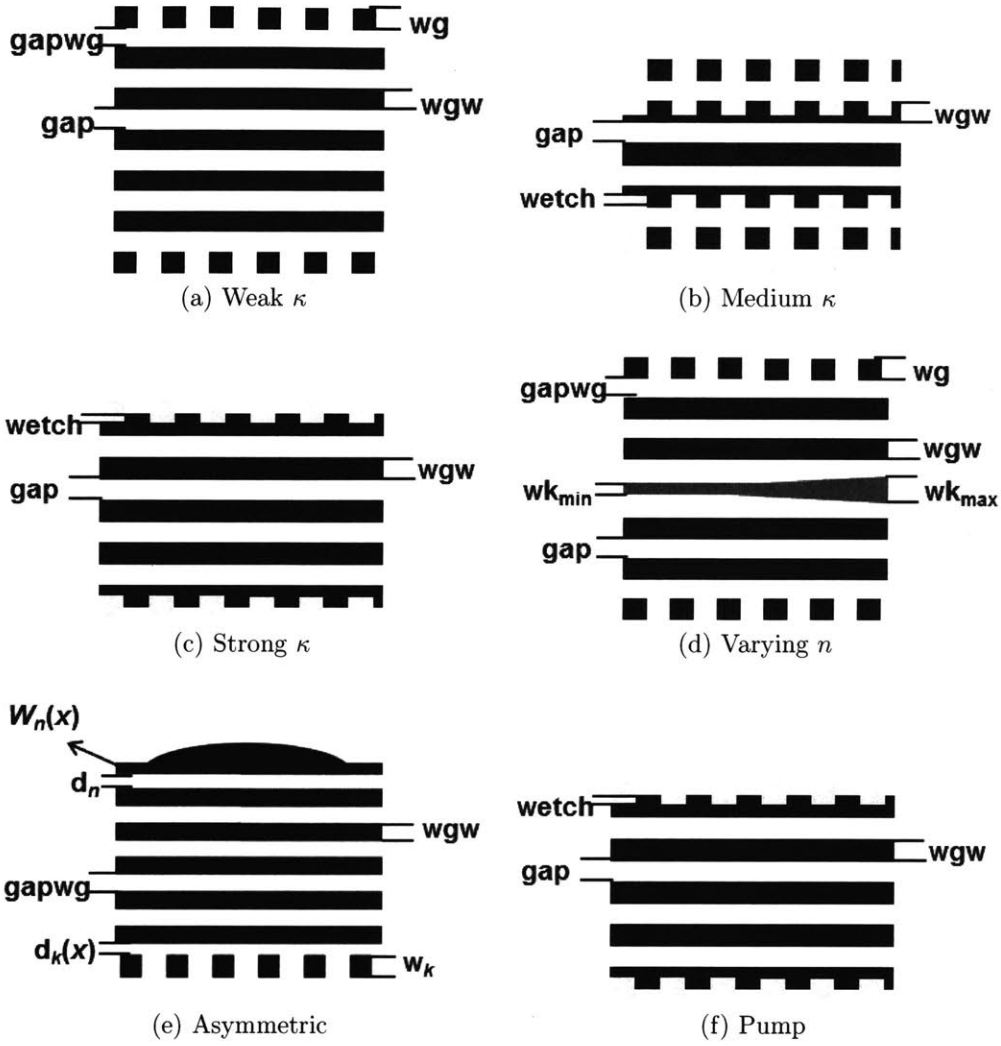

Figure 2-5: Various grating designs on multi-segmented waveguide.

by deposition of a PECVD SiN_xlayer 100 (or 200) nm. Both $SiO_2$and SiN_xlayers were chemically mechanically polished (CMP) to reduce losses due to surface roughness. The silicon nitride layer was subsequently annealed at 1050°C for 72 min. to reduce absorption due to Si-H and N-H bonds around 1.52 μm. The nitride layer was then patterned using 193 nm immersion lithography and reactive ion etching. After patterning, another PECVD SiO_2layer was deposited for the oxide gap layer and CMP-ed to a final height of 100 (or 200) nm above the silicon nitride layer. Trenches for dicing and fiber end coupling were then etched into the edges of the dies by deep oxide and silicon etching. Finally, the wafers were transferred from the CMOS foundry, diced

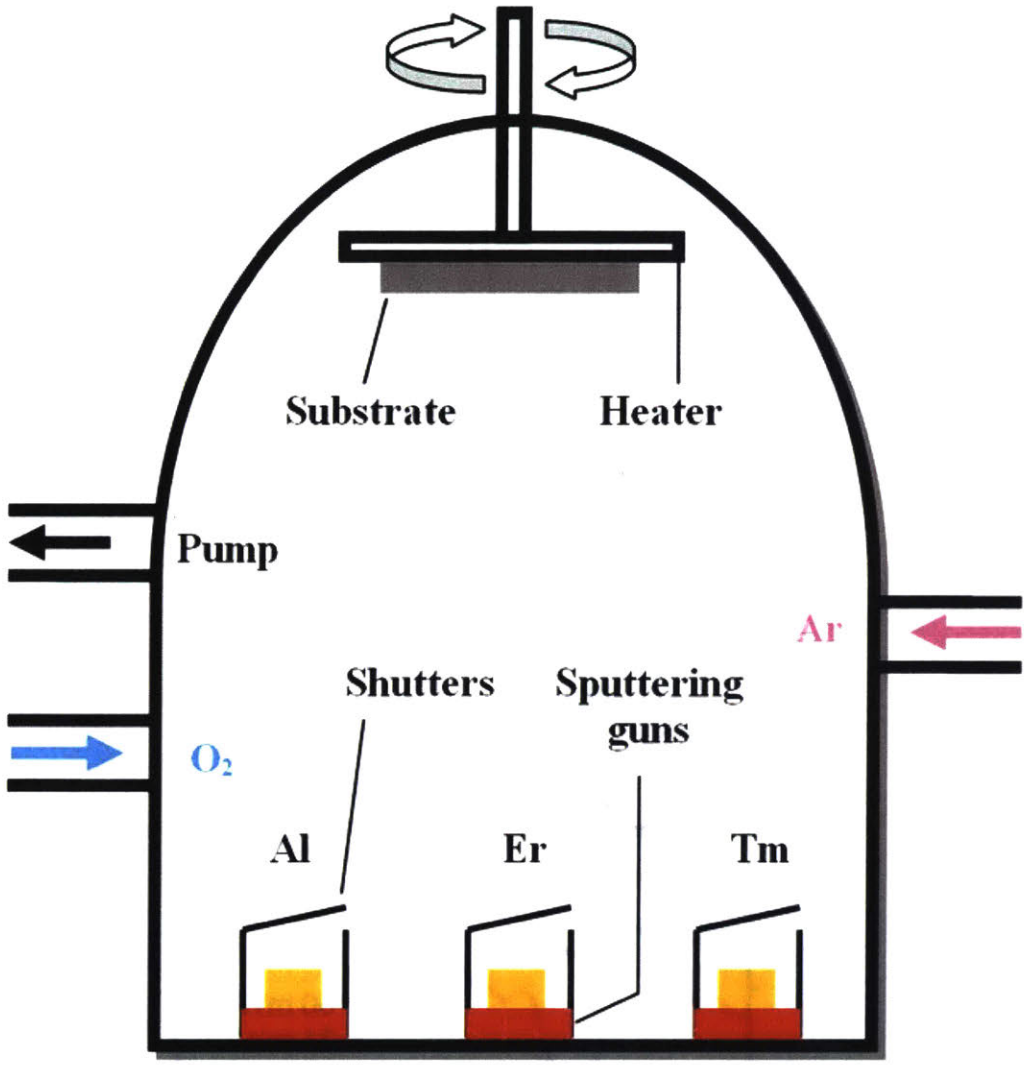

Figure 2-6: RF sputtering machine

into individual dies and an Al_2O_3:Er^{3+}layer was deposited by reactive co-sputtering (figure 2-6) using a similar process to that reported in [18].

Using the prism coupling method to measure the planar losses around 1550 nm, we determine the background loss in the Al_2O_3:Er^{3+}film to be < 0.1 dB/cm (see figure 2-7a). This value is close to the sensitivity limit of the measurement apparatus. In addition to loss characterization, we perform a gain measurement at varying wavelengths. A typical measurement of gain of a Al_2O_3:Er^{3+}waveguide (doping concentration 1.4×10^{20} cm^{-3}, length 1.6 cm, waveguide design as shown in figure 2-1a) are shown in figure 2-7b. Maximum peak gain of 1 dB/cm can be observed at around

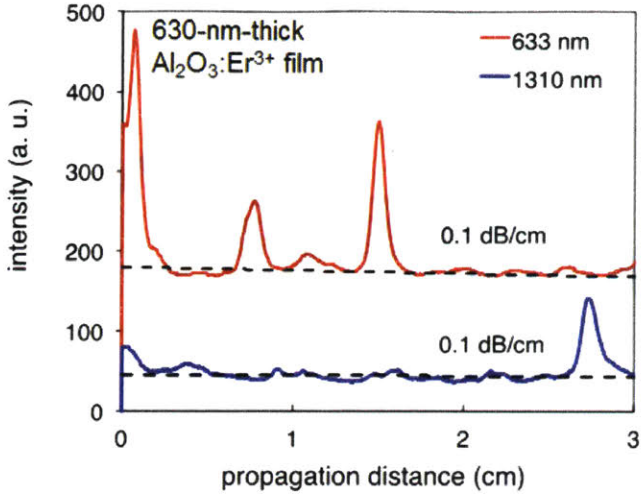

(a) Loss measurement

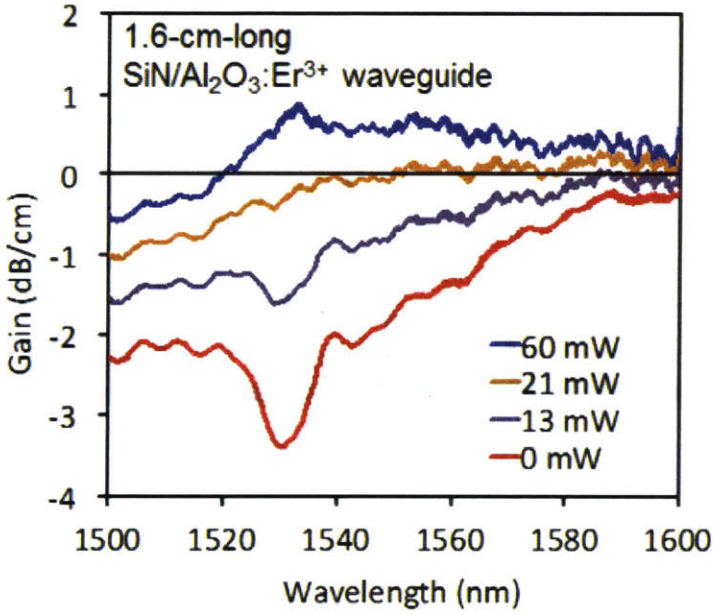

(b) Gain measurement

Figure 2-7: (a) Loss measurement by prism coupling (b) Gain measurement at various pump power.

1530 nm (standard erbium emission [13]) in the spectrum at on-chip pump power $\sim$ 60 mW.

2.3 DBR laser

For initial test in the laser waveguide design,we construct a simple distributed Bragg Reflector (DBR) laser that consists of a straight waveguide of length $L_{gain} = 20$ mm and width $w = 4000$ nm confined by two Bragg grating as reflecting mirrors (figure 2-8). The gratings are formed by waveguides of length $d = 1.5$ mm with periodically notched side walls having notch widths of s_1 at one end and s_2 at the other end. s_1 is fixed at 1.29 μm for a reflectivity of ~100% and s_2 is varied from 418 nm to 796 nm to achieve a reflectivity of 85% to 99.6%. The grating period Λ is varied between lengths of 478, 487 and 498 nm, which corresponds to Bragg wavelengths of 1536, 1561 and 1596 nm, respectively. The erbium doping concentration is 1.4×10^{20} cm^{-3}.

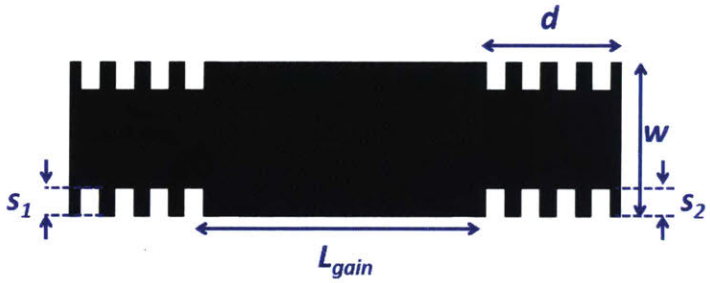

Figure 2-8: Design of DBR laser

Figure 2-9 shows the experimental setup used to measure the lasers. Pump light from 978 nm and 975 nm laser diodes are coupled into the chip on each side using fiber 980/1550 nm wavelength division multiplexers (WDM), respectively. The laser output is collected from the 1550 nm port of the WDM at both sides.

By insertion loss measurements, we estimated coupling losses at each facet of the chip of -5.6 dB and -7.3 dB for 980 nm and 1550 nm TE-polarized light, respectively. Using the measured facet loss, we determine launched pump powers of 147 mW and 98 mW from 978 nm and 975 nm diodes, respectively. The maximum output power is obtained from the DBR laser with center wavelength at 1561 nm and reflectivities of $R_1 = 100\%$ and $R_2 = 95\%$. To characterize the laser efficiency, we plot the output power at different pump powers, as shown in figure 2-10a. We start by pumping from the 978 nm diode (left) only. When the diode reaches the maximum pump power, we

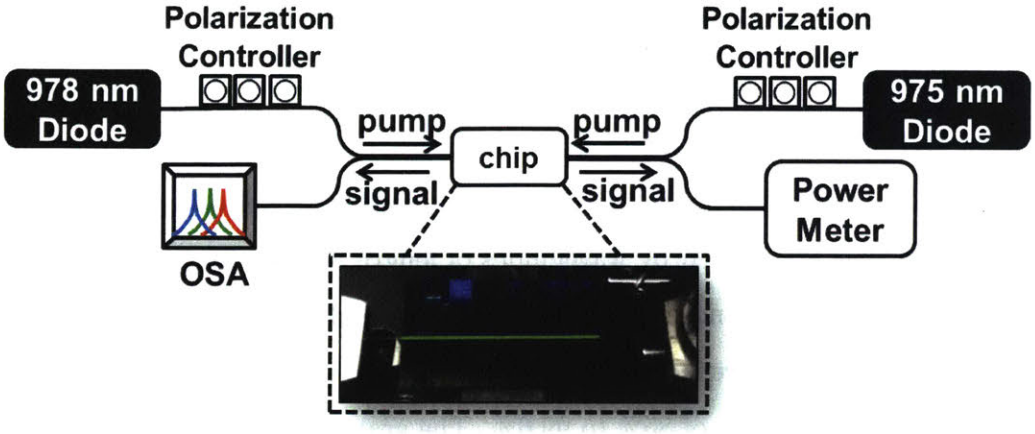

Figure 2-9: Experimental setup of laser measurement

turn on the pump from the 975 nm diode (right). We obtain maximum on-chip output power of $P_{max} = 5.1$ mW with a lasing threshold of $P_{th} = 44$ mW. This corresponds to a slope efficiency of $\eta = 2.6\%$.

In addition, we obtain maximum output powers for DBR with different grating periods of $P_{max} = 2.5$ mW ($\lambda = 1536$ nm) and $P_{max} = 0.5$ mW ($\lambda = 1596$ nm). These outputs are obtained from cavities with reflectivity of $R_2 = 86\%$ ($\lambda = 1536$ nm) and $R_2 = 95\%$ ($\lambda = 1596$ nm), respectively. The difference in the optimum reflectivity for the DBR cavities can be attributed to the difference in the gain threshold and maximum small signal gain at different wavelengths. Figure 2-10b shows the spectra of three different lasers recorded by the OSA. The laser emission at 1596 nm is a consequence of low grating scattering loss, low background losses in the gain film and the wide gain spectrum of Al_2O_3:Er^{3+}. We note that the DBR laser spectra lie within two important communication bands, the C-band and L- band. By simply modifying the period of the gratings in the SiN_xlayer, it is feasible to fabricate arrays of lasers spanning both communication bands.

From the spectrum of the DBR laser, we often obtain multimode lasing. This is expected, considering the free spectral range (FSR) of the cavity (~ 0.04 nm) is much smaller than the grating bandwidth (~ 1 nm). In the next sections, we discuss laser cavities to produce a single-frequency spectrum.

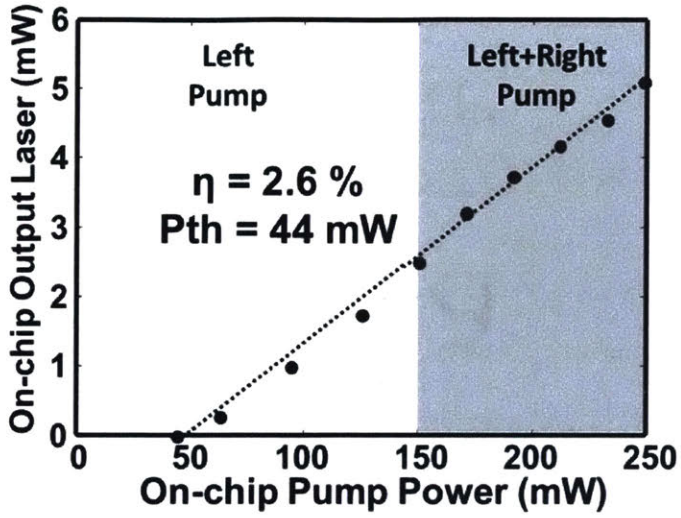

(a) DBR power measurement

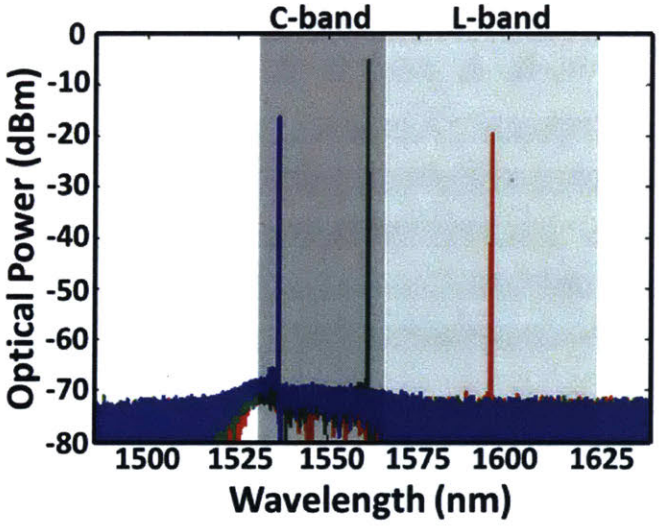

(b) DBR spectrum

Figure 2-10: (a) Output power vs on-chip pump power for the DBR laser at 1561 nm laser wavelength. (b) Spectrum of the output DBR laser within the C- and L-band.

2.4 Quarter phase shift DFB laser

To obtain a single-frequency laser, a distributed feedback (DFB) design with phase defect can be constructed [27]. Chronologically, at this moment of the thesis work, we decided to focus only on the thick SiN_xdesign. Therefore, we apply the five-segment

thick SiN_xdesign to realize single-frequency and narrow-linewidth Al_2O_3:Er^{3+}DFB lasers.

The DFB cavities consist of a grating structure with a quarter phase shift (QPS) at the center of each device. Each grating unit is formed by placing additional periodic pieces on both sides of the five-segment SiN_xstructure, as shown in figure 2-11. These periodic side pieces have width w of 300 nm with the grating strength κ adjusted by varying the gap distance d_{wg}. We fabricated a total of 9 devices with 3 grating period variations (Λ = 482 nm, 492 nm, and 502 nm) and 3 grating strength variations (d_{wg} / κ = 600 nm / 0.6 cm^{-1}, 350 nm / 0.9 cm^{-1}, and 200 nm / 1.2 cm^{-1}). The erbium doping concentration in the gain is kept at $N_{doping} = 1.0 \times 10^{20}$ cm^{-3}.

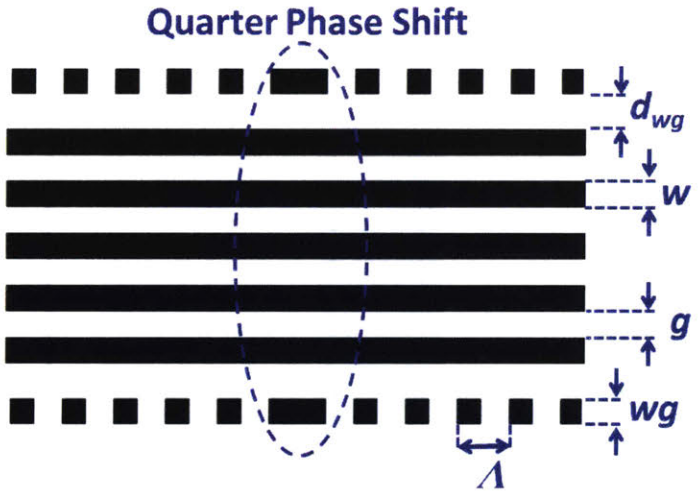

Figure 2-11: Design of QPS-DFB laser. The cavity structure consists of five SiN_xsegments with grating perturbation provided by two additional side pieces.

To characterize their performances, we again pump the DFB lasers from both sides using fiber pigtail laser diodes at 978 nm and 976 nm. We obtain the best laser performance from devices with d_{wg} = 350 nm or $\kappa = 0.9$ cm^{-1} for all three wavelengths. Figure 2-12b shows the spectra of DFB lasers operating at 1536 nm, 1566 nm, and 1596 nm, which covers a similar emission bandwidth that has been shown previously in DBR lasers. Maximum output powers of 0.41 mW, 0.76 mW, and 0.47 mW at widely spaced wavelengths wavelengths within both the C and L bands of the erbium

gain spectrum (1536 nm, 1566 nm, and 1596 nm). The laser operating at 1536 nm has the lowest output power, corresponding to > 46.1 dB side mode suppression ratio (SMSR) for all devices. We characterize the slope efficiency and threshold power of the lasers, as shown in figure 2-12a. We obtain slope efficiencies η = 0.3%, 0.6%, and 0.3% and threshold powers P_{th} = 55 mW, 65 mW, and 105 mW for lasers at wavelengths 1536 nm, 1566 nm, and 1596 nm, respectively.

Compare to DBR lasers, DFB spectrum show a single peak in the OSA spectrum (limit resolution of 0.02 nm). The quality of these single longitudinal sources can be measured from the laser linewidth, which will be discussed in the following chapter. In here, the best performing laser is again shown to be at $\sim$ 1560 nm. Although Al_2O_3:Er^{3+}laser has peak emission at 1530 nm, the reabsorption loss is lower at longer wavelengths. Through the trade off between these two factors, wavelength around 1560 nm tend to perform better in most of the designs.

2.5 High power scaling

As one of the important metrics in the integrated laser, we demonstrate power scaling of single frequency Al_2O_3:Er^{3+}DFB laser by using a high power 1480 pump Raman laser (figure 2-13). By using a similar waveguide design with thin SiN_xstructure, we show that the large mode area of the laser enable power scaling without the risk of thermal damage. A series of QPS-DFB structures with variation in grating strengths and cavity lengths were tested. The grating etch variation on each side of the waveguide (similar to grating in DBR lasers in figure 2-8) was s = 100, 123, 145 nm and the DFB length was varied between 15 and 23 mm. The choice of N_{doping} = 0.9 $\times$ 10^{20} cm^{-3} for Er ion concentration ensures sufficient gain without excessive pump absorption along the waveguides.

The fiber to chip coupling introduced approximately 10 dB loss both for the pump and the emitted signal. No damage was observed even when more than 1 W of pump power was coupled into the waveguide. DFBs with stronger width modulation (s = 123, 145 nm) demonstrated single mode lasing at 1563 nm wavelength while the best

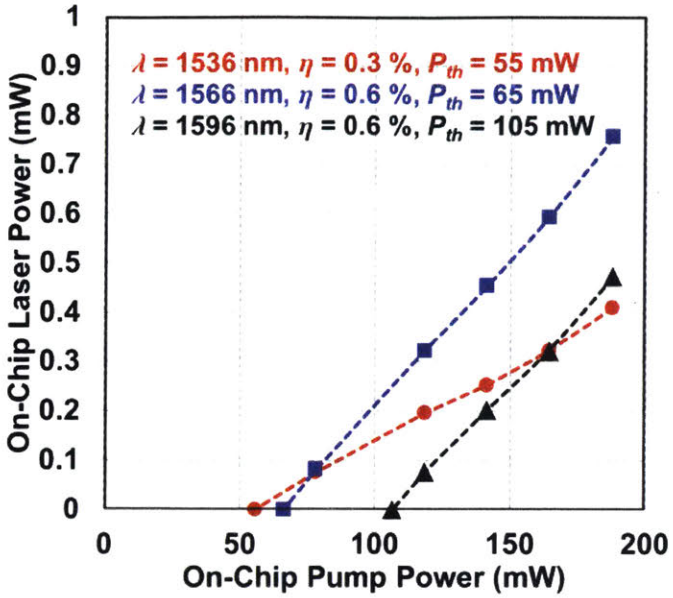

(a) QPS-DFB power measurement

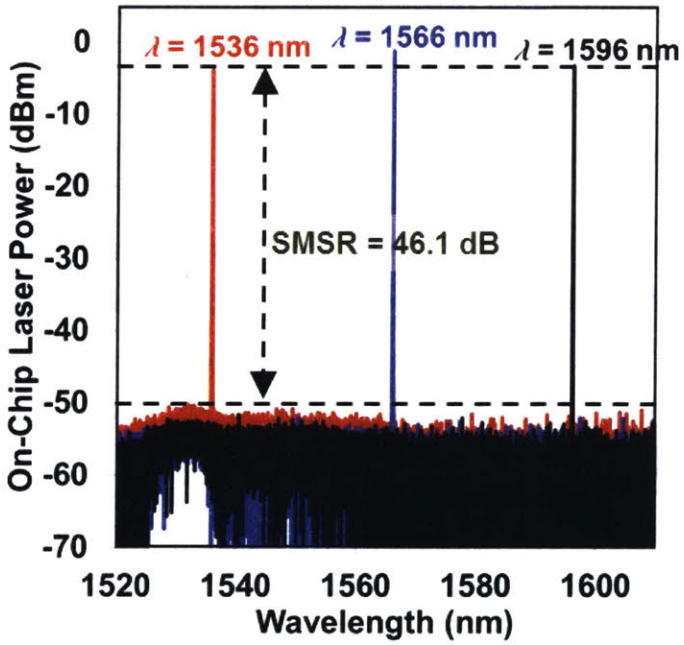

(b) QPS-DFB spectrum

Figure 2-12: (a) Output power of Al_2O_3:Er^{3+}QPS-DFB lasers vs. pump power.(b) Optical spectrum of Al_2O_3:Er^{3+}QPS-DFB lasers at various grating periods.

slope efficiency of 7 % was achieved with the strongest cavity design. Figure 2-14a depicts two sample pump-signal efficiency curves for 145 nm width modulation ($\kappa =$

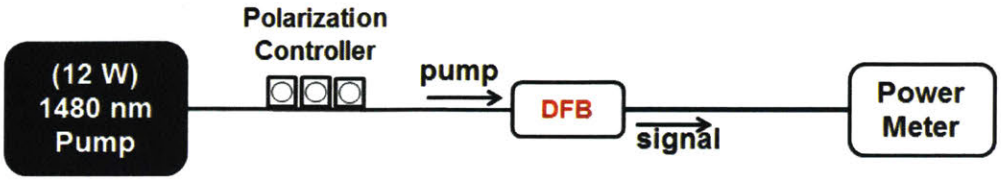

Figure 2-13: High power DFB experiment setup

0.3 m^{-1}) with two different grating lengths. The longer DFB demonstrates 75 mW of on-chip laser power when pumped with 1.1 W, which is to our knowledge the greatest power achieved from a chip based laser in the communication wavelengths [28].

2.6 Summary

In summary, we have demonstrated a CMOS compatible and scalable integrated Al_2O_3:Er^{3+}lasers. The laser cavity design was defined using 193 nm immersion lithography within a standard CMOS foundry and the novel waveguide design that enable the Al_2O_3:Er^{3+}layer to be deposited as a final backend-processing step. The waveguide structure is designed to have broad wavelength insensitive property, with high confinement factor ($> 85\%$) and intensity overlap ($> 90\%$) for an octave-spanning range across near infra-red wavelengths (950 $--$ 2000 nm).

Maximum output powers of 2.5 mW, 5.1 mW, and 0.5 mW are obtained from DBR cavities at center wavelength at 1536 nm, 1561 nm, 1596 nm, respectively. These laser wavelengths lie within both the C- and L-bands of the erbium gain spectrum. The maximum output power at 1561 nm corresponds to a slope efficiency of $\eta = 2.6\%$ and a lasing threshold of $P_{th} = 44$ mW.

We obtain a similar performance for DFB cavities, with output powers of 0.41 mW, 0.76 mW, and 0.47 mW 1536 nm, 1566 nm, and 1596 nm. The advantage of DFB cavity (compare to DBR) is the single frequency operation in the laser. The laser operating at 1536 nm has the lowest output power, corresponding to $>$ 46.1 dB SMSR for all devices. We obtain slope efficiencies $\eta = 0.3\%$, 0.6%, and 0.3% and threshold powers $P_{th} = 55$ mW, 65 mW, and 105 mW for lasers at wavelengths 1536

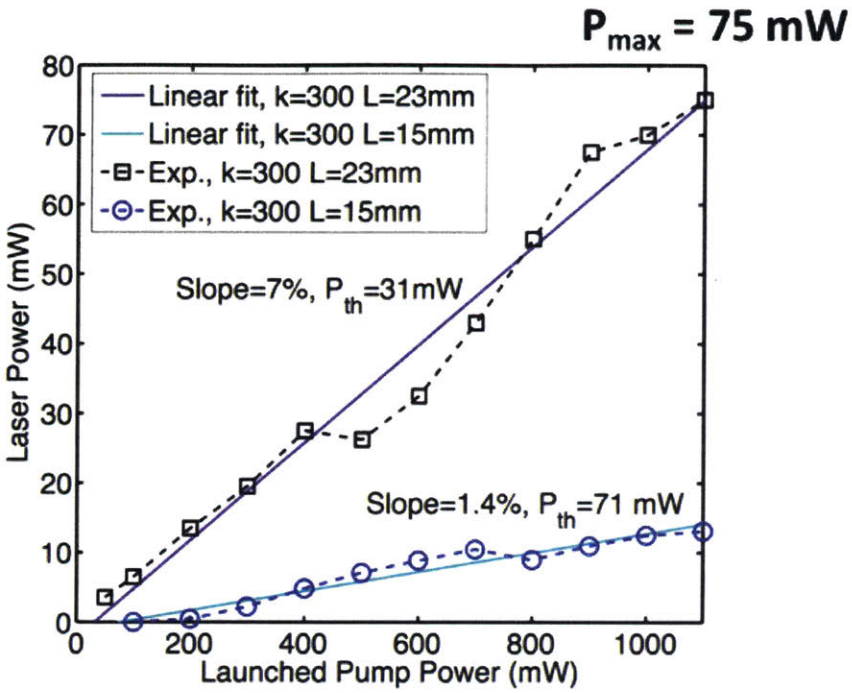

(a) High power DFB measurement

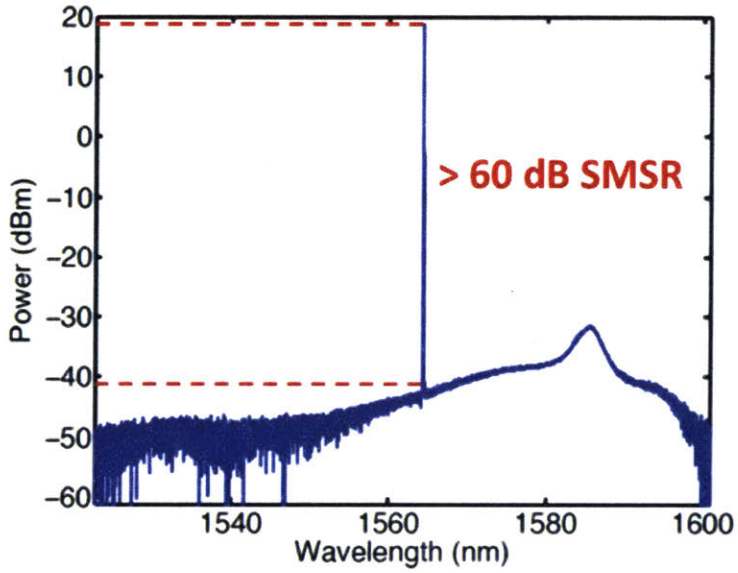

(b) High power DFB spectrum

Figure 2-14: (a) Output power vs on-chip pump power for high power DFB measurement. (b) Spectrum of the high power output of DFB laser.

nm, 1566 nm, and 1596 nm, respectively.

To show the power scalability in our design, we demonstrate a DFB laser with

output power of > 75 mW by using a high power pump source. We show no thermal damage was observed due to the large mode area of our design.

The main advantage of this approach lies in the robust, high resolution, and wafer-scale silicon nitride structuring and backend deposition of the Al_2O_3:Er^{3+}layer. More complex structures can be directly patterned in the SiN_xlayer. Furthermore, these structures can be mass produced and integrated with other silicon photonics devices in a standard CMOS foundry.

Chapter 3

Ultra-narrow Linewidth Laser Design

We present the discussion on obtaining an ultra-narrow linewidth laser. We review the linewidth measurement theory and recirculating setup to accurately determine the laser linewidth. We also compare the discrete and distributed design for quarter phase shift in DFB laser. We show that due to a more uniform intensity distribution in the cavity, distributed phase shift DFB demonstrate a better performance in efficiency and linewidth than a discrete quarter phase shift design.

3.1 Linewidth theory and measurement

Linewidth is defined as the full width half maximum of the optical spectrum or power spectral density at the emission wavelength. Linewidth represents the frequency noise in the laser which can be classified from two distinct sources, the quantum noise and technical noise [29, 30, 31]. The quantum noise comes from the spontaneous emission noise from the cavity, and it can be calculated from the Schawlow-Townes formula. The Schawlow-Townes formula for laser linewidth is given by the following.

$$\Delta\nu_L = \frac{2\pi h\nu_L(\Delta\nu_c)^2}{P_{out}} \tag{3.1}$$

h is Planck's constant, $\Delta\nu_L$ is the laser linewidth, P_{out} is the output power of the laser, and $\Delta\nu_c$ is the passive cavity linewidth related to the cavity lifetime τ_c. To account for the reabsorption loss in three-level state lasers, the modified Schawlow-Townes [32] formula is defined as the following.

$$\Delta\nu_L = \frac{2\pi h\nu_L(\Delta\nu_c)^2}{P_{out}}\left[1-\frac{\tau_c}{\tau_{loss}}\right]\left[1-\frac{\sigma_L^{abs}(c\tau_c\sigma_L^{em}N_T-1)}{\sigma_L^{em}(c\tau_c\sigma_L^{abs}N_T+1)}\right]^{-1} \tag{3.2}$$

$$\frac{1}{\tau_c} = \frac{1}{\tau_{loss}} + \frac{1}{\tau_{out}} = 2\pi\Delta\nu_c \tag{3.3}$$

The cavity lifetime τ_c is dependent on the loss decay time τ_{loss} and outcoupling decay time τ_{out}. c is the speed of light, N_T is the doping concentration, σ_L^{abs} and σ_L^{em} are the cross section of Al_2O_3:$Er^{3+}$for absorption and emission, respectively. In Al_2O_3:Er^{3+}laser, the modified Schawlow-Townes limit shows significant linewidth broadening due to the additional reabsorption loss, as shown in figure 3-1a.

From the equations, it shows that the linewidth can be improved by a higher Q in the passive cavity. We calculate the linewidth variation for a fixed output power at 0.5 mW for various Q in figure 3-1b. To obtain the best linewidth performance, laser at a longer wavelength (around 1600 nm) with lower reabsorption loss is preferred.

The technical noise is the environmental noise of the laser, which includes the mechanical vibrations, temperature fluctuations, and pump power noise. The contributions from these two terms can be differentiated from the profile; the quantum noise has a Lorentzian distribution while the technical noise is white (Gaussian) in nature. The linewidth measurement can be obtained by self-heterodyne of the laser signal. The self-heterodyne measurement setup will characterize both the Gaussian and Lorentzian terms, which result in convolution of the functions. By fitting it to a Voigt profile, the contribution from each term can be differentiated. Lastly, the "real" frequency linewidth can be obtained by half of the full width half maximum of Lorentzian component of the curve.

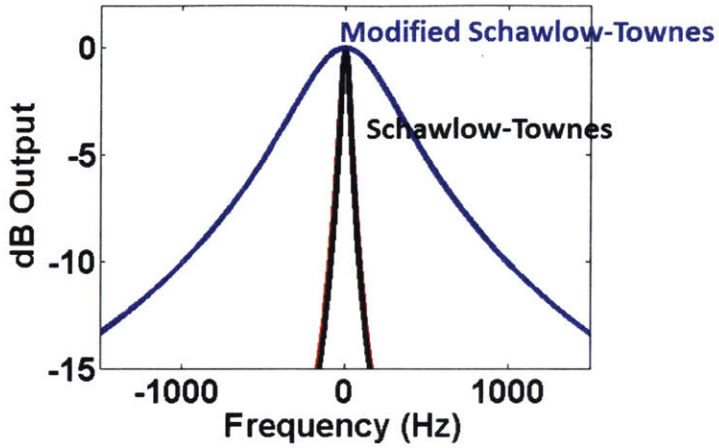

(a) Schawlow-Townes Calculation

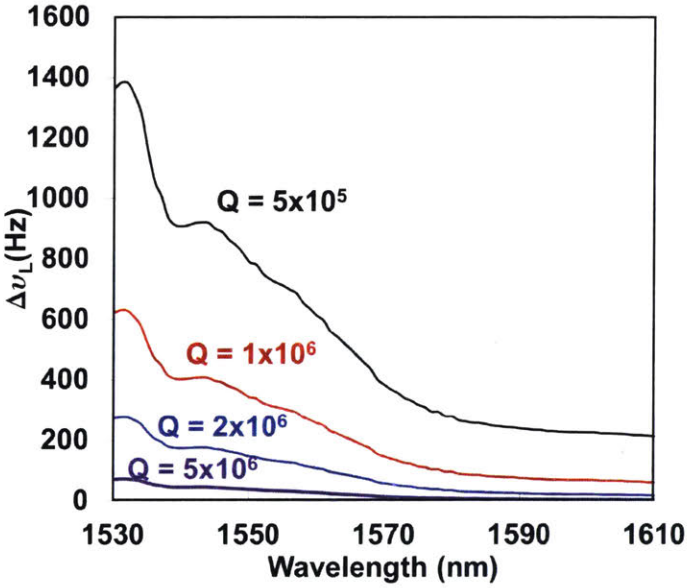

(b) Linewidth calculation

Figure 3-1: (a) Linewidth calculation based on modified three-level state Schawlow-Townes limit. (b) Modified Schawlow-Townes limit at different laser wavelength for Al_2O_3:Er^{3+}at output power of 0.5 mW and background loss of 0.15 dB/cm.

Figure 3-2 shows the method for linewidth measurement by a self-heterodyne delayed interferometer setup (SHDI) [33].The laser input is split into two branches. The first branch passes through a frequency shifter such as single sideband modulator (SSB) or acousto optics modulator (AOM) to shift the original frequency by an radio frequency signal (RF). A polarization controller, erbium doped amplifier (EDFA),

and an isolator are placed in the first arm to compensate for the loss in SSB/AOM and also to prevent back-reflection at the splitter. The other branch passes through a long fiber delay with length L_{delay} and another polarization controller. The presence of the fiber delay is to prevent the phase interference in the self-heterodyne, thus it has to be longer than the coherent length of the laser $L_{coherence}$.

From the Schawlow-Townes formula, the fundamental (quantum) linewidth limit of an Al_2O_3:Er^{3+}DFB laser can reach the sub-kHz level. As a comparison, if $\Delta\nu$= 1 kHz and the speed of light $c/n = 2 \times 10^8$ m/s, then the minimum L_{delay} needs to be at least 200 km. Such a long fiber requirement can be alleviated in a recirculating SHDI (R-SHDI) configuration [34], as shown in figure 3-3. The setup is similar to a standard SHDI, but one of the branches goes to a multipass cavity that consists of a fiber delay and AOM for frequency shifting (f_{AOM} = 44 MHz). Thus, the spectrum at frequency $n \times f_{AOM}$ corresponds to an auto-correlation of the input light after passing through the equivalent delay of $n \times L_{delay}$. Lastly, an EDFA, an optical isolator, and a tunable filter are included to compensate for round-trip loss.

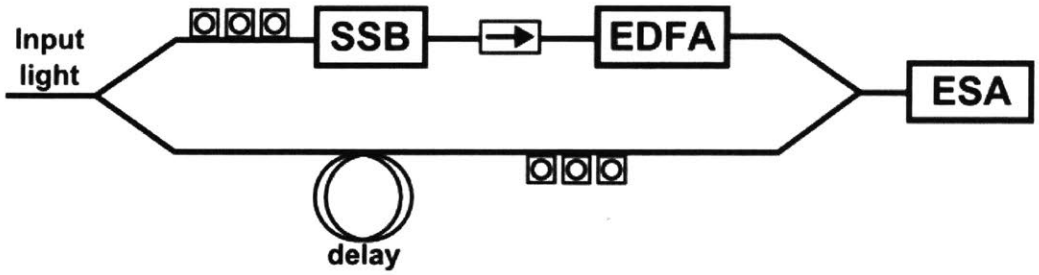

Figure 3-2: Standard self-heterodyne delayed interferometer setup.

Thus, we have provided a brief review of the linewidth theory and measurement in a laser. The modified Schawlow-Townes limit shows additional broadening to the frequency noise. In addition, the linewidth measurement setup characterizes two type of frequency noises (quantum and technical), which can be differentiated by fitting the self-heterodyne spectrum to Voigt function. We review the setup to measure the linewidth. Due to the required long fiber delay in standard SHDI setup, a recirculating-SHDI is suggested for ultra-narrow linewidth measurement. In the next section, we discuss the laser design to obtain the optimal linewidth performance.

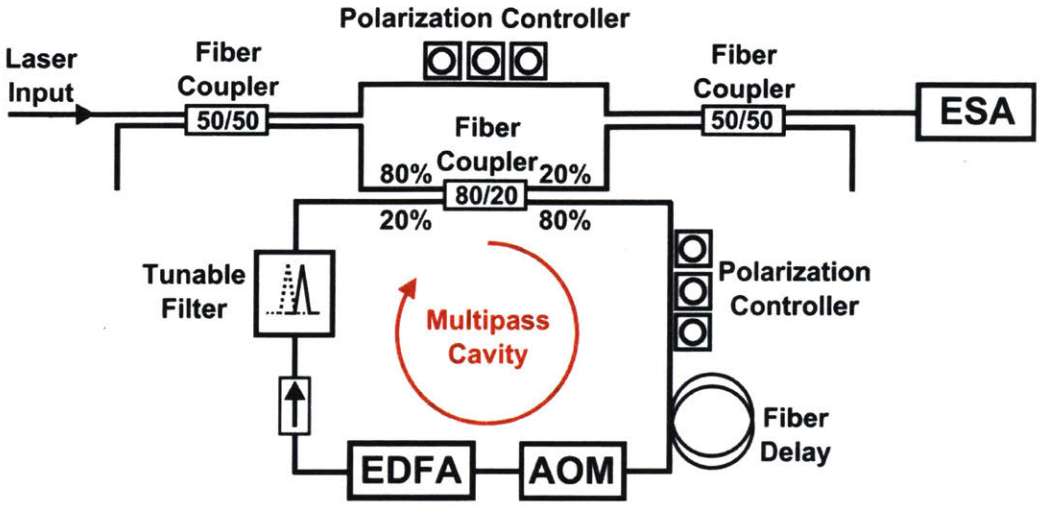

Figure 3-3: Recirculating self-heterodyne delayed interferometer for ultra-narrow-linewidth measurement.

3.2 Distributed phase shift design

In previous chapter, for a QPS-DFB design, a discrete quarter phase shift is formed at the center of the cavity with a sharp frequency resonance at the Bragg wavelength. The intense electric field concentrated around the phase shifted region may limit the performance of the laser due to spatial hole burning [35, 36] Alternatively, the phase shift in distributed phase shift (DPS) cavity [37] is continuously spread in a wider region, thus improving the uniformity of the field distribution and increasing the length of the effective gain section.

Figure 3-4a shows the transfer matrix calculation [38] of the intensity distribution along the DFB cavity in discrete and distributed phase shift structures. The DPS-DFB cavity can be constructed by adiabatically increasing/decreasing the index of the waveguide near the phase shifted region. We show that the intensity distribution has an even symmetry for the slowly increasing DPS structure (DPS (+)), and otherwise for DPS(-). With symmetric lobes around the center of the cavity, DPS (+) structure would experienced a reduced hole burning effect.

To design the grating structure in DPS-DFB, an asymmetric design with varying waveguide width $w_n(x)$ and periodic piece spacing $d_\kappa(x)$, where x is axis along the cavity, as shown in figure 3-4b. This allows accumulation of phase shift by sinusoidal

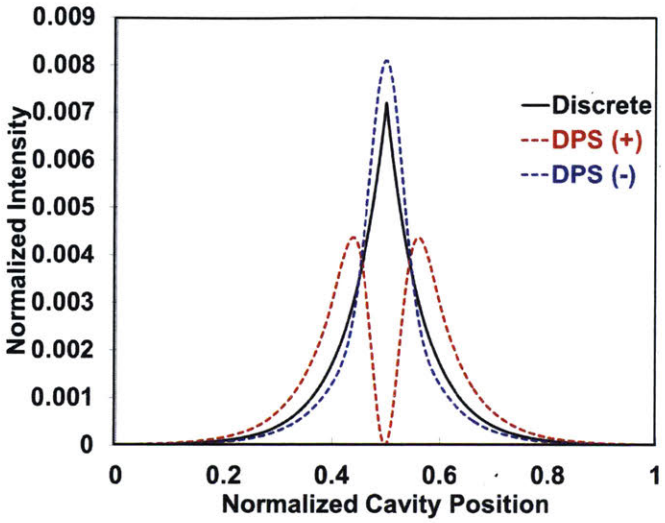

(a) DPS intensity distribution

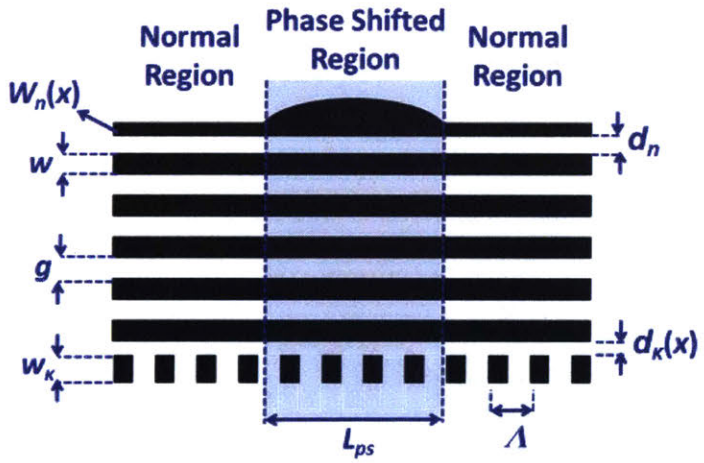

(b) DPS design

Figure 3-4: (a) Intensity distribution along the DPS-DFB cavity. (b) Design of Al_2O_3:Er^{3+}DPS-DFB laser with asymmetric grating structure.

increment of effective refractive index $\Delta n_{eff}(x)$ [17] while maintaining a constant grating strength κ in the phase shifted region with length L_{ps}. We use the coupled mode theory [38] to determine the right combination of $w_n(x)$ and $d_\kappa(x)$ for fixed gap distance $d_n = 250$ nm and periodic pieces width $w_\kappa = 300$ nm. We fabricated two different L_{ps} (0.2 cm and 0.4 cm) for grating period at 492 nm and $\kappa = 0.7$ cm^{-1}. For 0.2 cm DPS-DFB, $w_n(x)$ vary from $168 - 351$ nm and $d_\kappa(x)$ vary from $119 - 162$ nm. For 0.4 cm DPS-DFB, $w_n(x)$ vary from $168 - 271$ nm and $d_\kappa(x)$ vary from $140 - 162$

nm.

Figure 3-5b shows the spectrum of the best DPS-DFB from $L_{ps} = 0.4$ cm centered at $\lambda = 1565$ nm. A maximum output power of 5.43 mW is obtained, corresponds to SMSR > 59.4 dB. Figure 3-5a shows the comparison of power performance of the lasers. The longer L_{ps} DFB laser has almost double output power at maximum pump. The threshold power is > 4 times lower than QPS design ($P_{th} = 14$ mW) at wavelength around 1560 nm, with close to 5 times improvement in the slope efficiency ($\eta = 2.9\%$). These improvements can be attributed to a more uniform and longer active gain section in DPS-DFB.

We measure the linewidth of the DFB laser centered at $\lambda = 1566$ nm for QPS-DFB and $\lambda = 1565$ nm for DPS-DFB, as shown in figure 3-6. For QPS-DFB, the spectrum was collected at a center frequency of $f_c = 132$ MHz ($n = 3$), which corresponds to a total delay length of 105 km ($L_{delay} = 35$ km). For DPS-DFB, $n = 15$, $f_c = 660$ MHz, and effective $L_{delay} = 525$ km. To differentiate $1/f$ frequency (Gaussian) noise contribution, the measured spectra are fitted with Voigt function [30, 31]. The self-heterodyne spectra are plotted around f_c with the QPS-DFB presented in red color and DPS-DFB in blue color.

From the fitting of QPS-DFB linewidth, we obtain a FWHM of the Voigt function of $FWHM_{Voigt} = 66.1 \pm 2.5$ kHz. The Voigt linewidth is further decomposed into the Gaussian component $FWHM_{Gauss} = 18.4 \pm 7.9$ kHz and Lorentzian component $FWHM_{Lorentz} = 60.7 \pm 2.2$ kHz. The optical linewidth $\Delta\nu$ can be estimated from half the Lorentzian width of the spectrum, thus $\Delta\nu_{QPS} = \frac{1}{2} \times FWHM_{Lorentz} = 30.4 \pm 1.1$ kHz. For DPS-DFB, with the same analysis above we obtain $FWHM_{Voigt} = 23.8 \pm 0.7$ kHz, $FWHM_{Gauss} = 17.5 \pm 1$ kHz, $FWHM_{Lorentz} = 10.5 \pm 0.5$ kHz, and thus $\Delta\nu_{DPS} = 5.3 \pm 0.3$ kHz. The linewidth improvement in DPS-DFB ($\Delta\nu_{QPS} = 5.73 \times \Delta\nu_{DPS}$) can be attributed to a higher output power and reduction in spatial hole burning effect.

Thus, we have demonstrated narrow linewidthAl_2O_3:Er^{3+}DFB lasers in two different designs, QPS-DFB and DPS-DFB cavities. By using QPS-DFB configuration, we obtain maximum output power of 0.76 mW at 1566 nm with 200 mW pumping,

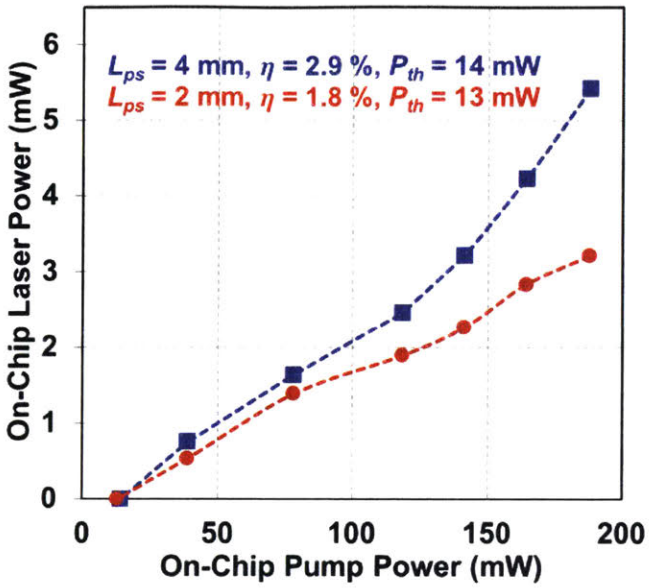

(a) DPS-DFB power measurement

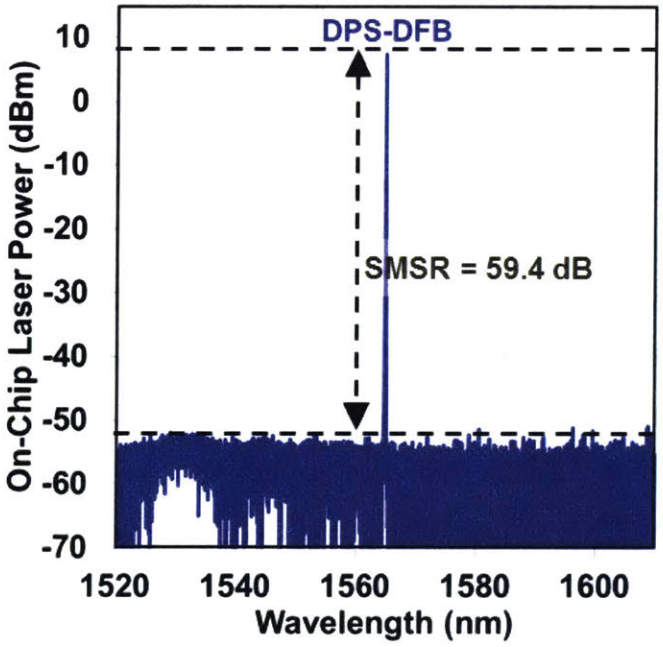

(b) DPS-DFB spectrum

Figure 3-5: (a) Output power of Al_2O_3:Er^{3+}DPS-DFB lasers vs. pump power for two different distributed phase shift lengths. (b) Optical spectrum of Al_2O_3:Er^{3+}DPS-DFB at 1565 nm.

as demonstrated previously in chapter 2. In a DPS cavity, we achieve an order of magnitude improvement in maximum output power (5.43 mW) at the same pump

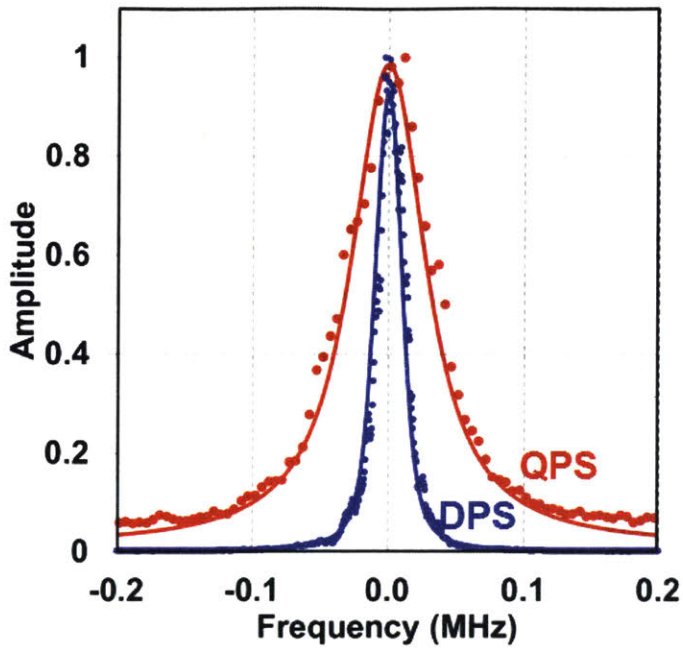

(a) Linewidth (linear)

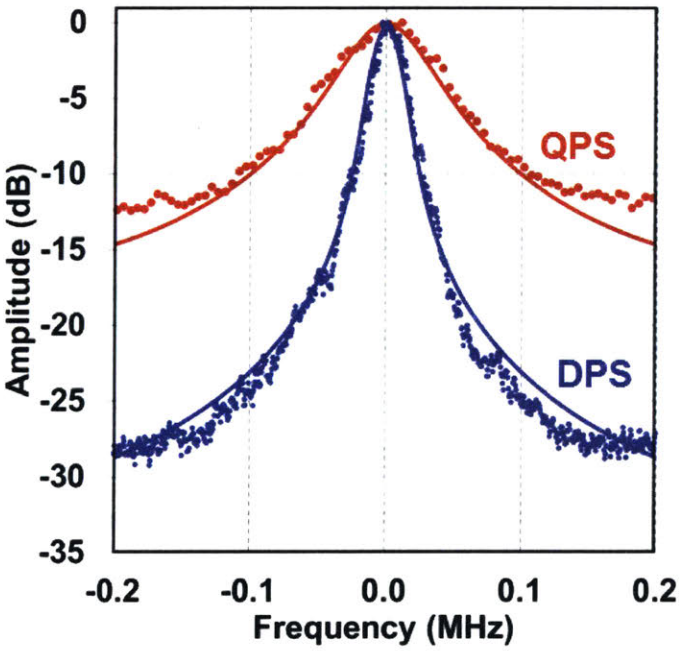

(b) Linewidth (dB)

Figure 3-6: Self-heterodyne spectrum of Al_2O_3:Er^{3+}DFB laser in for (red) QPS-DFB and (blue) DPS-DFB in (a) linear and (b) dB scale. The solid lines of the same color are the fitting of the corresponding measurements (dots).

power for wavelength centered at 1565 nm, corresponds to side mode suprresion ratio (SMSR) of $>$ 59.4 dB. Finally, we measure the optical linewidth with R-SHDI setup to obtain $\Delta\nu_{DPS} = 30.4 \pm 1.1$ kHz and $\Delta\nu_{DPS} = 5.3 \pm 0.3$ kHz. The overall improvement ($\sim$6 $\times$) of the DPS-DFB cavity can be attributed to the reduction of spatial hole burning in QPS-DFB cavity and therefore, a longer effective gain section. Even narrower linewidth can be achieved by mechanical stabilization of the setup, increasing the pump absorption efficiency, increasing the output power, or enhancing the cavity Q.

3.3 Summary

In summary, we have demonstrated a design for obtaining ultra-narrow linewidth laser. We briefly review the linewidth theory and measurement in a laser. Due to reabsorption loss in Al_2O_3:Er^{3+}laser, the modified Schawlow-Townes limit shows additional broadening to the frequency noise. We discuss the linewidth measurement setup that characterize the self-heterodyne spectrum of the laser. The setup measures two type of frequency noises (quantum and technical), in which it can be separated by fitting the self-heterodyne spectrum to Voigt function. We then provide two setups to characterize the frequency noise. Due to the required long fiber delay in standard SHDI setup, a recirculating-SHDI is suggested for ultra-narrow linewidth measurement.

We propose a distributed phase shift DFB design to obtain an ultra-narrow linewidth laser. Compared to QPS cavity, the DPS has the advantage of more uniform intensity distribution and longer effective gain section. From a 0.4 cm distributed phase shift length in a 2 cm DPS-DFB, we obtain maximum power of 5.4 mW, slope efficiency of 2.9%, threshold power of 14 mW, and linewidth of 5.3 $\pm$ 0.3 kHz at λ = 1565 nm. In QPS-DFB, at 1566 nm, we obtain maximum power of 0.76 mW, slope efficiency of 0.6%, threshold power of 65 mW, and linewidth of 30.4 $\pm$ 1.1 kHz. This shows the superiority of the distributed design compare to discrete design in Al_2O_3:Er^{3+}DFB laser.

Chapter 4

Reliable Laser Design

We present the results on reliable Al_2O_3:Er^{3+}laser design. The discussion is motivated by the observation of different distortions in the passive DFB cavity response on different chips from the same Al_2O_3deposition run. We investigate the influence of gain film thickness uniformity on cavity Q and threshold power in Al_2O_3:Er^{3+}DFB laser. We show that even for thickness variation of $< 0.5\%$, the cavity response can be highly distorted with significantly reduced Q. We propose a compensation scheme based on a curved DFB structure. Under the same grating parameters,we achieve $>$ 6 times lower threshold power compared to a straight DFB laser. The reliability of the design and alternative approaches are also discussed.

4.1 Distortion in straight DFB laser

We perform transmission measurement of a DFB cavity with length 23 mm and $\kappa = 0.3$ cm^{-1} at various chips from the same wafer (Edouard). All the chips are placed randomly in the same deposition platform on the same run. Figure 4-1 shows the transmission measurement of four chips marked by the position at the wafer. For the same DFB cavity, the transmission response is varying from chip to chip, and only one of the chip show lasing. The cavity Q is also shown to vary, from 8×10^4 to 4×10^5 for doping concentration of 1.5×10^{20} cm^{-3}.

Motivated by this observation, we repeated our waveguide fabrication process

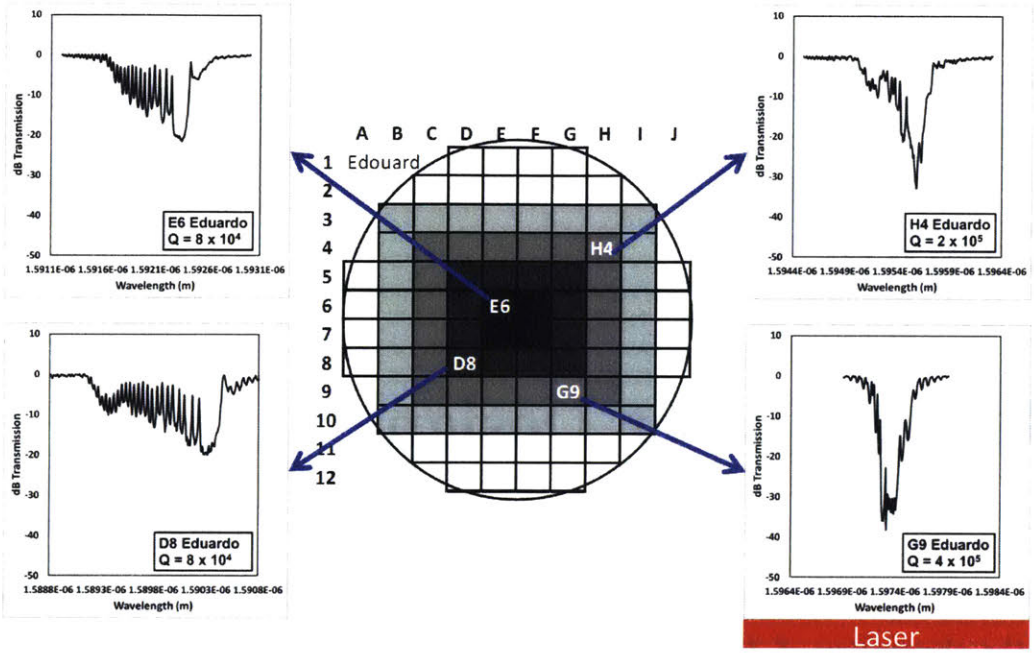

Figure 4-1: Transmission measurement of DFB cavity at various chips on the same Al_2O_3:Er^{3+}deposition run.

for several more runs to investigate the reliability of design. Figure 4-2 show the selected undoped and doped DFB cavity response. The resonances are located around 1595 nm. We estimate the absorption cross section for both gratings to be σ_{abs} = 0.2 × 10^{-21} cm^2, correspond to absorption of 0.13 dB/cm (Q_{abs} = 2.1 × 10^6). From the measurement, $Q_{undoped}$ = 1.4 × 10^6 and Q_{doped} = 4 × 10^5. This shows $\frac{1}{Q_{doped}} \simeq \frac{1}{Q_{undoped}} + \frac{1}{Q_{abs}}$, which indicates the loss of the doped cavity consist of the absorption by the erbium in the host and the intrinsic DFB cavity loss (scattering and outcoupling).

We hypothesize the source of the varying quality of the cavity is from the thickness nonuniformity in the Al_2O_3deposited layer. We measure the thickness variation of Al_2O_3film deposition in AJA Orion sputtering system. The target sample is mounted on a 5 cm radius rotating platform and thickness measurements are performed by prism coupling at various distances R from the center of the platform. Several film depositions in the range of 1000-1500 nm are normalized as shown in figure 4-3a. The uniformity of the film is reduced as it gets further away from the center. The data are

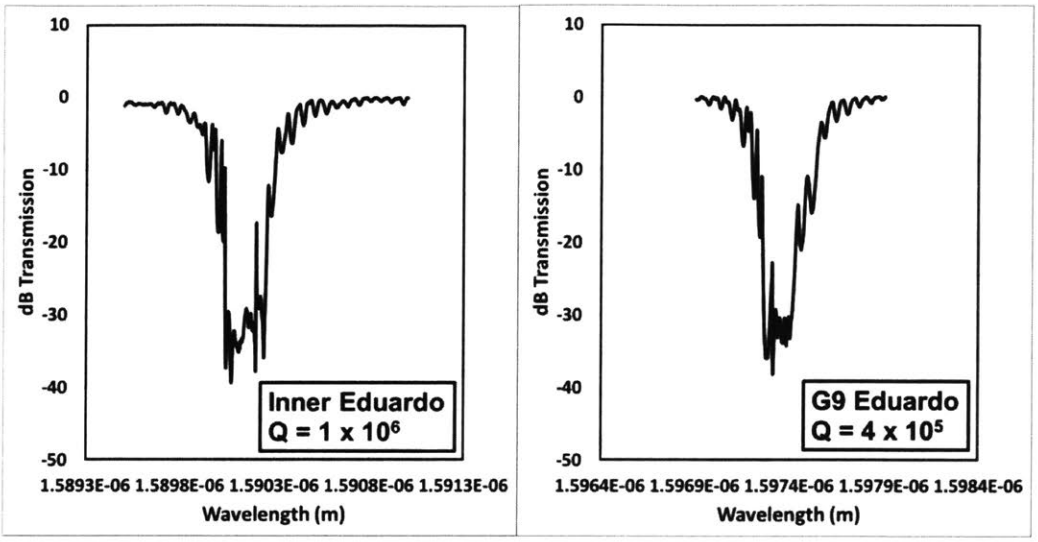

(a) Undoped DFB (b) Doped DFB

Figure 4-2: Transmission measurement of selected (a) undoped and (b) doped DFB cavities.

fitted with quadratic polynomial function, estimating 12% maximum variation across the platform.

Figure 4-3b illustrates geometry of the deposition of straight DFB structure in a rotating platform. Different part of the structure is located at varying distance r from the center O, thus inducing thickness variation along the device. Furthermore, a non-zero tilt angle α can introduce additional skew to the profile. This misalignment can also be interpreted as translational error of (x_{shift}, y_{shift}) from position where α = 0 (point A). The parameters can be calculated by the following equations.

$$r_{(d)}^2 = (R + d\sin\alpha)^2 + (d\cos\alpha)^2 \tag{4.1}$$

$$x_{shift} = R(1 - \cos\alpha) \tag{4.2}$$

$$y_{shift} = R\sin\alpha \tag{4.3}$$

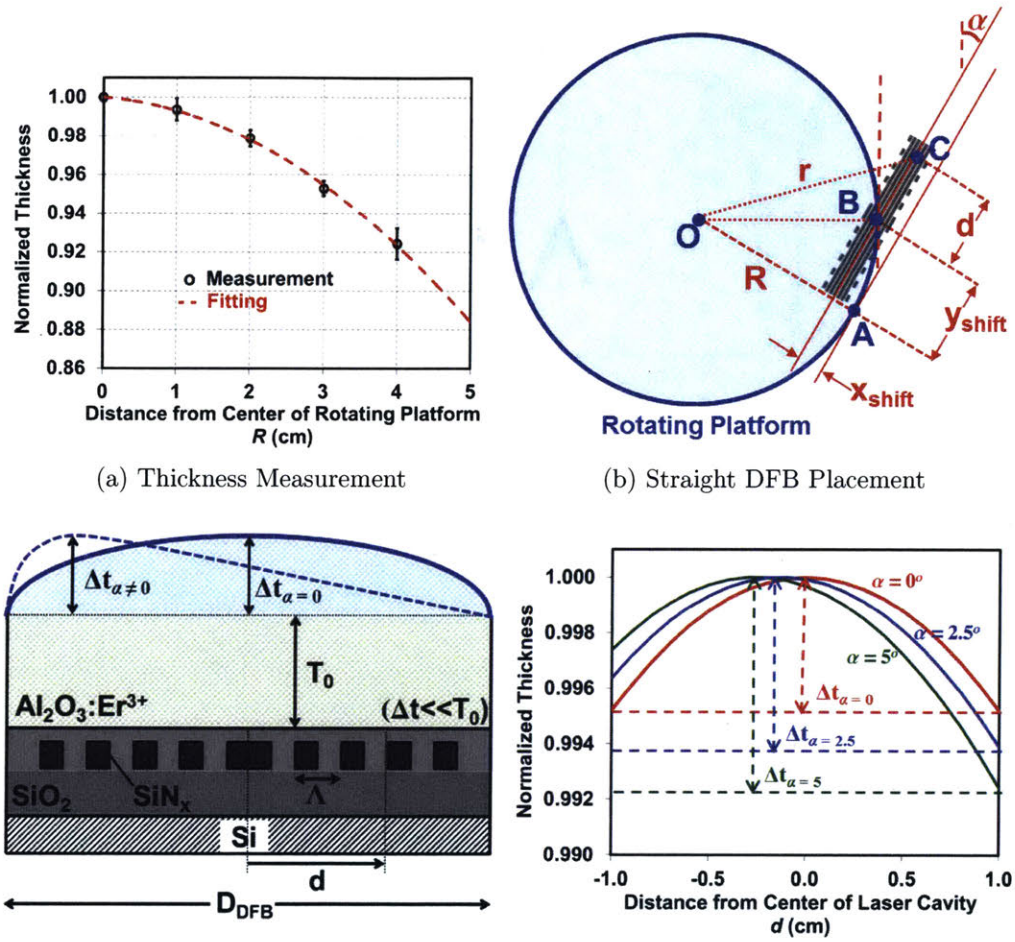

(a) Thickness Measurement

(b) Straight DFB Placement

(c) Side-view

(d) Thickness Profile

Figure 4-3: (a) Measurement (black) of the Al_2O_3thickness fitted with quadratic function (red) at varying distance from the center of the rotating platform. (b) Diagram of the straight DFB laser placement in a radially symmetric Al_2O_3film deposition process. (c) Illustration of thickness variation along the Al_2O_3DFB cavity. (d) Calculation of thickness profile in 2 cm long straight DFB cavity for various tilt angles at $R = 3$ cm.

where for a DFB with length of D_{DFB}, d is calculated from $D_{DFB}/2$ to $+D_{DFB}/2$.

The thickness variation along the DFB cavity is illustrated in figure 4-3. The cavity with length D_{DFB} with grating period Λ is deposited with base Al_2O_3:Er^{3+}thickness of T_0. The variation Δt along the cavity is skewed for $\alpha \neq 0$. We calculate for various tilt angles in $D_{DFB} = 2$ cm for positioning at $R = 3$cm, as shown in figure 4-3d. The thickness is normalized for $T_0 = 1100$ nm.We obtain a small nonuniformity of 0.5%,

0.5%, and 0.8% for $\alpha = 0^o$, 2.5^o, and 5^o respectively.

The influence of film thickness nonuniformity on cavity Q is investigated for different magnitude of the variations, as shown in figure 4-4. Using transfer matrix calculation, we calculate the transmission response of straight DFB cavity for various tilt angles (row-wise) and thickness variations (column-wise). The DFB is segmented into 1000 sections, with the effective index n_{eff} as a function of the film thickness at different d. The grating has strength $\kappa = 0.5$ cm^{-1}, length $D_{DFB} = 2$ cm, and total absorbtion loss $l = 0.5$ dB. The Q factor is determined from the ratio of the laser wavelength $\lambda = 1590$ nm with the 3-dB width of the resonance peak. We observe distortions in the response that reduce the cavity Q significantly compared to uniform thickness DFB ($Q_{max} = 1.07 \times 10^6$).

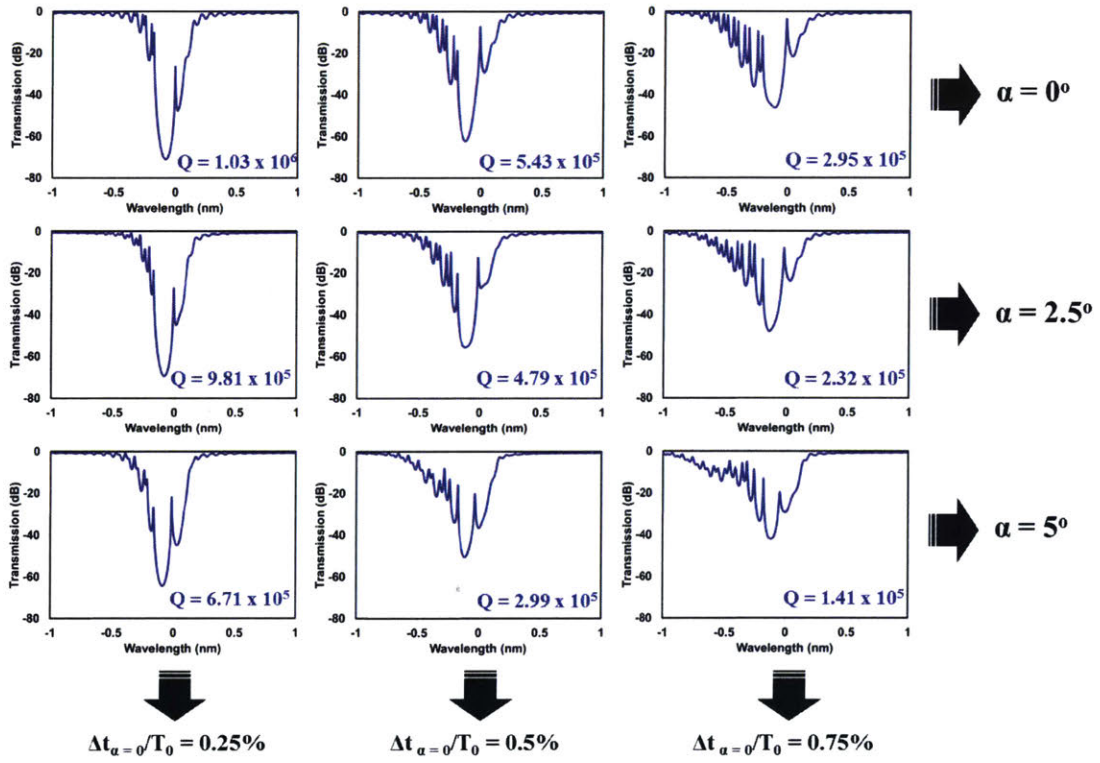

Figure 4-4: Calcuation of transmission response of straight 2 cm DFB cavity for various tilt angles and thickness variations at $R = 3$ cm.

In summary, we show the analysis of thickness nonuniformity on the performance of Al_2O_3:Er^{3+}laser. The thickness variation is presence in the radial symmetric depo-

sition of the sputtering system. Even for variation < 0.5%, a 2 cm DFB laser suffers significant distortions and reduced cavity Q. In the next section, we will discuss a laser design to compensate for the thickness variation.

4.2 Curved DFB structure

To compensate for the thickness nonuniformity in the deposition, we propose a curved DFB structure that follows the circular symmetry of the platform, as shown in figure 4-5a. By placing the curved DFB at $R = R_c$, the thickness profile can be maintained uniform throughout the cavity. Calculation of 2 cm DFB structure at various angles show that the profile is linear with smaller magnitude of variation, as shown in figure 4-5b. The radial distance r as a function of position in the device d is calculated by the following formulas.

$$r_{(d)}^2 = (x_{shift} + x'_{(d)} \cos\alpha + y'_{(d)} \sin\alpha)^2 + (y_{shift} - x'_{(d)} \sin\alpha + y'_{(d)} \cos\alpha)^2 \qquad (4.4)$$

where (x_{shift}, y_{shift}) denotes the relative position of the DFB curvature center (point O_c) to center of the platform (point O), and ($x(d)$,$y(d)$) is the position of a segment in the device (point C) observed point O_c. These parameters can be calculated by the following relations.

$$x_{shift} = R - R_c \cos\alpha \qquad (4.5)$$

$$y_{shift} = R_c \sin\alpha \qquad (4.6)$$

$$x'_{(d)} = R_c \cos(\frac{d}{R_c}) \qquad (4.7)$$

$$y'_{(d)} = R_c \sin(\frac{d}{R_c}) \tag{4.8}$$

Figure 4-6 shows the transmission responses of curved DFB cavity under the same parameters shown previously. The curved DFB can maintain symmetric responses and outperform the Q factors of straight DFB structure. The cavity Q only suffers noticeable degradation after a misalignment of $\alpha \simeq 5^o$ for $\Delta t_{\alpha=0}/T_0 > 0.5\%$. This shows the reliability of the curved DFB design against fabrication tolerance.

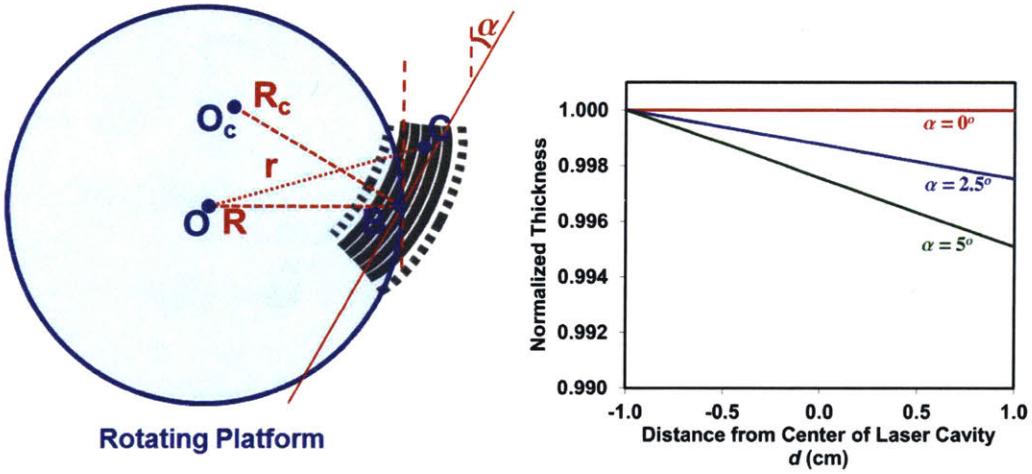

(a) Curved DFB Placement (b) Thickness Profile

Figure 4-5: (a) Diagram of the curved DFB laser placement in a radially symmetricAl_2O_3film deposition process. (b) Calculation of thickness profile in 2 cm long curved DFB cavity for various tilt angles at $R = R_c = 3$cm.

We compare the performance of straight and curved Al_2O_3:Er^{3+}DFB lasers fabricated on the same chip. The lasers are aligned manually at $R \simeq 3$ cm in the platform. We use a multi-segment wavelength-insensitive design that consists of a Si substrate, five SiN_xsegments (thickness of 200 nm, width of 450 nm, and gap of 400 nm), enclosed by a SiO_2layer (oxide gap of 200 nm), and Al_2O_3:Er^{3+}gain film (thickness $T_0 = 1100$ nm). A discrete quarter phase shift is formed at the center of each cavities to produce sharp resonances at Bragg condition. The grating unit is formed by additional periodic pieces on both sides with $\Lambda = 502$ nm ($\lambda_{laser} \simeq 1590$ nm). These periodic side pieces have width of 300 nm and gap distance of 350 nm. We use the prism coupling method to estimate background loss of < 0.1 dB/cm and

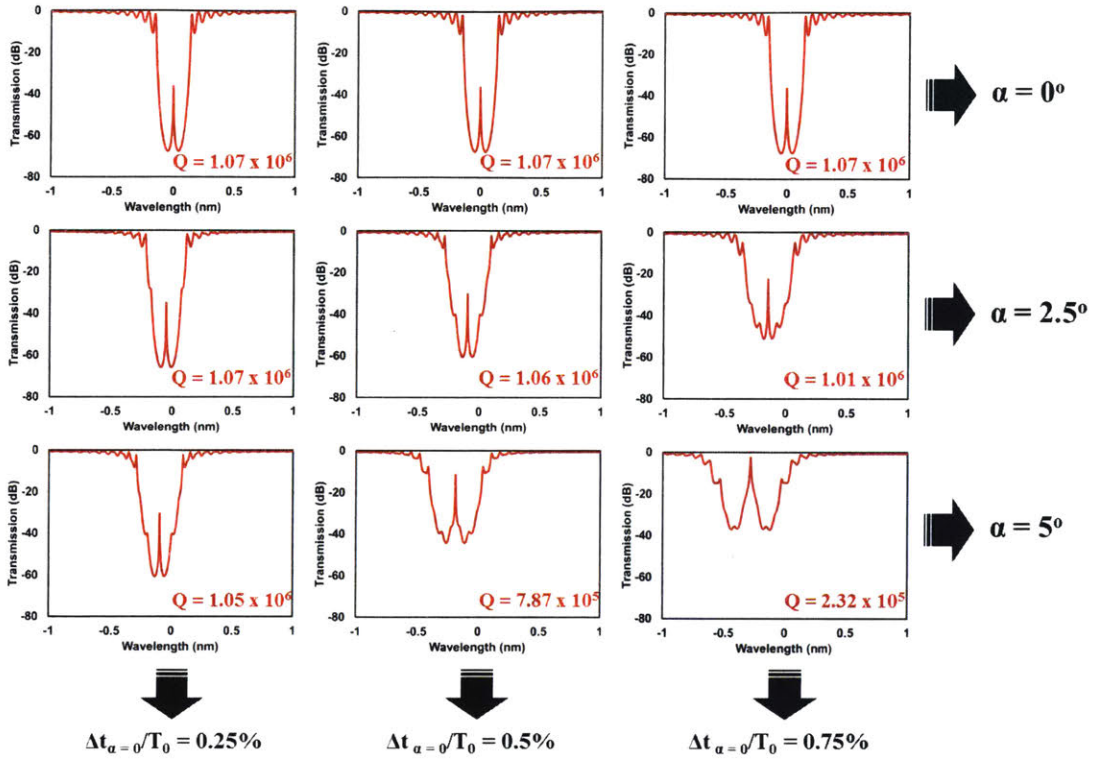

Figure 4-6: Calculation of transmission response of curved 2 cm DFB cavity for various tilt angles and thickness variations at $R = 3$ cm.

dopant concentration of 1.0×10^{20} cm^3.

Figure 4-7 shows the experimental setup of laser measurement. For curved DFB structure, the chip edge is angle-etched to provide normal incident coupling from fiber. Figure 4-8 shows the transmission measurement of the unpumped straight and curved DFB laser, respectively. The straight DFB structure contains similar features calculated in previous section, with many distortion peaks emerge in the blue-shift of the resonance wavelength. The resonance peak does not have a clear 3-dB width for Q estimation. The curved DFB structure shows a symmetric response, with measured $Q = 4.55 \times 10^5$.

We pump the DFB lasers from both sides using fiber pigtail laser diodes at 978 nm and 976 nm. Figure 4-9a shows > 6 times improvement in the threshold power for curved DFB ($P_{th} = 16$ mW) compare to straight DFB ($P_{th} = 105$ mW) lasers, with similar slope efficiency (0.6-0.7%). At total pump power of 188 mW, we obtain maxi-

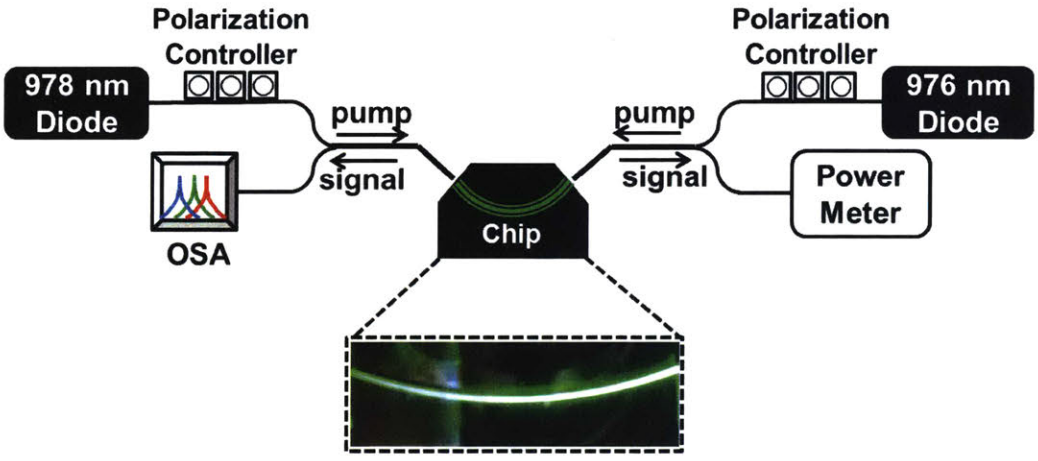

Figure 4-7: Experimental setup of curved DFB laser measurement

mum output power of 1.2 mW for curved DFB laser and less than 0.5 mW for straight DFB laser. Lastly, Figure 4-9b shows the spectra of both lasers, demonstrating SMSR of 55.7 dB for curved DFB laser.

In figure 4-10, we consider the sensitivity of 2 cm straight and curved DFB thickness profile to the position in platform. In straight DFB structure, the thickness variation is similar for all R, with magnitude of around 0.5%. In curved DFB structure ($R_c = 3$ cm), thickness variation $< 0.2\%$ can be obtained by placing 2 cm $< R <$ 4 cm. This reinforces the reliability of the curved DFB film deposition.

We also consider the effect of the device length. Q factors of straight DFB at various lengths are shown in figure 4-11a, for $\alpha = 0^o$, 2.5^o and 5^o. Shorter (< 1 cm) structures accumulate smaller thickness nonuniformity, thus providing a more reliable design for straight DFB cavity. However, to achieve a similar power efficiency, this might require a higher doping concentration which can be detrimental to the laser performance [19] due to the erbium limited solubility and clustering.

Alternatively, the thickness variation can be compensated by using index-varying waveguide design. The SiN_xwaveguide width can be adjusted along the cavity to provide small index perturbations. This approach would require additional initial calibration in the deposition system to provide the right compensating value in the device.

Thus, we show a simple design by curving the DFB laser to compensate for the

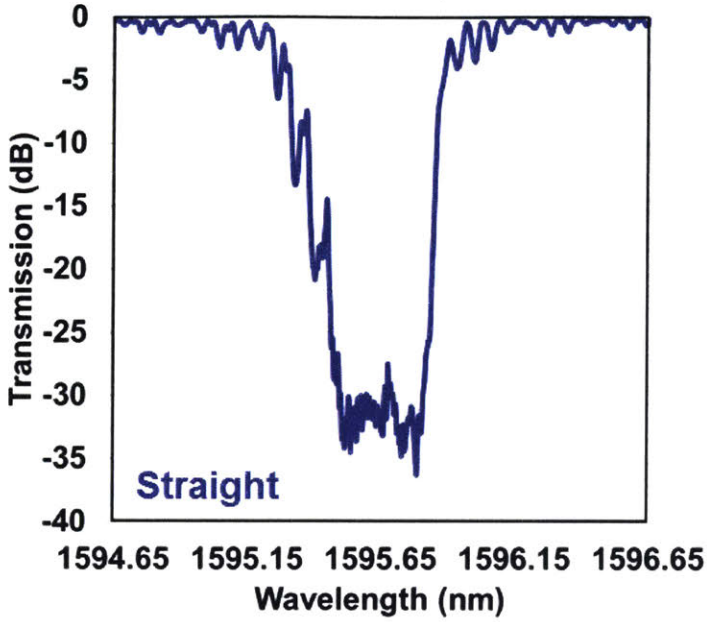

(a) Straight DFB Measurement

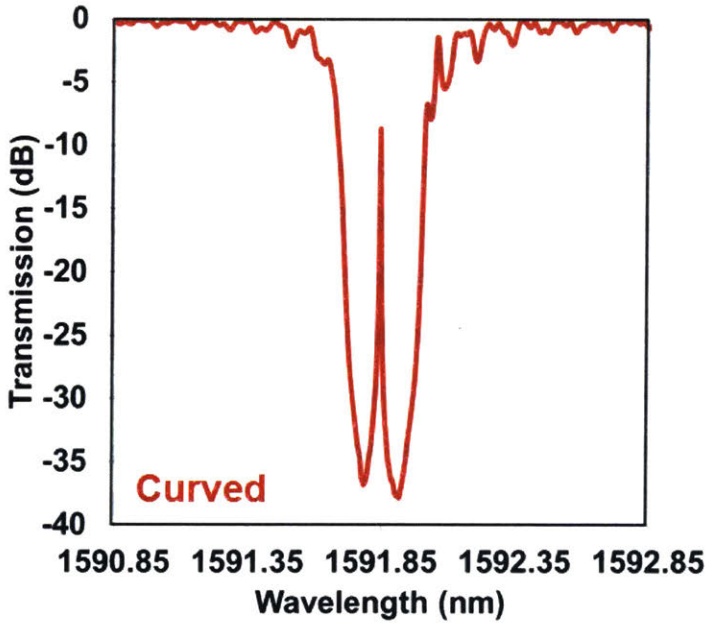

(b) Curved DFB Measurement

Figure 4-8: Transmission measurement of (a) straight and (b) curved Al_2O_3:Er^{3+}DFB lasers

radially symmetric Al_2O_3fabrication process. We obtain obvious improvement in the transmission response and cavity Q that results in lower threshold DFB laser. We

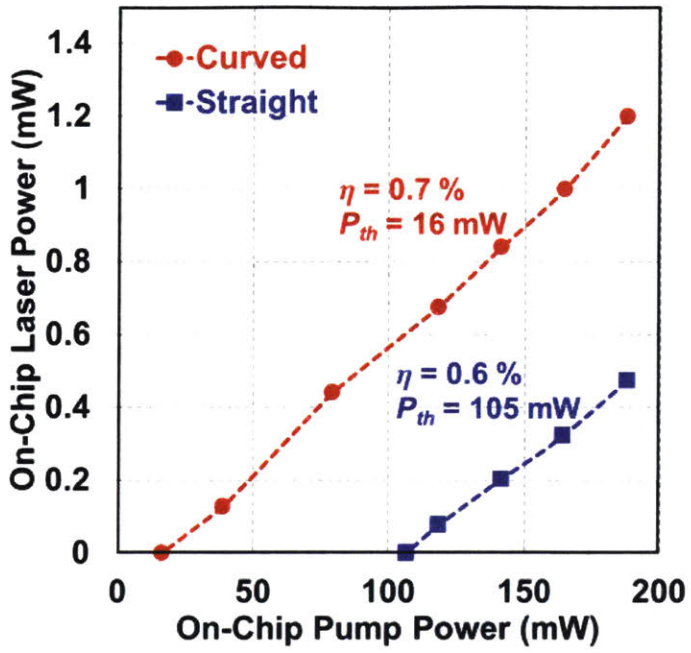

(a) Straight DFB Measurement

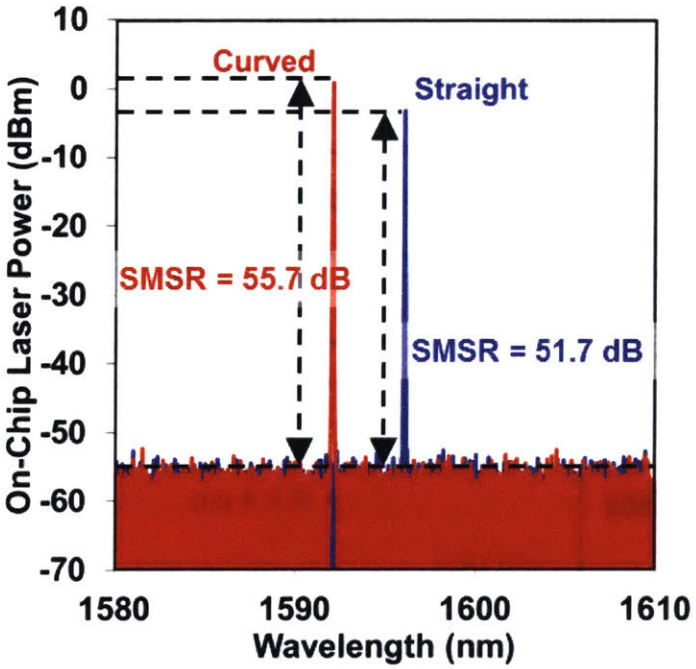

(b) Curved DFB Measurement

Figure 4-9: (a) Comparison of output powers of straight and curved DFB lasers at different pump powers. (b) Optical spectrum of straight and curved DFB lasers.

also show that the design is more tolerant to misalignment, thus demonstrating a reliable way to fabricate the Al_2O_3:Er^{3+}laser. Alternative approaches such as shorter DFB laser and index compensating cavity are also discussed.

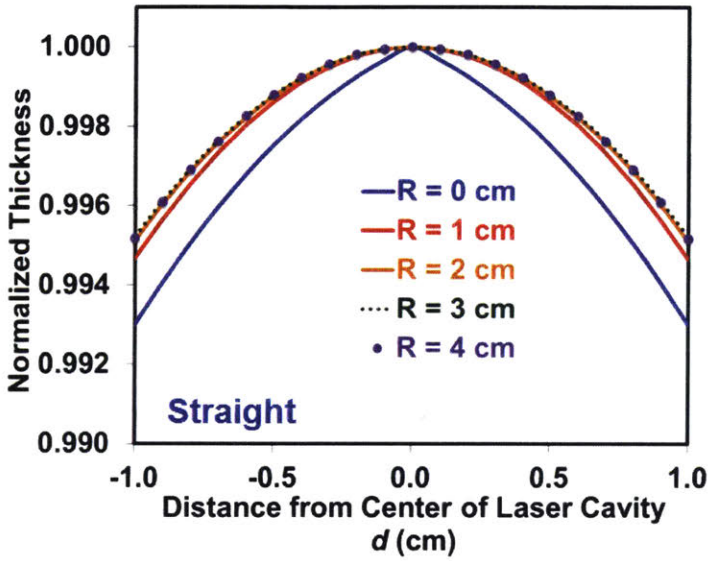

(a) Straight DFB Measurement

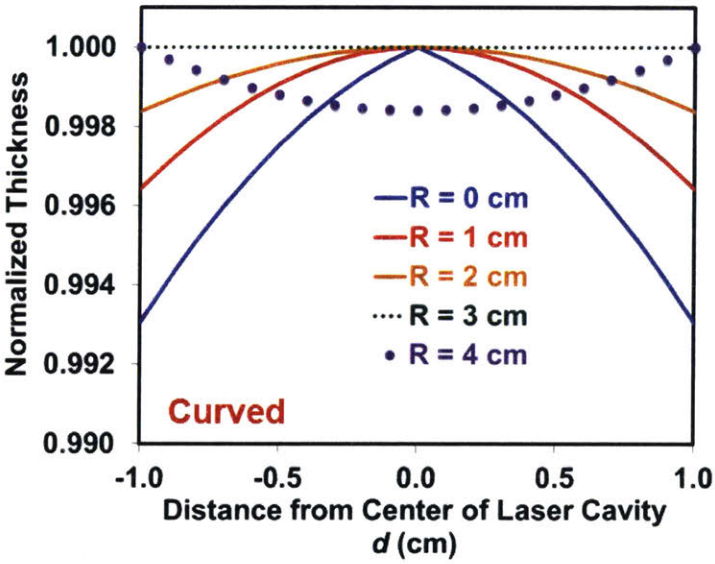

(b) Curved DFB Measurement

Figure 4-10: (a) Calculation of thickness profile for straight DFB with $\alpha = 0^o$ at various radial distance R from the platform center. (b) Calculation of thickness profile for curved DFB with $R_c = 3$cm and $\alpha = 0^o$ at various radial distance R from the platform center.

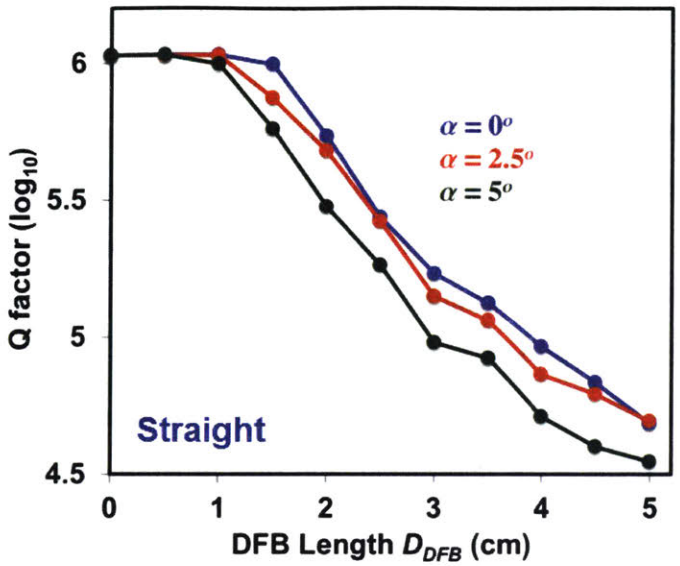

(a) Straight DFB Measurement

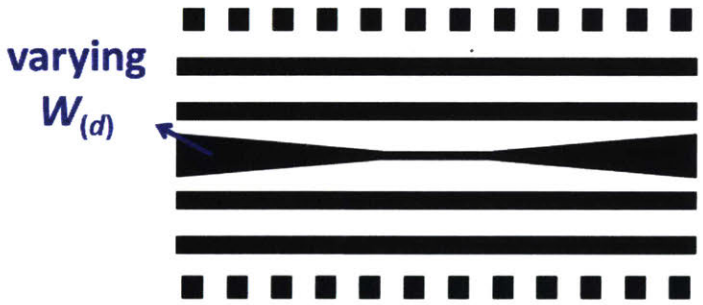

(b) Curved DFB Measurement

Figure 4-11: (a) Plot of Q factor of straight DFB for various DFB lengths at $R = 3$ cm. (b) Illustration of index-varying waveguide design.

4.3 Summary

In summary, we have demonstrated a design for reliable Al_2O_3:Er^{3+}laser. We measure the same DFB structure on different chips from the same wafer on the same deposition run and obtain varying transmission responses that affect the reliability of the performance. Through the analysis of the thickness variation in the sputtering system, we show a thickness variation of $\sim 0.5\%$ in a 2 cm straight DFB cavity. By transfer matrix calculation, we calculate that even $< 0.5\%$ thickness variation, the

transmission response of DFB can be highly distorted with significantly reduced Q.

We propose a compensation scheme based on a curved DFB structure that follows the circular symmetry of the deposition. Under the same grating parameters, the curved design outperforms the conventional straight DFB structure. We achieve slope efficiency of 0.7%, threshold power of 16 mW, and maximum output power of 1.2 mW for curved DFB laser. In straight DFB laser, we obtain slope efficiency of 0.6%, threshold power of 105 mW, and maximum output power of 0.5 mW, demonstrating $>$ 6 times threshold power improvement. The curved DFB laser is shown to be more tolerant to misalignment in the deposition, and thus providing a reliable approach for on-chip Al_2O_3:Er^{3+}laser.

Alternative approaches to construct a reliable laser are shorter DFB device and index compensated cavity. Such approaches however are limited by other requirements, such as higher doping concentration and calibrated measurement of the thickness variation in sputtering system.

Chapter 5

Application of Al_2O_3:Er^{3+}Laser

We present the results on design of Al_2O_3:Er^{3+}laser for application in some use cases. First, we demonstrate monolithic integration of a wavelength division multiplexed (WDM) light source for silicon photonics by cascade of Al_2O_3:Er^{3+}DFB lasers. Four DFB lasers with uniformly spaced emission wavelengths are cascaded in series to simultaneously operate with no additional temperature tuning required. Then we show the integration of Al_2O_3:Er^{3+}laser in a 3D integrated silicon photonics platform by using an erbium trench layer to passivate the gain medium from other devices. We demonstrate laser operation working along with other silicon photonics devices on the same chip.

5.1 WDM light source by cascade of DFB laser

A wavelength division multiplexed (WDM) light source is a key component in silicon photonics technology for application in optical communications [39, 40, 41]. It generally consists of several uniformly spaced optical wavelengths that can be used to encode multiple communication channels in a common output. Several research groups have demonstrated integrated WDM light sources of up to 16 channels by bonding of III-V gain material onto the silicon chip [42, 43, 44, 45, 46]. However, these hybrid devices often require careful temperature control and complex fabrication steps with yield challenges.

Alternatively, rare earth doped glass lasers on silicon, such as Al_2O_3:Er^{3+}DFB laser , have been shown to achieve low noise, good thermal stability and high output power. By combining several lasers with varying grating periods, a multi-wavelengths light source can be obtained with custom longitudinal mode spacing.

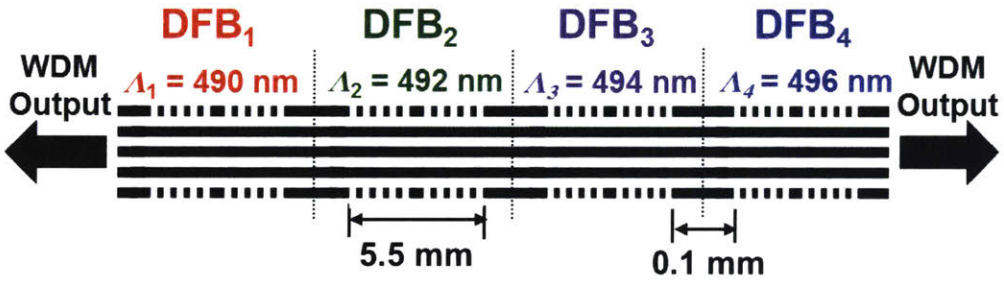

Figure 5-1: Design of WDM light source by cascaded DFBs. Four erbium DFB lasers at uniformly spaced grating period are cascaded in series to generate multi-wavelengths laser output.

In this chapter, we demonstrate a monolithic WDM source by cascading four Al_2O_3:Er^{3+}DFB lasers. The design of the cascaded-DFB structure is shown in figure 5-1. Four DFB lasers are cascaded in series with the length of each laser L_{DFB} = 5.5 mm, distance between each laser $L_{spacing}$ = 0.1 mm, and first grating period Λ_1 = 490 nm with 2 nm subsequent increment (Λ_2 = 492 nm, Λ_3 = 494 nm, and Λ_4 = 496 nm). Each DFB laser has a quarter phase shift located at the center, thus emitting symmetric outputs on both sides. The right output from DFB_1 propagates to the next laser DFB_2, and so on to the right end of the structure. The combined output is then a WDM of four uniformly spaced wavelengths. In order to design an asymmetric output that emits on only one end of the device, the phase shift can be placed to be slightly off-centered in the cavity. With small reabsorption loss (0.5 dB/cm at 1563 nm) and good thermal stability of the Al_2O_3:Er^{3+}laser, the lasers can be placed closely with with negligible cross talk.

To form a compact CMOS compatible cascaded-DFB structure, we optimized the multi-segmented waveguide design for short lasers. The laser waveguide consists of five silicon nitride (SiN_x) segments with the grating perturbation formed by periodic etching of the first and last segments. The SiN_xsegments have dimensions of thickness

$t = 200$ nm, width$w = 450$ nm, and gap $g = 400$ nm. A SiO_2gap $g_{ox} = 200$ nm is then added on top of the SiN_xstructure. Lastly, the Al_2O_3:Er^{3+}gain medium of thickness $t_{AlO} = 1100$ nm is deposited by a reactive co-sputtering process as the final backend step. The erbium ion concentration is $N_{Er} = 1.0 \times 10^{20}$ cm^{-3} and the background loss is measured to be < 0.1 dB/cm, using the prism coupling method.

We measure the transmission response of the cascaded-DFB structure as shown in figure 5-2a. Sharp resonances are located at the center of each DFB response at wavelengths $\lambda_1 = 1563.56$ nm, $\lambda_2 = 1569.84$ nm, $\lambda_3 = 1575.90$ nm, and $\lambda_4 = 1581.76$ nm. The wavelength spacings between adjacent DFBs are slightly non-uniform ($\Delta\lambda_{adjacent}$ = 6.28 nm, 6.06 nm, and 5.86 nm). We believe that this can be explained by the thickness non-uniformity of the Al_2O_3:Er^{3+}film deposition. Due to the circular symmetry of the reactive sputtering process, long straight structures may suffer from variations in film thickness, as described in chapter 4.

Laser measurements were carried out by pumping the cascaded-DFB structure from both sides with two fiber pigtailed laser diodes centered at 978 nm (left side) and 976 nm (right side). Accounting for fiber-chip coupling losses, the maximum on-chip pump powers of the 978 nm and 976 nm diodes are estimated to be 120 mW (left pump) and 70 mW (right pump) respectively. The output is monitored using two optical spectrum analyzers (OSA) on both sides.

We obtain laser wavelengths centered at 1563.92 nm, 1570.20 nm, 1576.28 nm, and 1582.16 nm, slightly higher than the passive transmission measurement due to local heating by pump absorption. The peak output powers obtained in the left (and right) OSA for the four DFBs are as follow: 17.7 dBm (17.4 dBm), 20.4 dBm (20.2 dBm), 22.1 dBm (22.6 dBm), 19.1 dBm (24.0 dBm). The measured power from the left and right OSA generally show similar output levels, except for DFB_4, which is still in investigation. We plot the total emission spectrum of the cascaded DFBs by adding the spectrum obtained from both left and right OSA in figure 5-2b. The total peak power obtained for different wavelengths are 14.5 dBm, 17.5 dBm, 19.4 dBm, and 18.0 dBm. This corresponds to a total cascaded DFB output power of 10.9 dBm from all four DFBs, an average of 16.9 dBm per DFB. By assuming the noise floor

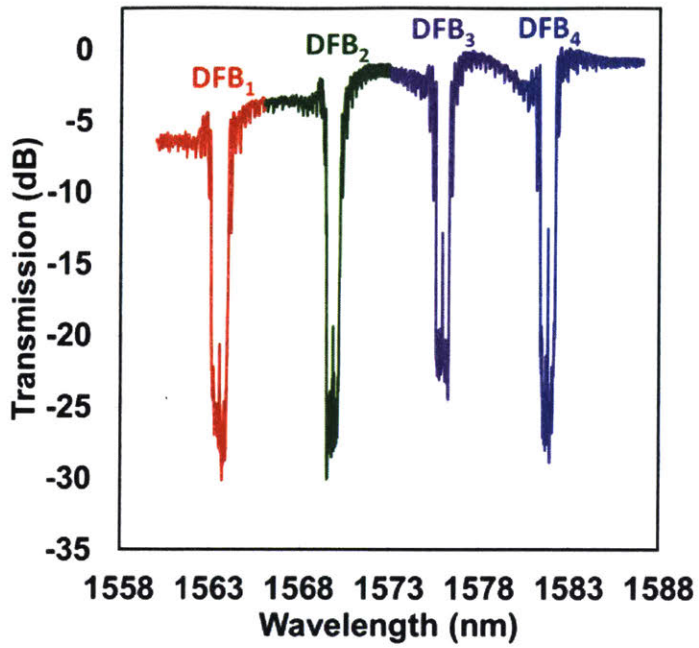

(a) Transmission Measurement

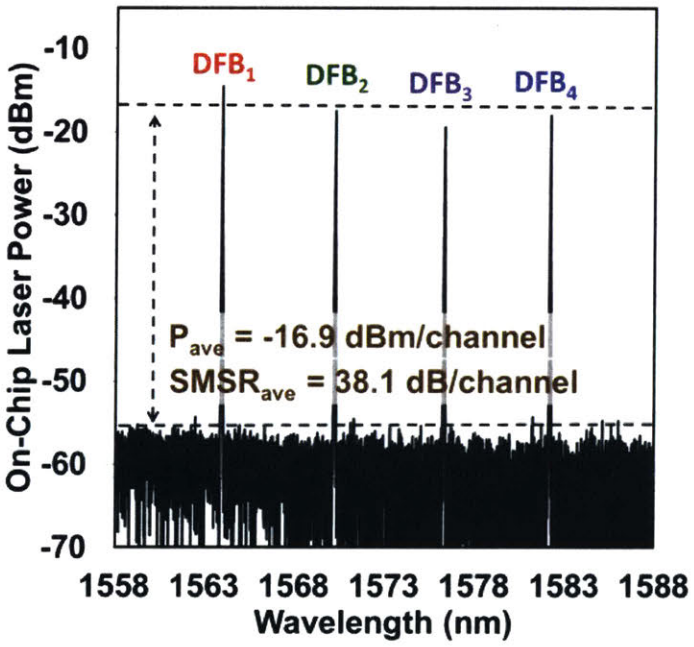

(b) Spectrum

Figure 5-2: (a) Transmission measurement of cascaded-DFB structure. (b) Total emission spectrum of the cascaded-DFB WDM source at maximum pump power.

at -55.0 dBm as shown in figure, we obtain an average of 38.1 ± 2.5 dB SMSR per DFB, which is to our knowledge, one of the best signal to noise performances of a on-chip WDM light source ever reported [44].

We perform a temperature dependence test of the cascaded DFBs by placing the chip on a thermoelectric cooler (TEC). The TEC temperature can be adjusted from 20 to 50 °C by varying the current level. Figure 5-3a shows the spectrum of DFB1 at temperatures of 20, 30, and 40 °C. No significant change of the output power is observed at varying temperatures, demonstrating thermal stability of the Al_2O_3:Er^{3+}lasers. Figure 5-3b shows the wavelengths of all four DFBs at varying temperature with an uniform temperature-dependent shift of $\frac{d\lambda}{dT} = 0.015$ nm/°C across all four lasers.

Improved performance of the cascaded DFB laser WDM light source can be achieved in the following ways. The maximal output of each DFB laser can be optimized by varying the grating strength κ and cavity length L_{DFB}, as shown in [47]. The pump laser can be recirculated by using a selective reflector to obtain a more flattened spatial pump profile. In addition, by taking into account the doping concentration, reabsorption loss, and total available pump power, the combined WDM output can be carefully designed to have better power uniformity. Lastly, to scale the cascaded-DFB to include more DFB lasers, several structures can be combined in parallel or the structure can be folded around the chip to increase the total available length (here the design was constrained by the chip length of 2.5 cm).

In summary, we have demonstrated CMOS-compatible monolithic integration of a WDM light source in a silicon photonics platform by cascade of Al_2O_3:Er^{3+}lasers. Simultaneous operation of four DFB lasers has been achieved and the output shows good thermal stability with varying chip temperatures (20−40 °C), with a uniform temperature dependent wavelength shift of 0.015 nm/C across all four DFBs. We propose that such Al_2O_3:Er^{3+}lasers are an alternative approach to low noise and thermally stable WDM light sources for optical communications.

Temperature insensitive operation of optical interconnects has been actively investigated in recent years [48, 49]. By using multiple Al_2O_3:Er^{3+}DFB lasers and SiN_xring filters with equal channel spacing ($\Delta\lambda_{laser} = \Delta\lambda_{filter}$), we propose an opti-

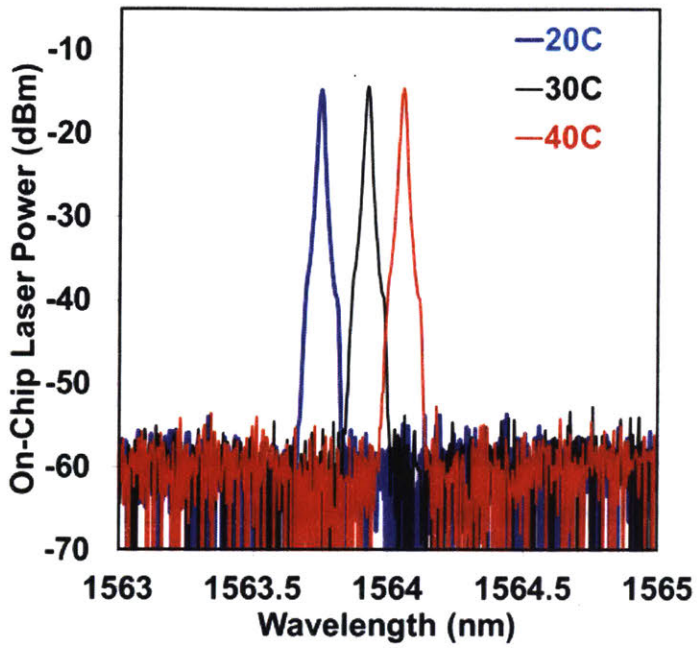

(a) Temperature Shift Spectrum

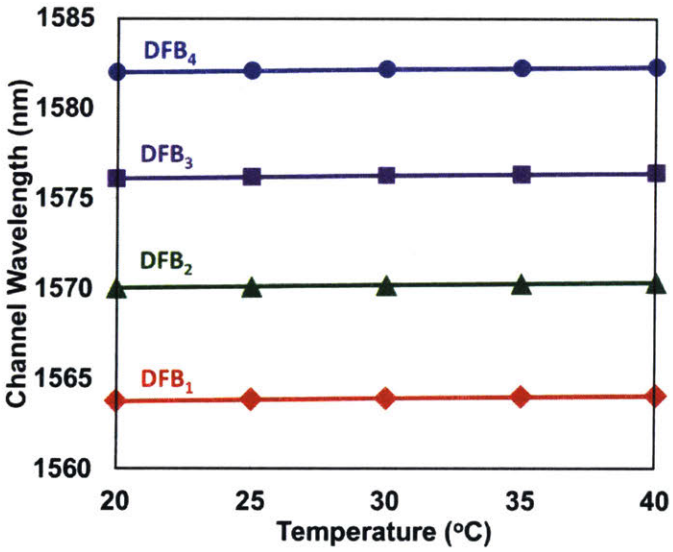

(b) 4 DFB Shift

Figure 5-3: (a) The spectra of Al_2O_3:Er^{3+}DFB laser outputs and SiN_xring filter drop responses at 20°C and 50°C. (b) Plot of frequency shift of the laser and filter at various temperatures.

cal transceiver scheme as shown in figure 5-4. The outputs from $N = k \times n$ number of regularly spaced lasers are combined into one waveguide. This waveguide is then

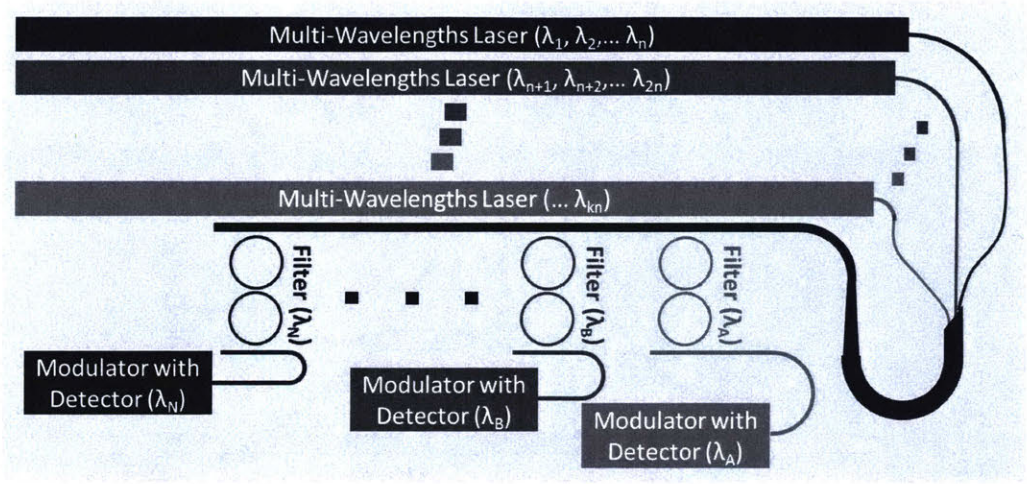

(a) Temperature Control Free Optical Interconnect

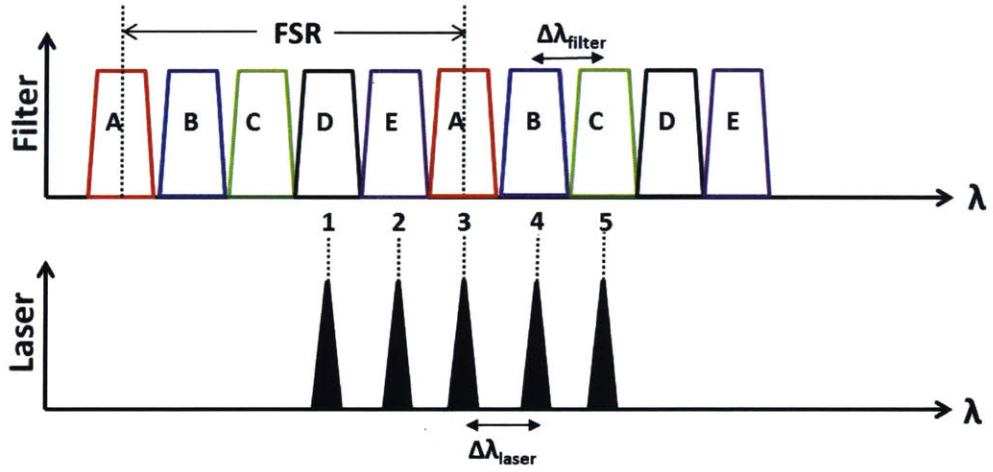

(b) Frequency Filtering Scheme

Figure 5-4: (a) Conceptual diagram of the proposed Al_2O_3:Er^{3+}lasers and SiN_xfilters-based optical transceiver. (b) Schematic responses of drop ports and laser outputs from five filters and DFB lasers, respectively. If the wavelength spacing is equal ($\Delta\lambda_{laser} = \Delta\lambda_{filter}$), there would be a one-to-one correspondence of the laser and the filter, e.g. 1 to D, 2 to E, 3 to A, 4 to B, and 5 to C.

passed through N filters with each output proceed to the modulator and detector for that wavelength. If the channels span across entire free spectral range (FSR), then there would be a one-to-one correspondence of the laser and the filter. Furthermore, a temperature control free operation is possible since both Al_2O_3:Er^{3+}lasers and SiN_xfilters have small and almost equal thermal characteristics.

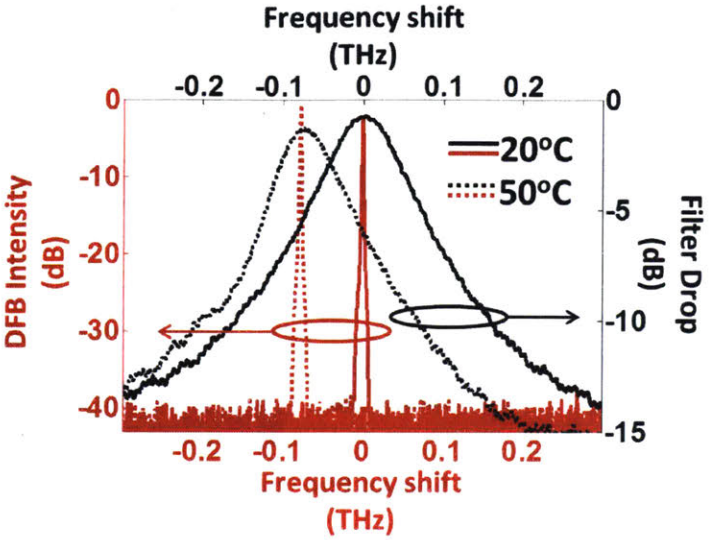

(a) Spectrum of Temperature Dependent Shift

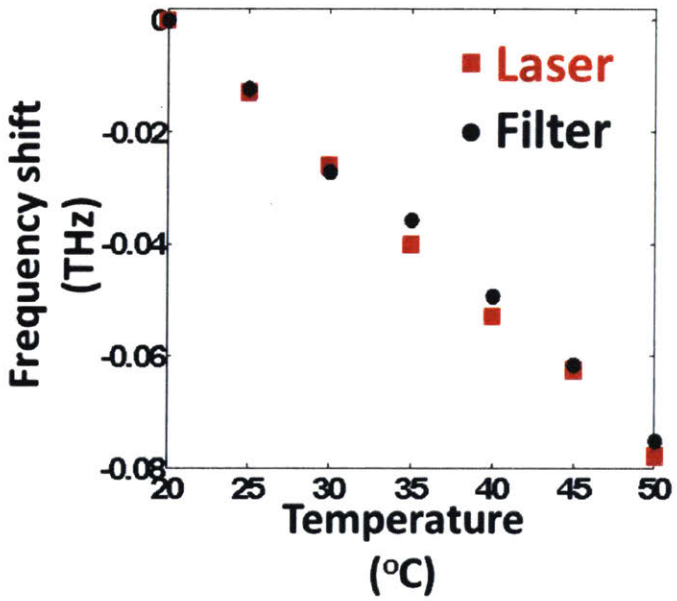

(b) Frequency vs Temperature

Figure 5-5: (a) Spectrum of DFB laser and ring filter. (b) Frequency shift of DFB Laser and silicon nitride ring filter at varying temperature.

The filter here consists of two PECVD SiN_xrings (radius $R = 30$ μm), both at the same thicknesses of 200 nm and widths of 1 m. The nitride layers are separated by 100 nm SiO_2. The filter is coupled symmetrically from both sides by bus waveguides made from two SiN_xwaveguides of widths 1 μm at equal gap distances of 200 nm. The ring filter has 3-dB bandwidth of 114 GHz at 1567 nm.

We measured the spectra of the DFB outputs and drop responses at various temperatures. In figure 5-5a, we aligned the laser and filter spectra plot at 20°C. The temperature dependent frequency shifts are then compared at 50°C. The frequency change is almost synchronized, demonstrating the potential for on-chip optical transmitter operation without temperature control. A finer measurement of the frequency shifts at various temperature points is shown in figure 5-5b. The fitting of the frequency shift of the Al_2O_3:Er^{3+}laser (2.57 GHz/°C) is measured to be within 4% difference from the SiN_xring filter (2.47 GHz/°C).

Thus, we demonstrated the feasibility of a temperature control free optical transceiver by using Al_2O_3:Er^{3+}DFB laser and SiN_xring filter. The temperature dependent frequency shift of the laser is shown to be almost synchronous with the ring filter over temperature range of 20°C to 50°C.

5.2 Erbium laser in full platform

So far, we have demonstrated Al_2O_3:Er^{3+}lasers on a dedicated platform for laser devices. The stack consists of only several layers such as SiN_x, $SiO_2$and Al_2O_3:Er^{3+}film. In a full silicon photonics platform, the layer stack can easily have more than a dozen to hundred of layers with additional steps such as n/p doping, annealing, metal/via, and other silicon photonics or electronic devices. The layer stack process thus has to designed to allow all the devices to work on the same chip.

In hybrid III-V and Si laser, various integration schemes of the laser has been demonstrated, as shown in figure 5-6. One approach is to use Indium Phosphate as the interface material to bond both the III-V laser and the Si chip (figure 5-6a) [15]. Another approach is to align and bond the semiconductor optical amplifier (SOA)

on the substrate (figure 5-6b) [44]. Both of these approaches require a nontrivial alignment step that complicates the integration process and reduce the production yield. An alternative approach to improve the alignment accuracy is to create trenches for the III-V material. It still requires bonding and SiO_2passivation steps to secure the gain material, and the resulting yield is still not clear [50].

In this work, we demonstrate an integration scheme of Al_2O_3:Er^{3+}laser witthout any alignment step by using an erbium trench structure. The erbium trench is patterned by the same lithography process for the laser waveguide. Figure 5-7a illustrates the full platform integration scheme of Al_2O_3:Er^{3+}laser. The step-by-step process of fabricating the laser devices with erbium trench is shown in figure 5-7b. First, we start with two layer of SiN_x. The top SiN_xlayer acts as the etch marker for the trench. Depending on the waveguide cross section, additional SiO_2layer can be deposited in the trench. Lastly, the Al_2O_3:Er^{3+}layer deposition remains to be the last backend step as before.

We implement the integration scheme of Al_2O_3:Er^{3+}laser on a full silicon photonics platform by using the quarter phase shift DFB design discussed in chapter 2. The width of the erbium trench is designed to be 50 μm wide. We obtain lasing at 1560 nm (figure 5-8) working along with other devices on the same chip such as optical phased arrays and tunable ring filters. Threshold power of $P_{th} = 89$ mW and slope efficiency $\eta = 1.0\%$ are obtained. We also measure the linewidth of the laser (figure 5-9), and obtain similar performance to the laser without the erbium trench. A slightly higher threshold power indicates additional intrinsic loss in the cavity which we have not investigated further. Potential source of loss can be due to the boundary loss of the trench, multimode coupling to the "trench mode", shadowing effect from the trench in Al_2O_3:Er^{3+}deposition.

In summary, we demonstrate the feasibility of integrating Al_2O_3:Er^{3+}laser in the full silicon photonics platform. The erbium trench is fabricated with the same patterning lithography for laser waveguide. This integration approach requires no alignment effort and still allows the Al_2O_3:Er^{3+}deposition to be the last step in the process. Similar laser performance is obtained for laser with and without erbium trench with

a slight additional loss. Further investigation is needed to optimize the performance of the laser.

5.3 Summary

In this chapter, we addressed the implementation of Al_2O_3:Er^{3+}laser in several use cases. For optical communication applications, we produced a multi-channels WDM light sources by cascading four DFB lasers with constant increment in grating period. We obtained laser wavelengths centered at 1563.92 nm, 1570.20 nm, 1576.28 nm, and 1582.16 nm at an average power of 16.9 dBm per DFB. The WDM sources show good thermal stability with temperature dependent wavelength shift of 0.015 nm/C, an order of magnitude smaller than semiconductor laser. Furthermore, we show that the thermal characteristic of Al_2O_3:Er^{3+}laser matches with SiN_xring filter, demonstrating the feasibility of a temperature control free transceiver operation.

We also extended the compatibility of Al_2O_3:Er^{3+}laser to work with other on-chip devices by demonstrating the integration of the laser in a full silicon photonics platform. An erbium trench is fabricated with the same patterning lithography step as the laser waveguide. We demonstrate a quarter phase shift DFB laser on the same chip that contains other working photonics devices. This integration opens the possibility for further integration of Al_2O_3:Er^{3+}laser in a more complex silicon photonics circuits.

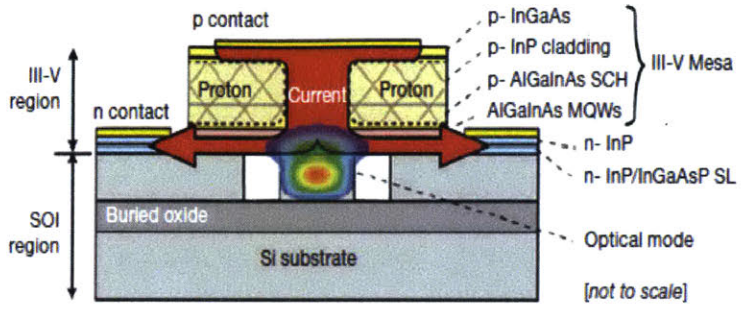

(a) Hybrid Bonding with InP

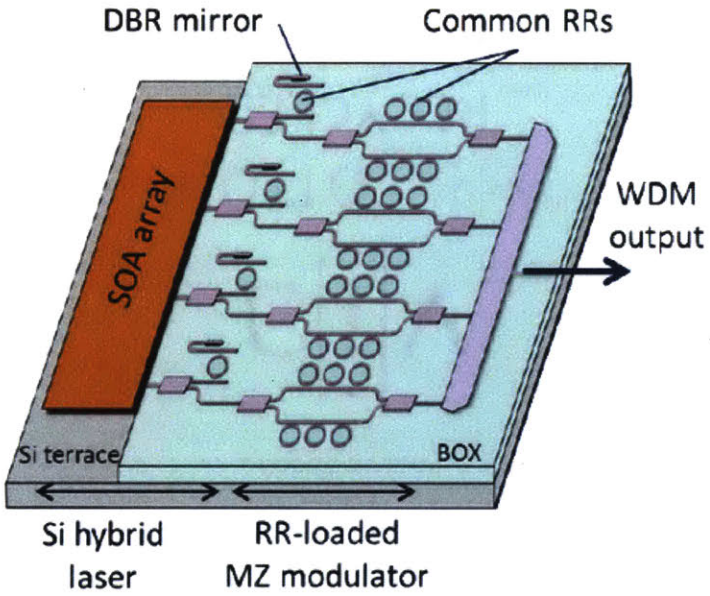

(b) External Cavity with SOA

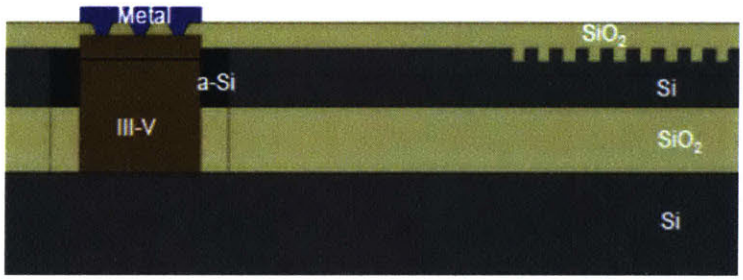

(c) SiO_2Buried Approach

Figure 5-6: Various integration schemes of semiconductor laser on silicon photonics platform. (a) Bonding of III-V laser and SiO_2glass by using Indium Phosphate (InP) material. (b) Bonding and alignment of semiconductor optical amplifier (SOA) on silicon substrate. (c) Burying of III-V material sealed by SiO_2layer with metal bonding on top.

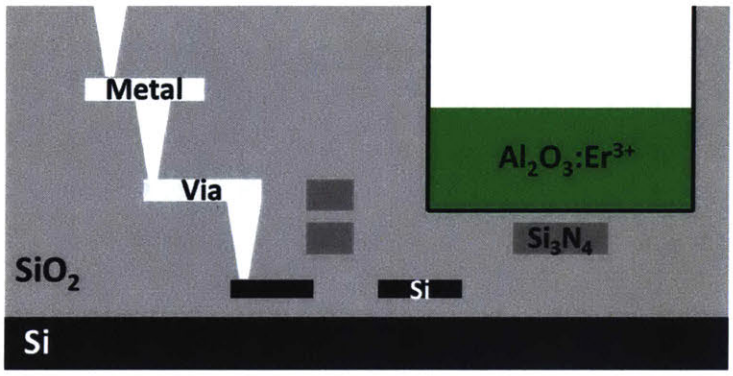

(a) Full Platform Integration

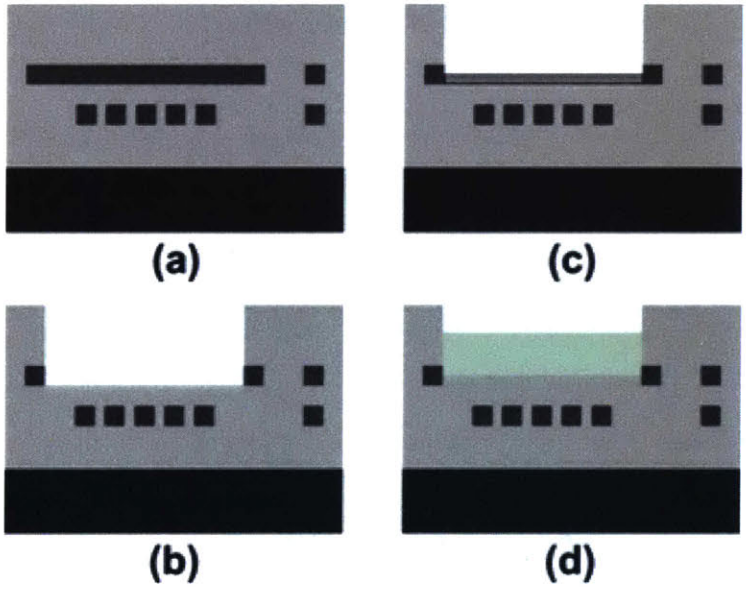

(b) Erbium Trench Process

Figure 5-7: (a) Schematic of integration scheme of $Al_2O_3:Er^{3+}$laser on full silicon photonics platform. (b) The fabrication process of $Al_2O_3:Er^{3+}$laser in erbium trench.

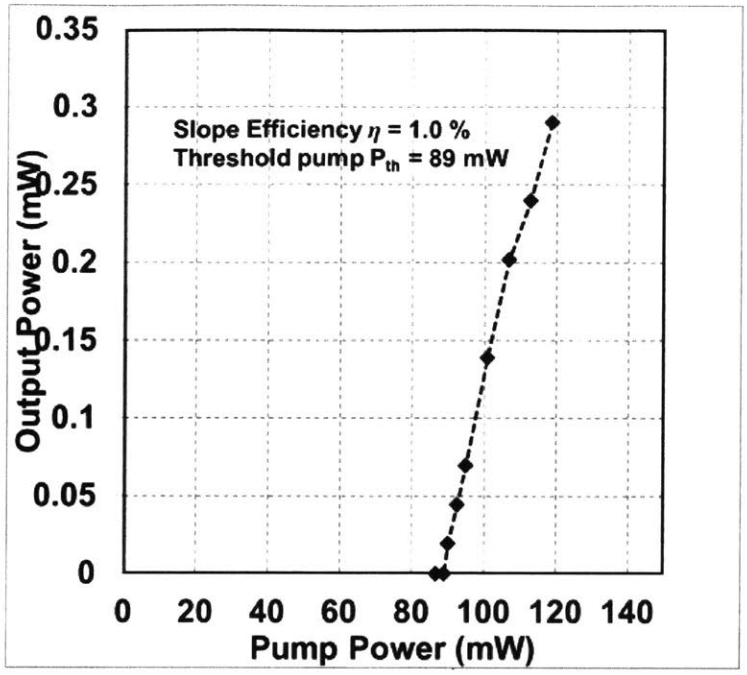

(a) Laser Performance

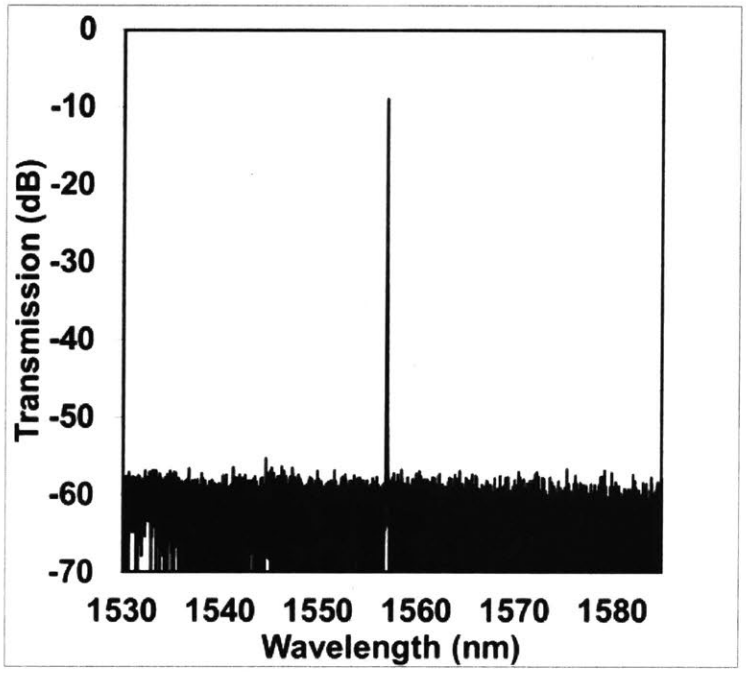

(b) Laser Spectrum

Figure 5-8: (a) Output power vs pump power and (b) spectrum of Al_2O_3:Er^{3+}laser in full silicon photonics platform.

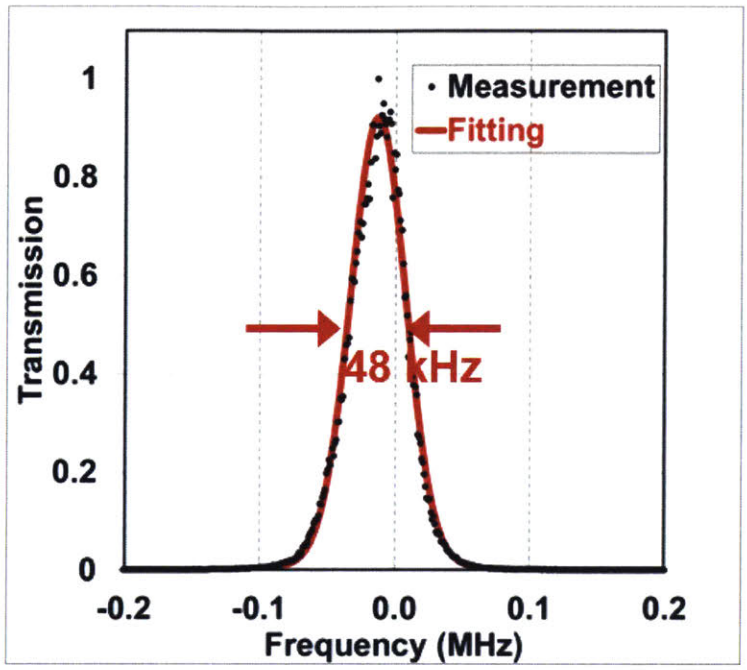

(a) Laser Linewidth (linear)

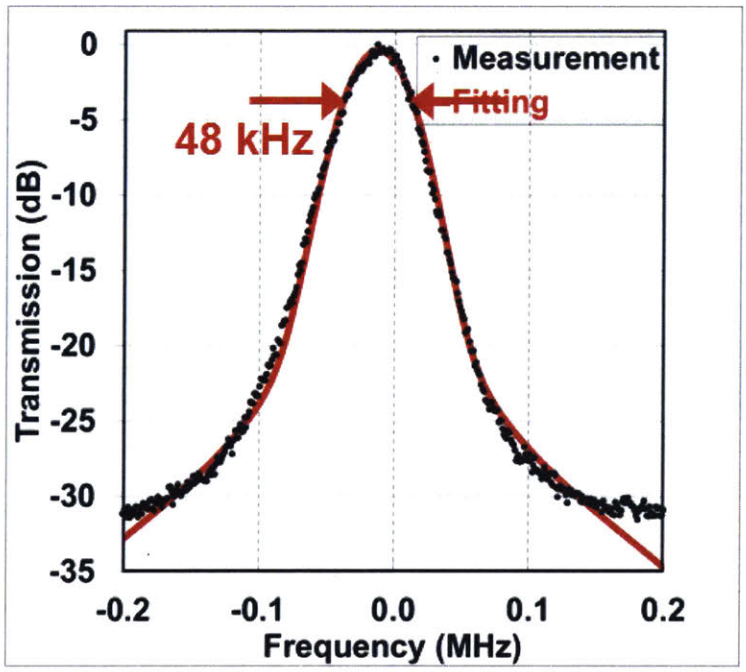

(b) Laser Linewidth (dB)

Figure 5-9: Laser linewidth in (a) linear and (b) dB scale.

Chapter 6

Additional Works

In this chapter, we discuss several additional works related to the main effort in this thesis. There are two main results discussed here, first, the microring laser design that uses the same novel waveguide design on a small trench area to generate a compact low threshold rare earth doped lasers. Then, we report a multi-pass pump configuration that enhances the absorption efficiency by tuning the grating design for the pump and lasing wavelength, .

6.1 Compact microring laser

We have demonstrated a high power Al_2O_3:Er^{3+}laser on silicon photonics platform. The cavity length is usually in centimeter-scale and the threshold power ranges in several to tens of miliwatts. In some applications such as biophotonic sensors [51, 52], compact device foot print and sub-milliwatt threshold might be preferred. In an approach which drastically reduces the device size and lasing threshold, high quality factor whispering gallery mode cavities [53, 54] have been doped with rare earth ions to realize visible and infrared microtoroid and microdisk lasers on silicon [52, 55, 56, 57]. However, such lasers are isolated on the chip surface and require an external fiber to couple pump and laser light to and from the cavity, respectively. Whereas efforts have been made towards a monolithic micrometer-scale integration scheme [58, 59, 60, 61], that is, where both microcavity and waveguide are co-integrated on the same chip,

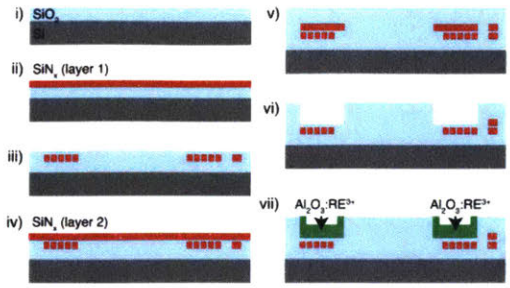

(a) Microring Fabrication Steps

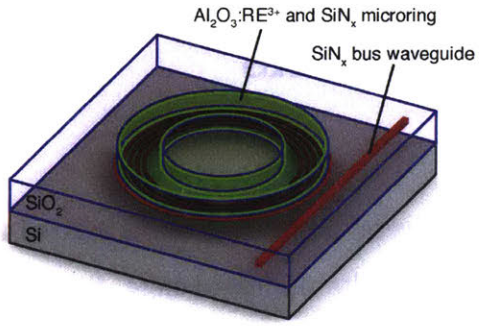

(b) Microring Structure

Figure 6-1: (a) Microring laser fabrication steps: (i) deposition of the SiO_2bottom-cladding layer on a silicon substrate; (ii) deposition of the lower SiN_xlayer; (iii) patterning of the SiN_xrings and bottom part of SiN_xbus waveguide (at far right) followed by SiO_2encapsulation; (iv) deposition of the upper SiN_xlayer; (v) patterning and SiO_2encapsulation of the upper SiN_xlayer to define the trench etch stop and top part of the nitride bus waveguide; (vi) microring trench etch and removal of SiN_xetch stop; (vii) deposition of the rare earth doped Al_2O_3gain medium into the trench. (b) Illustration of the resulting monolithic rare-earth-doped microring laser structure.

to our knowledge, no laser action has previously been demonstrated.

Here, using a similar laser waveguide design for Al_2O_3:Er^{3+}, we report on compact, low-threshold microring lasers monolithically integrated on silicon chips. The rare earth doped microlasers are fully integrated with their excitation and emission bus waveguides via a high-Q cavity design with effective fabrication technique. We show compact sub-milliwatt threshold microring lasers with erbium-, ytterbium, and thulium-doped Al_2O_3host material with center wavelengths at 1560 nm, 1040 nm, 1800 nm respectively. Our approach allows for straightforward, dense integration of such laser sources within existing silicon-based microphotonic systems.

We discussed the design of erbium- and ytterbium doped microring laser as follows.

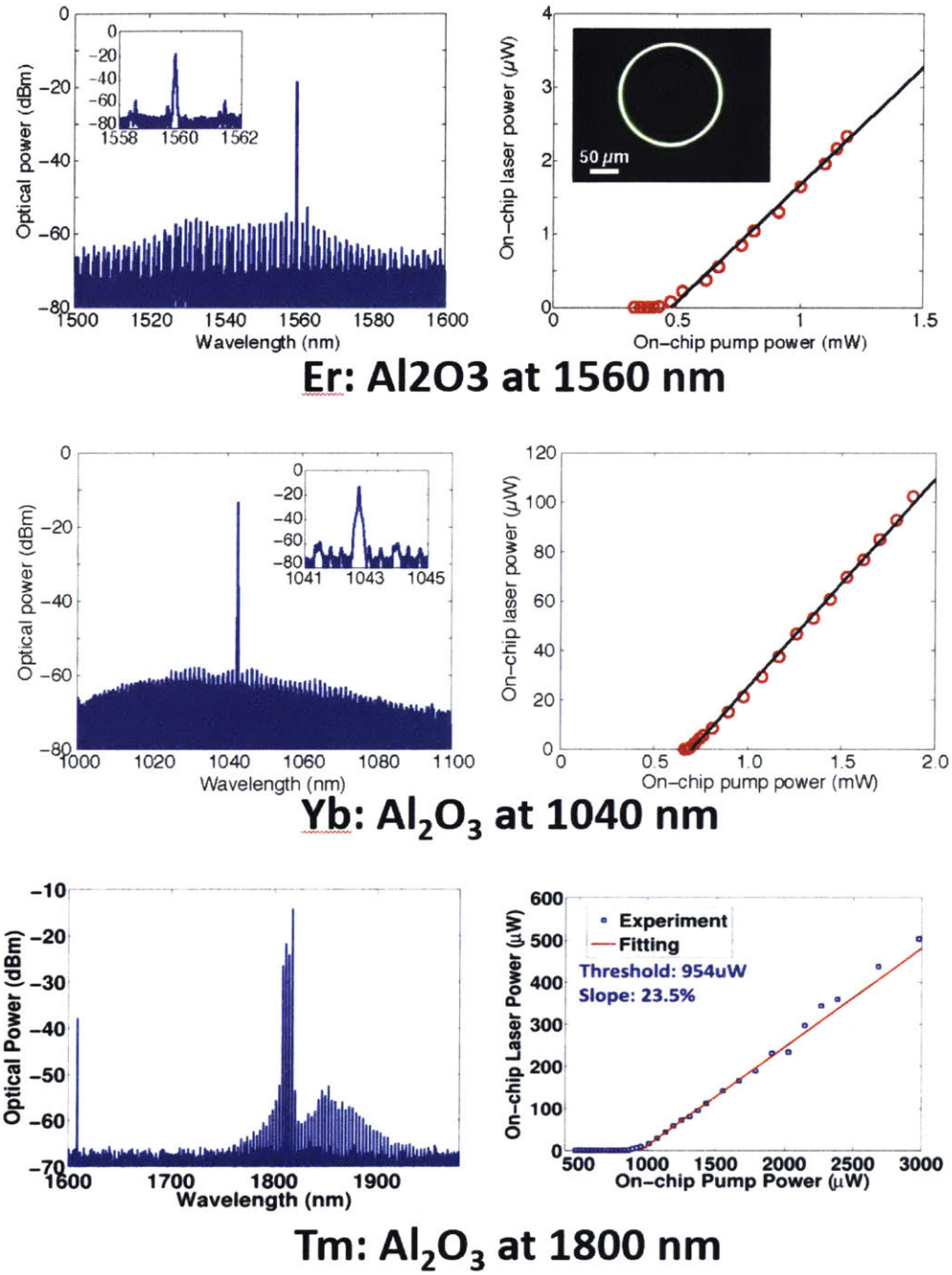

Figure 6-2: Laser performance and spectrum of various rare-earth doped Al_2O_3laser.

As shown in figure 6-1, our microring laser design is based on a silicon-compatible process flow which uses two SiN_xlayers. The microlaser structure consists of a rare earth doped Al_2O_3filled trench above SiN_xwaveguide, which forms the active micro-

cavity, beside a SiN_xbus waveguide for pump injection and laser output coupling. SiN_xhas a higher refractive index than rare earth doped Al_2O_3($n \sim 2$ vs. $n \sim 1.65$), enabling more compact, high-refractive-index-contrast and low-loss passive photonic devices. However, to achieve net gain in the cavity and lasing, a sufficient proportion of light must propagate in the active gain medium. Thus, we developed a composite resonator structure which supports modes with high optical intensity overlap with the gain layer, but also permits reduced microring diameter due to the SiN_xfeatures. The trench also serves to confine the light and reduce the microring bending radius and enables silicon compatibility (the non-standard gain material can be deposited into the trenches outside of the silicon foundry). The segmented SiN_xcavity design yields a highly wavelength-insensitive mode shape, allowing for high overlap between 980-nm pump modes and 1050-nm Yb- or 1550-nm Er-doped microring laser modes. Meanwhile, the integrated double-layer silicon nitride bus waveguide allows for a high degree of control of waveguide mode properties (i.e. for phase-matching to the microcavity pump modes and effective coupling of pump light to the ring) and low-loss guiding of pump and laser light on the chip.

We fabricated two 240 nm thick SiN_x(n = 1.94 at 1550 nm) layers with a 100-nm-thick SiO_2layer in between. We patterned both SiN_xlayers yielding 0.6 μm wide SiN_xmicroring features with 0.4 μm separations and 160 μm outer diameter, waveguide widths, w, of 0.4 or 0.9 μm and microring-waveguide gaps, g, ranging from 0.1 to 1.0 μm (in 0.1 μm steps). Above the top SiN_xlevel, we deposited a 4 μm thick SiO_2layer, and patterned and etched 4 μm deep microring trenches using the upper SiN_xlayer as an etch stop. After removal of the SiN_xetch-stop, we deposited an additional 100 nm thick SiO_2layer in the microring trenches. Lastly, we deposited 2 μm thick undoped, erbium-doped and ytterbium-doped aluminum oxide films over the top of the dies (shown only deposited into the microring trenches in the figure for clarity) using a reactive co-sputtering process as before. For the ytterbium-doped lasers we applied a uniform doping profile and concentration of 7×10^{20} cm^{-3}. We selected a relatively high ytterbium doping concentration because of the low absorption-to-emission cross-section ratio around 1050 nm and negligible concentration-quenching

effects observed in ytterbium doped Al_2O_3[32]. Moreover, relatively high gain was required to overcome the higher internal resonator scattering losses near 1 μm and output coupling as compared to erbium-doped devices operating near 1.5 μm. For erbium-doped lasers, the erbium concentration was varied throughout the layer in order to match the 980 nm pump mode distribution and minimize the laser threshold. We varied the sputtering power applied to the erbium target throughout the deposition, resulting in uniform lateral doping and a graded vertical concentration profile (with peak in the center of the film and approximately 1/3 the peak concentration at the top and bottom of the film). We selected peak erbium concentrations on the order of 2 to 3 $\times$ 10^{20} cm^{-3} high enough to achieve higher gain than cavity losses, but low enough to maintain low threshold lasing and avoid significant concentration quenching mechanisms [13]. We summarize the fabrication steps in figure 6-1a and the resulting structure is illustrated in figure 6-1b.

In figure 6-2 we show the laser performance of erbium- and ytterbium- doped Al_2O_3laser. For erbium laser, by varying the gap of the bus waveguide and the trench structure, we observed laser modes spanning a wavelength range of 1530 $-$ 1565 nm and both multi-mode and single-mode lasing. The laser spectrum was typically multi-mode at low pump powers, while one or two dominant modes emerged under higher powers. For a device with erbium concentration 3 $\times$ 10^{20} cm^{-3} and g = 0.3 μm we observed single-mode lasing at 1560 nm (with side-mode suppression $>$ 30 dB) and up to 27 μW total laser power in the silicon nitride waveguide (limited by the maximum diode laser pump power). By comparing to the resonances observed in 1550 nm transmission measurements in the same chips, we determined the laser modes to be TM like. The free-space 3dB linewidth was $<$ 20 pm (below the limit of the optical spectrum analyzer used to measure the laser spectrum). We obtained the lowest laser threshold in devices with g $\sim$ 0.5 μm (at optimum pump coupling) and at reduced erbium concentration. The laser exhibits a threshold of 0.5 mW, and double-sided slope efficiency of 0.3%, with up to 2.4 μW output power (total power measured from both outputs) coupled into the SiN_xwaveguide.

In ytterbium-doped microrings we observed lasing in the range 1020 $-$ 1045 nm.

We observed lowest-threshold lasing at a pump wavelength of 970.96 nm. This wavelength is blue-shifted from Yb absorption peak around 975 nm because the absorption at 975 nm is too strong, thus significantly reducing both Q and the coupled pump power. A single laser line is evident at 1040 nm with a side-mode suppression of $>$ 40 dB (inset). We observed lasing at a threshold of 0.7 mW, a total output power of $>$ 100 μW coupled into the SiN_xwaveguide and double-sided slope efficiency of 8.4%.

The fabrication and characterization of thulium doped microring lasers are similar to erbium and ytterbium microlasers. We will refer the reader to the PhD thesis of Zhan Su [62].

With these results we have realized highly-compact monolithic rare-earth-doped devices on silicon. Previously, the smallest bend radius obtained in an Al_2O_3:Er^{3+}device embedded in $SiO_2$was 250 μm, in that case a compact amplifier [63]. Here, using SiN_xfeatures we reduce the bend radius to 80 m, thus suggesting a path towards more compact integrated amplifiers as well as lasers. Compared to previous Al_2O_3:Er^{3+}racetrack lasers [16], we have decreased the device footprint by a factor of $\sim$500. Meanwhile, the total cavity length of the microrings is 20 times shorter than that of DFB and DBR devices, and the thresholds reported here are more than 10 times smaller.

While in this work we demonstrate a proof of principle, a full investigation of the parameter space can lead to enhanced microring laser performance. Er-Yb co-doping or in-band pumping at 1480 nm can be explored to increase the erbium laser efficiency. Furthermore, the high efficiencies of DFB and DBR lasers and ultra-low thresholds demonstrated in fiber-coupled microcavities [52, 55, 56, 57] indicate that higher efficiencies and lower thresholds can be obtained by optimizing the resonator mode and optical coupling properties and increasing the cavity Q.

By using standard silicon wafer-scale processing, we demonstrate that these microring lasers can be implemented in silicon-based photonic circuits (i.e. enabling integration with high-performance active and passive silicon, germanium and silicon nitride devices). A single off-chip fiber-coupled pump source or heterogeneously-bonded on-chip laser diode pump could efficiently power multiple microring lasers.

Due to their low threshold and single-mode operation around 1.5 μm, arrays of Er-doped lasers are promising as chip-scale multi-wavelengths communications sources. Meanwhile, Yb-doped lasers emit in the low water absorption window, can operate in water and can act as highly effective nanoparticle sensors [64, 65]. Thus, their implementation in lab-on-a-chip or integrated biophotonic applications is of interest. Furthermore, the reported cavity structure can easily be adapted for additional rare earth dopants (Nd^{3+}, Tm^{3+}, etc.) with different pump and laser wavelengths.

In summary, we have shown lasing in fully-integrated, monolithic microring structures on silicon chips. The rare-earth-doped microring lasers are enabled by a multilayer design which is silicon-compatible, straightforward and can be easily adapted to realize laser sources emitting from the visible to mid-infrared wavelengths on a full silicon photonics process flow. The low lasing threshold suggests that a single, low-cost diode laser pump source could excite densely-integrated arrays of lasers on a chip for wavelength division multiplexing applications. Optimization of optical coupling parameters and microring mode properties can lead to even lower thresholds, higher efficiencies and smaller device footprints. These new, compact, inexpensive and efficient lasers are a viable alternative to existing silicon-based laser technologies and have implications for wide-ranging applications of integrated photonic systems, including optical computing, classical and quantum communications, sensing, biophotonics and fundamental micro- and nanoscale research.

6.2 Resonantly Pumped DFB Laser

In a typical Al_2O_3:Er^{3+}laser, the pump absorption is usually limited, particularly because of their small footprint size as compared to traditional erbium fiber laser. To allow sufficiently short pump absorption lengths, erbium-doped waveguide lasers are doped with higher levels of erbium concentrations, which can lead to increase in energy transfer upconversions and concentration-quenching effects [66]. Recirculating the pump can increase the number of pump passes over a short length. For instance, a highly reflective mirror can be placed at the end of an erbium-doped waveguide laser

and reflect the unabsorbed pump back into the laser, as suggested in reference [47]. We demonstrated this scheme in the experiment, as shown in figure 6-3, and shows ~1.5 times improvement in threshold power and slope efficiency. This permits two pump passes but prevents dual-sided pumping, from the side of the highly reflective mirror. To allow multiple pump passes, an additional reflective mirror can be placed at the laser input, forming a pump cavity.

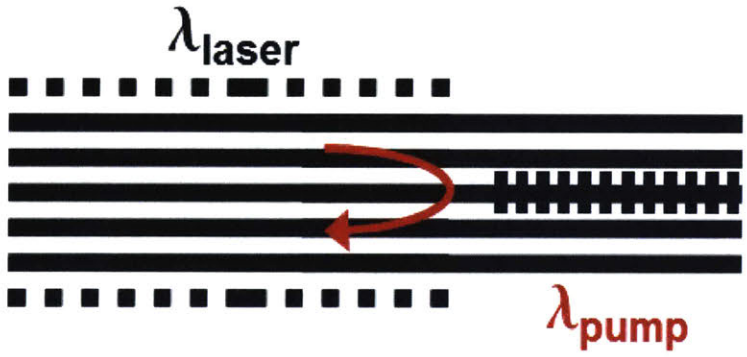

(a) Single Reflector Design

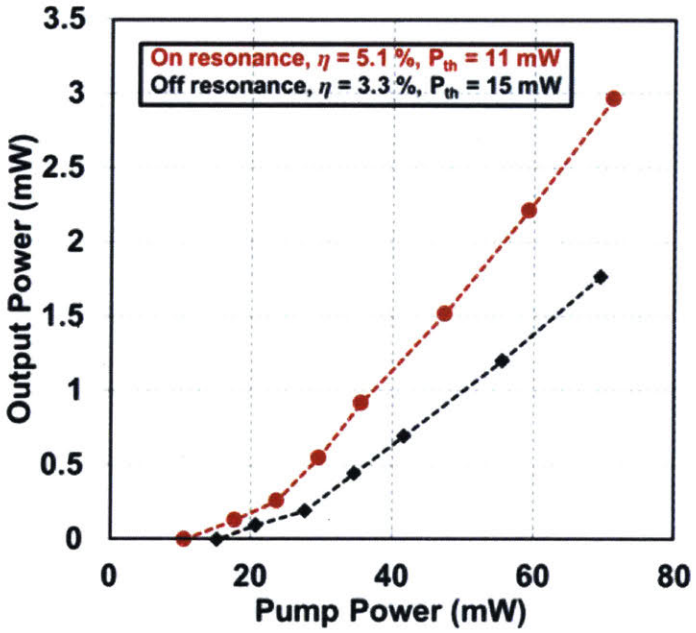

(b) Single Reflector Performance (dB)

Figure 6-3: (a) Schematic and (b) laser performance of DFB laser with a single pump reflector.

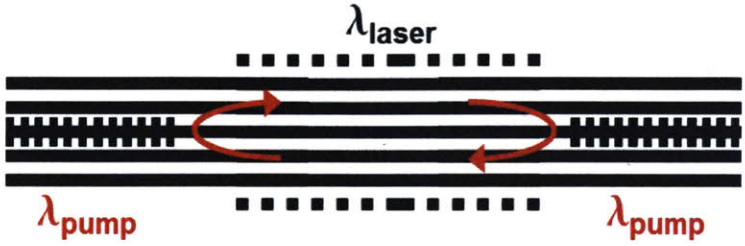

(a) Resonant Pump Design

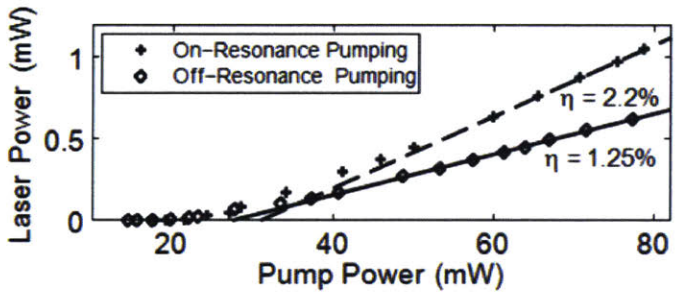

(b) Resonant Pump Performance (dB)

Figure 6-4: (a) Schematic and (b) laser performance of DFB laser with resonant pumping.

Here, we report on an optical pumping scheme, termed resonant pumping, for an Al_2O_3:Er^{3+}DFB waveguide laser. The scheme uses two mirrors on either side of the DFB laser, forming a pump cavity that recirculates the unabsorbed pump light. Symmetric distributed Bragg reflectors are used as the mirrors and are designed by matching the external and internal quality factors of the cavity. Experimental demonstration shows lasing at an optical communication wavelength of around 1560 nm and an improvement of 1.8 times in the lasing efficiency, when the DFB laser is pumped on-resonance.

We briefly discuss the resonant pumped DFB laser here, for full discussion, readers are encouraged to refer to [67]. The structure is the standard quarter phase shifted DFB laser enclosed by a DBR pump cavity. The DBR pump cavity is realized by placing DBR gratings on either side of the DFB laser. The grating perturbations have a period of 0.298 μm and are formed by etching out 0.1 μm from both sides of the center SiN_xlayer. The center SiN_xhas a width w_c of 0.458 μm. The lengths of the

DBR grating and DFB laser are 350 μm and 2 cm, respectively. A small separation exists between the ends of the DFB laser and the DBR gratings, and, hence, the total length of the DBR pump cavity is 2.11 cm. A layer of index-matching fluid (n=1.45) is placed on top of the laser during measurement to assist in matching the pump resonance.

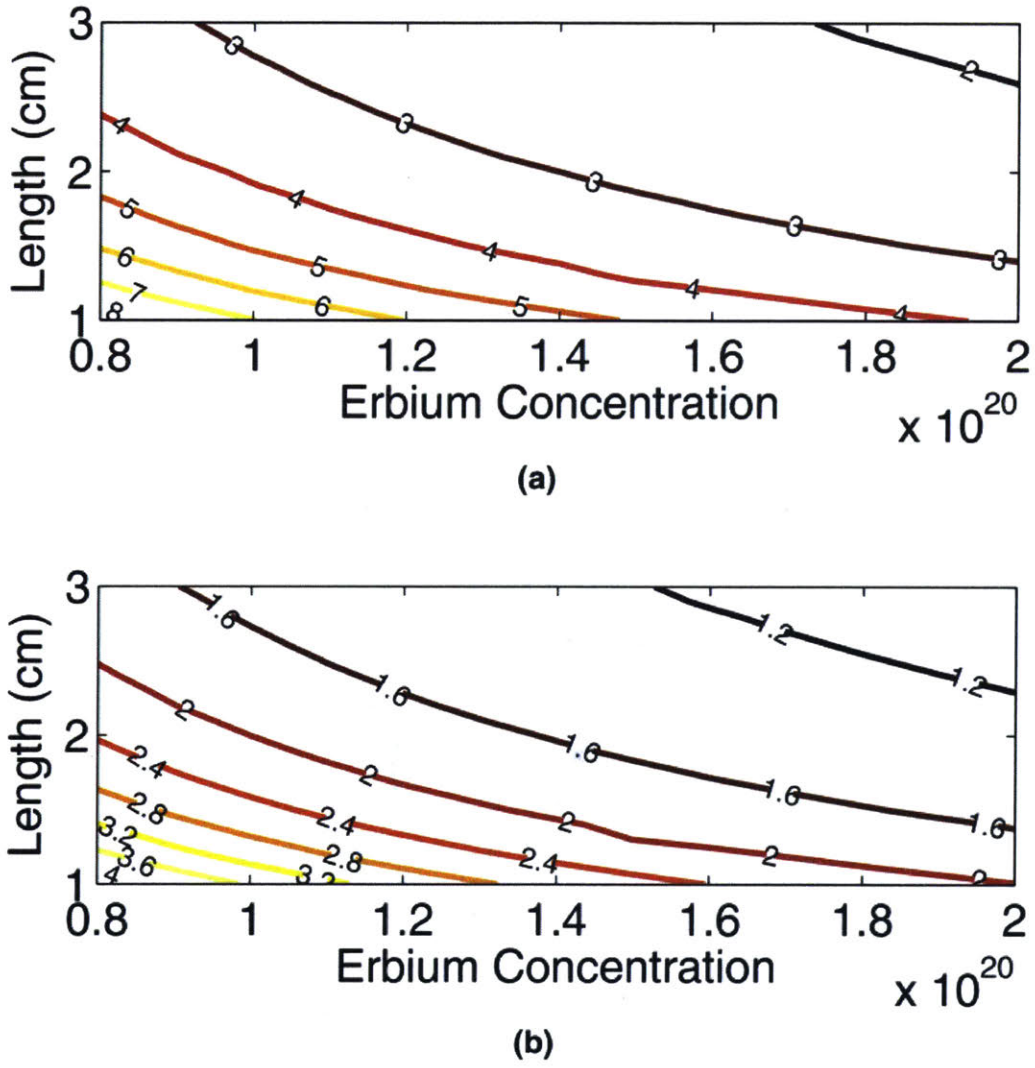

Figure 6-5: Contour plot of the cavity-induced field enhancement for different cavity lengths and erbium concentrations (ions/cm^3): (a) maximum enhancement, (b) average enhancement.

The pump cavity DBR grating design was based on matching the grating external quality factor Q_{ext} to the internal Q_{int} of the pump cavity, for critical coupling [68]. The internal Q_{int} consists of total pump loss that comes from background loss in the

Al_2O_3:Er^{3+}film and the erbium absorption loss. The background loss was measured to be 0.1 dB/cm and erbium absorption at 976 nm was calculated to be 0.91 dB/cm from the doping concentration of 1.5×10^{20} cm^{-3} with the pump confinement factor of 0.76. The total pump loss is thus 1.0 dB/cm. Using the total pump loss value and the effective index of 1.64 at 976 nm, the internal Q_{int} can be calculated to be 4.5×10^5. The grating external Q_{ext} can be calculated by assuming Fabry Perot cavity. Following the grating design, transfer matrix calculations were performed to determine the amount of field enhancement produced by the cavity, at resonance. The amount of enhancement was calculated as the ratio between the field intensity in the cavity and the intensity in a single-pass case. This can be expressed at various points along the cavity as the following:

$$\zeta(z) = \frac{\mid E_f(z) + E_r(z) \mid^2}{\mid E_{fs}(z) \mid^2} \tag{6.1}$$

$E_f(z)$ and $E_r(z)$ are the forward and backward propagating electric fields along the cavity, respectively, and $E_{fs}(z)$ is just the forward electric field in the single-pass case. A standing wave is formed in the cavity, with periodic maximum and minimum electric-field fluctuations. Figure 6-5 shows a contour plot of the maximum and average field enhancements for various cavity lengths and erbium doping concentrations. The maximum value was taken at the center of the cavity, where much of the DFB laser intensity exists. Note that these calculations assumed -matched grating reflectivities. It can be easily deduced that the enhancement increases as the cavity length shortens or the erbium concentration reduces. For a cavity length of 2.11 cm and an erbium doping concentration of 1.5×10^{20} cm^{-3}, the average and maximum field intensity enhancements are 1.5 and 2.7, respectively. We hence expect laser performance improvements, within this range, when pumped on-resonance.

To pump the laser, we use a narrow-linewidth 976 nm pump diode (< 1 MHz) laser. The output is collected from the 1550 nm outputs of both the right and left WDMs, and measured using an optical spectrum analyzer. By insertion loss measurements, we

estimate coupling losses per facet of 4.2 and 5.7 dB for 976 and 1550 nm, respectively, without the index-matching fluid on the chip. The coupling losses are 3.3 and 4.5 dB for 976 and 1550 nm, respectively, with the index-matching fluid. Lasing is observed at 1563 nm. Figure 6-4b shows the on-chip laser power versus the on-chip pump power for cases when the laser is pumped on- and off-resonance. From the plot, the slope efficiencies can be estimated to be 2.2% and 1.2% with on- and off-resonance pumping, respectively. An improvement of 1.8 times is thus achieved when the laser is pumped on-resonance. This improvement falls within the predicted enhancement ranges of 1.5 and 2.7, as discussed above.

In summary, we have demonstrated resonant pumping for an erbium-doped DFB laser. A pump cavity was formed by placing DBR gratings on either side of the DFB laser. The design of the DBR gratings was based on matching the internal and external Qs. Experimental measurement show an improvement of 1.8 times in the lasing efficiency when the DFB laser was pumped on-resonance. The proposed resonant pumping scheme improve the pump absorption rate for short laser cavities.

Chapter 7

Summary

Silicon photonics is the future of optical technology. By leveraging the maturity of silicon device fabrication, the field of photonics has found its way to the large scale production potential. Just as electronics need a voltage source, a complete silicon photonics platform requires a coherent light source such as laser. The top three specifications of silicon photonics laser are CMOS compatibility, high power scalability and ultra-narrow linewidth for low noise operation.

We present the development of integrated erbium-doped aluminum oxide laser on a silicon photonics platform. Using a novel wavelength-insensitive design, a CMOS compatible waveguide structure is designed to achieve high confinement factor and intensity overlap for both the pump (980 nm) and signal (1550 nm) wavelengths. Laser operation in the C- and L- bands of the erbium gain spectrum is obtained with both a distributed Bragg reflector and a distributed feedback structure. We demonstrate power scaling with output power greater than 75 mW. To obtain an ultra-narrow linewidth laser, we design a distributed phase shift laser to obtain 5.3 $\pm$ 0.3 kHz linewidth. A recirculating-self heterodyne delayed interferometer setup is used to measure the linewidth accurately.

We then continue to investigate the influence of gain film thickness uniformity in distributed feedback laser performance. Due to the geometry mismatch of the circularly symmetric deposition process and the straight laser structure, we observed performance degradation and inconsistency across the 300 mm wafer in a 2-cm DFB

cavity. We propose a compensation scheme by bending the DFB structure to follow the circular symmetry of the fabrication step. We obtain performance improvement of greater than 6 times in the threshold power. The curved DFB laser is shown to be more tolerant to misalignment in the deposition, and thus providing a reliable approach for obtaining on-chip Al_2O_3:Er^{3+}laser.

We consider the implementation of Al_2O_3:Er^{3+}laser in several use cases. In optical communication application, a wavelength division multiplexed (WDM) light source for silicon photonics can be obtained by cascading several Al_2O_3:Er^{3+}DFB lasers. We obtain a well-spaced four channels lasers with a temperature stable operation across $20 - 50^{o}$C. Furthermore, we extend the compatibility of Al_2O_3:Er^{3+}laser to work with other on-chip devices by demonstrating the integration of laser in a full silicon photonics platform. An erbium trench is fabricated on the location of the laser allowing alignment free process. This integration opens the possibility for further integration of Al_2O_3:Er^{3+}laser in a more complex silicon photonics circuits.

We discuss several additional related works. First, compact low threshold laser design by using a microring laser structure in an erbium trench. Lastly, a resonant pumped DFB structure that improved the pump absorption rate by almost two times.

An immediate potential future work is to combine Al_2O_3:Er^{3+}laser with other existing photonics devices on the same chips such as transceiver link, phased array, and sensor applications. Other possible directions include investigating other rare-earth doping at longer wavelength such as thulium and holmium doped lasers at 1.9 μm where the silicon absorption is lower. The laser design can also be further optimized by investigating different doping concentrations, cavity lengths, and other cavity parameters. Finally, the author hopes the work presented in this thesis can serve as a building block to a more complex applications of Al_2O_3:Er^{3+}laser in the future.

Appendix A

Three-level Erbium model

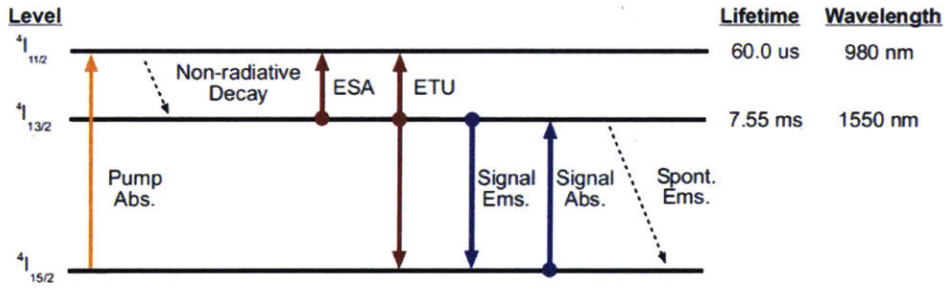

Figure A-1: Three-level state energy of Al_2O_3:Er^{3+}laser.

Fig. A-1 presents a 3 level model of erbium. ${}^4I_{15/2}$, ${}^4I_{13/2}$ and ${}^4I_{11/2}$ represent the ground, signal and pump energy states, respectively. Pump absorption occurs from ${}^4I_{15/2}$ to ${}^4I_{11/2}$. Fast non-radiative decay transition occurs to ${}^4I_{13/2}$. Excited state absorption (ESA) and/or energy transfer up-conversions (ETU) occurs from ${}^4I_{13/2}$ to ${}^4I_{11/2}$. Signal emission and absorption occurs between ${}^4I_{13/2}$ and ${}^4I_{15/2}$.

The temporal dynamics of signal photon and the 3 energy states can be expressed

as the following rate equations

$$\frac{dN_2}{dt} = -\frac{1}{\tau_2}N_2 + \frac{\sigma_{p,a}\lambda_p P_{in}}{chA_{eff}}N_0 + \frac{\sigma_{s,esa}\lambda_s}{chA_{eff}}SN_1 + W_{s,etu}{N_1}^2 \tag{A.1}$$

$$\frac{dN_1}{dt} = \frac{1}{\tau_2}N_2 + \frac{\sigma_{s,a}\lambda_s}{chA_{eff}}SN_0 - \frac{\sigma_{s,e}\lambda_s}{chA_{eff}}SN_1 - \frac{1}{\tau_1}N_1 - \frac{\sigma_{s,esa}\lambda_s}{chA_{eff}}SN_1 \tag{A.2}$$

$$- 2W_{s,etu}{N_1}^2 \tag{A.3}$$

$$N_0 = N_t - N_1 - N_2 \tag{A.4}$$

$$\frac{dS}{dt} = -v_g(\alpha + \sigma_{s,e}N_1 - \sigma_{s,a}N_0 - \sigma_{s,esa}N_1)S. \tag{A.5}$$

N_0, N_1, N_2 are the erbium concentrations at ground, signal and pump energy states, respectively. $\sigma_{p,a}$, $\sigma_{s,a}$, $\sigma_{s,e}$ are the pump absorption cross-section, signal absorption and emission cross-sections, respectively. $\sigma_{s,esa}$ is the signal-to-pump excited-state cross-section (ESA) and $W_{s,etu}$ is the signal-to-pump energy transfer up-conversion coefficient (ETU). In general, there may be a pump-to-higher-state ESA and ETU. But we consider a simplified model here. P_{in} is the input pump power (watts). λ_p and λ_s are the pump and signal wavelengths. α is the total cavity loss $(1/m)$ and v_g is the group velocity. A_{eff} is the effective area and S is the photon power (watts).

Dynamic solutions can be attained by simply applying a finite-difference scheme to the above equations. For example a forward-difference scheme can be expressed as

$$N_2^n = \Delta_t(-\frac{1}{\tau_2}N_2^{n-1} + \frac{\sigma_{p,a}\lambda_p P_{in}}{chA_{eff}}N_0^{n-1} + \frac{\sigma_{s,esa}\lambda_s}{chA_{eff}}S^{n-1}N_1^{n-1} \tag{A.6}$$

$$+ W_{s,etu}{N_1^{n-1}}^2) + N_2^{n-1} \tag{A.7}$$

$$N_1^n = \Delta_t(\frac{1}{\tau_2}N_2^{n-1} + \frac{\sigma_{s,a}\lambda_s}{chA_{eff}}S^{n-1}N_0^{n-1} - \frac{\sigma_{s,e}\lambda_s}{chA_{eff}}S^{n-1}N_1^{n-1} - \frac{1}{\tau_1}N_1^{n-1} \tag{A.8}$$

$$- \frac{\sigma_{s,esa}\lambda_s}{chA_{eff}}S^{n-1}N_1^{n-1} - 2W_{s,etu}{N_1^{n-1}}^2) + N_1^{n-1} \tag{A.9}$$

$$N_0^n = N_t - N_1^n - N_2^n \tag{A.10}$$

$$S^n = \Delta_t(-v_g(\alpha + \sigma_{s,e}N_1^{n-1} - \sigma_{s,a}N_0^{n-1})S^{n-1}) + S^{n-1}. \tag{A.11}$$

Higher-order difference schemes may be used, for example, Runge-Kutta 4th order, for better accuracy or larger time-step size (shorter computation time).

Steady-state solutions can be attained by setting the differential operators to zero and solving the set of 4 equations for 4 unknowns.

$$0 = -\frac{1}{\tau_2}N_2^{ss} + \frac{\sigma_{p,a}\lambda_p P_{in}}{chA_{eff}}N_0^{ss} + \frac{\sigma_{s,esa}\lambda_s}{chA_{eff}}S^{ss}N_1^{ss} + W_{s,etu}N_1^{ss2} \tag{A.12}$$

$$0 = \frac{1}{\tau_2}N_2^{ss} + \frac{\sigma_{s,a}\lambda_s}{chA_{eff}}S^{ss}N_0^{ss} - \frac{\sigma_{s,e}\lambda_s}{chA_{eff}}S^{ss}N_1^{ss} - \frac{1}{\tau_1}N_1^{ss} \tag{A.13}$$

$$- \frac{\sigma_{s,esa}\lambda_s}{chA_{eff}}S^{ss}N_1^{ss} - 2W_{s,etu}N_1^{ss2} \tag{A.14}$$

$$N_0^{ss} = N_t - N_1^{ss} - N_2^{ss} \tag{A.15}$$

$$0 = v_g(\alpha + \sigma_{s,e}N_1^{ss} - \sigma_{s,a}N_0^{ss})S^{ss}. \tag{A.16}$$

One can simply use in-built Matlab solvers, such as fsolve, to solve the 4 unknowns.

Ion-quenching in erbium doped lasers can affect the stability. An additional set of equations (noted with subscript q) for quenched-ions can be added to the original set of equations (A.1)-(A.5) for active-ions (noted with subscript a) and written as a set of coupled equations as

$$\frac{dN_{2,a}}{dt} = -\frac{1}{\tau_2}N_{2,a} + \frac{\sigma_{p,a}\lambda_p P_{in}}{chA_{eff}}N_{0,a} + \frac{\sigma_{s,esa}\lambda_s}{chA_{eff}}SN_{1,a} + W_{s,etu}{N_{1,a}}^2 \tag{A.17}$$

$$\frac{dN_{1,a}}{dt} = \frac{1}{\tau_2}N_{2,a} + \frac{\sigma_{s,a}\lambda_s}{chA_{eff}}SN_{0,a} - \frac{\sigma_{s,e}\lambda_s}{chA_{eff}}SN_{1,a} - \frac{1}{\tau_1}N_{1,a} - \frac{\sigma_{s,esa}\lambda_s}{chA_{eff}}SN_{1,a} \tag{A.18}$$

$$- 2W_{s,etu}{N_{1,a}}^2 \tag{A.19}$$

$$N_{0,a} = N_{t,a} - N_{1,a} - N_{2,a} \tag{A.20}$$

$$\frac{dN_{2,q}}{dt} = -\frac{1}{\tau_2}N_{2,q} + \frac{\sigma_{p,a}\lambda_p P_{in}}{chA_{eff}}N_{0,q} + \frac{\sigma_{s,esa}\lambda_s}{chA_{eff}}SN_{1,q} + W_{s,etu}{N_{1,q}}^2 \tag{A.21}$$

$$\frac{dN_{1,q}}{dt} = \frac{1}{\tau_2}N_{2,q} + \frac{\sigma_{s,a}\lambda_s}{chA_{eff}}SN_{0,q} - \frac{\sigma_{s,e}\lambda_s}{chA_{eff}}SN_{1,q} - \frac{1}{\tau_{1,q}}N_{1,q} - \frac{\sigma_{s,esa}\lambda_s}{chA_{eff}}SN_{1,q} \tag{A.22}$$

$$- 2W_{s,etu}{N_{1,q}}^2 \tag{A.23}$$

$$N_{0,q} = N_{t,q} - N_{1,q} - N_{2,q} \tag{A.24}$$

$$\frac{dS}{dt} = -v_g(\alpha + \sigma_{s,e}(N_{1,a} + N_{1,q}) - \sigma_{s,a}(N_{0,a} + N_{0,q}) - \sigma_{s,esa}(N_{1,a} + N_{1,q}))S. \tag{A.25}$$

The difference in the ion-quench set of equations is simply in the lifetime of the quench

ions ($\tau_{1,q}$ in equation (A.22)). Coupling here occurs through the photon number. Similar attempts as above can be made to solve for the transient and steady-state values.

A quick way to analyze the stability due to ion-quenching (compared to a temporal simulation), is to consider a small perturbation in steady-state and study whether the perturbation grows or decays. Let $\Delta N_{2,q}$, $\Delta N_{1,q}$, $\Delta N_{0,q}$ be the small perturbation in quench ion energy states. Similarly, let $\Delta N_{2,a}$, $\Delta N_{1,a}$, $\Delta N_{0,a}$ be the small perturbation in active ion energy states. And let ΔS be the small perturbation in photon. From (A.17)-(A.35), the perturbed system can be expressed as

$$\frac{d(N_{2,a}^{ss}+\Delta N_{2,a})}{dt} = -\frac{1}{\tau_2}(N_{2,a}^{ss}+\Delta N_{2,a}) + \frac{\sigma_{p,a}\lambda_p P_{in}}{chA_{eff}}(N_{0,a}^{ss}+\Delta N_{0,a}) \tag{A.26}$$

$$\frac{d(N_{1,a}^{ss}+\Delta N_{1,a})}{dt} = \frac{1}{\tau_2}(N_{2,a}^{ss}+\Delta N_{2,a}) + \frac{\sigma_{s,a}\lambda_s}{chA_{eff}}(S^{ss}+\Delta S)(N_{0,a}^{ss}+\Delta N_{0,a}) \tag{A.27}$$

$$- \frac{\sigma_{s,e}\lambda_s}{chA_{eff}}(S^{ss}+\Delta S)(N_{1,a}^{ss}+\Delta N_{1,a}) - \frac{1}{\tau_1}(N_{1,a}^{ss}+\Delta N_{1,a}) \tag{A.28}$$

$$N_{0,a}^{ss}+\Delta N_{0,a} = N_{t,a} - N_{1,a}^{ss} - \Delta N_{1,a} - N_{2,a}^{ss} - \Delta N_{2,a} \tag{A.29}$$

$$\frac{d(N_{2,q}^{ss}+\Delta N_{2,q})}{dt} = -\frac{1}{\tau_2}(N_{2,q}^{ss}+\Delta N_{2,q}) + \frac{\sigma_{p,a}\lambda_p P_{in}}{chA_{eff}}(N_{0,q}^{ss}+\Delta N_{0,q}) \tag{A.30}$$

$$\frac{d(N_{1,q}^{ss}+\Delta N_{1,q})}{dt} = \frac{1}{\tau_2}(N_{2,q}^{ss}+\Delta N_{2,q}) + \frac{\sigma_{s,a}\lambda_s}{chA_{eff}}(S^{ss}+\Delta S)(N_{0,q}^{ss}+\Delta N_{0,q}) \tag{A.31}$$

$$- \frac{\sigma_{s,e}\lambda_s}{chA_{eff}}(S^{ss}+\Delta S)(N_{1,q}^{ss}+\Delta N_{1,q}) - \frac{1}{\tau_{1,q}}(N_{1,q}^{ss}+\Delta N_{1,q}) \tag{A.32}$$

$$N_{0,q}^{ss}+\Delta N_{0,q} = N_{t,q} - N_{1,q}^{ss} - \Delta N_{1,q} - N_{2,q}^{ss} - \Delta N_{2,q} \tag{A.33}$$

$$\frac{d(S^{ss}+\Delta S)}{dt} = -v_g(\alpha + \sigma_{s,e}(N_{1,a}^{ss}+\Delta N_{1,a}+N_{1,q}^{ss}+\Delta N_{1,q}) \tag{A.34}$$

$$- \sigma_{s,a}(N_{0,a}^{ss}+\Delta N_{0,a}+N_{0,q}^{ss}+\Delta N_{0,q}))(S^{ss}+\Delta S). \tag{A.35}$$

For simplicity we do not include the ESA and ETU effects.

Assuming the perturbations are small enough such that higher-order terms can be canceled out (e.g $\Delta S \Delta N_{1,a} = 0$), the above set of equations can be reduced and

expressed in linear matrix form as

$$\frac{d}{dt}\begin{bmatrix} \Delta N_{2,a} \\ \Delta N_{1,a} \\ \Delta N_{2,q} \\ \Delta N_{1,q} \\ \Delta S \end{bmatrix} = \mathbf{M}\begin{bmatrix} \Delta N_{2,a} \\ \Delta N_{1,a} \\ \Delta N_{2,q} \\ \Delta N_{1,q} \\ \Delta S \end{bmatrix}, \tag{A.36}$$

where $\mathbf{M}$ is

$$\mathbf{M} = \begin{bmatrix} m_{11} & m_{12} & 0 & 0 & 0 \\ m_{21} & m_{22} & 0 & 0 & m_{25} \\ 0 & 0 & m_{33} & m_{34} & 0 \\ 0 & 0 & m_{43} & m_{44} & m_{45} \\ m_{51} & m_{52} & m_{53} & m_{54} & m_{55} \end{bmatrix}. \tag{A.37}$$

and

$$m_{11} = -\frac{1}{\tau 2} - \frac{\sigma_{p,a}\lambda_p P_{in}}{cchA_{eff}}$$
$$m_{12} = -\frac{\sigma_{p,a}\lambda_p P_{in}}{cchA_{eff}}$$
$$m_{21} = \frac{1}{\tau 2} - \frac{\sigma_{s,a}\lambda_s S^{ss}}{cchA_{eff}}$$
$$m_{22} = -\frac{\sigma_{s,a}\lambda_s S^{ss}}{cchA_{eff}} - \frac{\sigma_{s,e}\lambda_s S^{ss}}{cchA_{eff}} - \frac{1}{\tau 1}$$
$$m_{25} = \frac{\sigma_{s,a}\lambda_s S^{ss}}{cchA_{eff}}(N_{t,a} - N_{1,a}^{ss} - N_{2,a}^{ss}) - \frac{\sigma_{s,e}\lambda_s S^{ss}}{cchA_{eff}} N_{1,a}^{ss}$$
$$m_{33} = -\frac{1}{\tau 2} - \frac{\sigma_{p,a}\lambda_p P_{in}}{cchA_{eff}}$$
$$m_{34} = -\frac{\sigma_{p,a}\lambda_p P_{in}}{cchA_{eff}}$$
$$m_{43} = \frac{1}{\tau 2} - \frac{\sigma_{s,a}\lambda_s S^{ss}}{cchA_{eff}}$$
$$m_{44} = -\frac{\sigma_{s,a}\lambda_s S^{ss}}{cchA_{eff}} - \frac{\sigma_{s,e}\lambda_s S^{ss}}{cchA_{eff}} - \frac{1}{\tau 1 q}$$
$$m_{45} = \frac{\sigma_{s,a}\lambda_s S^{ss}}{cchA_{eff}}(N_{t,q} - N_{1,q}^{ss} - N_{2,q}^{ss}) - \frac{\sigma_{s,e}\lambda_s S^{ss}}{cchA_{eff}} N_{1,q}^{ss}$$
$$m_{51} = v_g \frac{\sigma_{s,a}\lambda_s S^{ss}}{cchA_{eff}}$$
$$m_{52} = v_g(\frac{\sigma_{s,a}\lambda_s S^{ss}}{cchA_{eff}} + \frac{\sigma_{s,e}\lambda_s S^{ss}}{cchA_{eff}})$$
$$m_{53} = v_g \frac{\sigma_{s,a}\lambda_s S^{ss}}{cchA_{eff}}$$
$$m_{54} = v_g(\frac{\sigma_{s,a}\lambda_s S^{ss}}{cchA_{eff}} + \frac{\sigma_{s,e}\lambda_s S^{ss}}{cchA_{eff}})$$
$$m_{55} = v_g(-\alpha + \sigma_{s,e}(N_{1,a}^{ss} + N_{1,q}^{ss}) - \sigma_{s,a}(N_{t,a} - N_{1,a}^{ss} - N_{2,a}^{ss} + N_{t,q} - N_{1,q}^{ss} - N_{2,q}^{ss}))$$

Note that time-variations of steady-state values were set to zero and $N_{0,a}^{ss} + \Delta N_{0,a}$ was replaced with $N_{t,a} - N_{1,a}^{ss} - \Delta N_{1,a} - N_{2,a}^{ss} - \Delta N_{2,a}$ (similarly for quenched term).

Now, assuming the vector $\begin{bmatrix} \Delta N_{2,a} \\ \Delta N_{1,a} \\ \Delta N_{2,q} \\ \Delta N_{1,q} \\ \Delta S \end{bmatrix}$ changes in time as $\begin{bmatrix} \Delta N_{2,a_0} \\ \Delta N_{1,a_0} \\ \Delta N_{2,q_0} \\ \Delta N_{1,q_0} \\ \Delta S_0 \end{bmatrix} e^{\lambda t}$, the latter term can be substituted into (A.36) to give an expression as $\lambda \begin{bmatrix} \Delta N_{2,a_0} \\ \Delta N_{1,a_0} \\ \Delta N_{2,q_0} \\ \Delta N_{1,q_0} \\ \Delta S_0 \end{bmatrix} = \mathbf{M} \begin{bmatrix} \Delta N_{2,a_0} \\ \Delta N_{1,a_0} \\ \Delta N_{2,q_0} \\ \Delta N_{1,q_0} \\ \Delta S_0 \end{bmatrix}$. λ is thus simply the eigenvalue of $\mathbf{M}$. If the real part of the eigenvalue is positive, the perturbations grow, and the system is unstable. If the real part of the eigenvalue is negative, the perturbations decay, and the system is stable.

Bibliography

[1] Http://www.intel.com/content/www/us/en/architecture-and-technology/silicon-photonics/silicon-photonics-overview.html.

[2] Https://www-03.ibm.com/press/us/en/pressrelease/46839.wss.

[3] W. Bogaerts, P. De Heyn, T. Van Vaerenbergh, K. De Vos, S. K. Selvaraja, T. Claes, P. Dumon, P. Bienstman, D. Van Thourhout, and R. Baets, "Silicon microring resonators," Laser & Photonics Reviews **6**, 47–73 (2012).

[4] R. Soref, "Mid-infrared photonics in silicon and germanium," Nature Photonics **4**, 495–497 (2010).

[5] J. Leuthold, C. Koos, and W. Freude, "Nonlinear silicon photonics," Nature Photonics **4**, 535–544 (2010).

[6] G. Roelkens, L. Liu, D. Liang, R. Jones, A. Fang, B. Koch, and J. Bowers, "Iii-v/silicon photonics for on-chip and inter-chip optical interconnects," Laser & Photonics Reviews **4**, 751–779 (2010).

[7] Http://www.darpa.mil/program/dahi-electronic-photonic-heterogenous-integration.

[8] Http://www.darpa.mil/program/direct-on-chip-digital-optical-synthesizer.

[9] G. T. Reed, "Silicon photonics: the state of the art pages," Wiley pp. 147–189 (2008).

[10] R. E. Camacho-Aguilera, Y. Cai, N. Patel, J. T. Bessette, M. Romagnoli, L. C. Kimerling, and J. Michel, "An electrically pumped germanium laser," Optics Express **20**, 11316–11320 (2012).

[11] H. Park, A. W. Fang, S. Kodama, and J. E. Bowers, "Hybrid silicon evanescent laser fabricated with a silicon waveguide and iii-v offset quantum well," Optics Express **13**, 9460–9464 (2005).

[12] O. Boyraz and B. Jalali, "Demonstration of a silicon raman laser," Optics Express **12**, 5269–5273 (2004).

[13] J. D. B. Bradley, L. Agazzi, D. Geskus, F. Ay, K. Worhoff, and M. Pollnau, "Gain bandwidth of 80 nm and 2 db/cm peak gain in al2o3:er3+ optical amplifiers on silicon," Journal of the Optical Society of America B-Optical Physics **27**, 187–196 (2010).

[14] C. H. Henry, "Theory of the linewidth of semiconductor-lasers," Ieee Journal of Quantum Electronics **18**, 259–264 (1982). Henry, ch.

[15] A. W. Fang, H. Park, O. Cohen, R. Jones, M. J. Paniccia, and J. E. Bowers, "Electrically pumped hybrid algainas-silicon evanescent laser," Optics Express **14**, 9203–9210 (2006).

[16] J. D. B. Bradley, R. Stoffer, L. Agazzi, F. Ay, K. Worhoff, and M. Pollnau, "Integrated al2o3:er3+ ring lasers on silicon with wide wavelength selectivity," Optics Letters **35**, 73–75 (2010).

[17] E. H. Bernhardi, H. A. G. M. van Wolferen, L. Agazzi, M. R. H. Khan, C. G. H. Roeloffzen, K. Worhoff, M. Pollnau, and R. M. de Ridder, "Ultra-narrow-linewidth, single-frequency distributed feedback waveguide laser in al2o3:er3+ on silicon," Optics Letters **35**, 2394–2396 (2010).

[18] K. Worhoff, J. D. B. Bradley, F. Ay, D. Geskus, T. P. Blauwendraat, and M. Pollnau, "Reliable low-cost fabrication of low-loss al2o3:er3+ waveguides with 5.4-db optical gain," Ieee Journal of Quantum Electronics **45**, 454–461 (2009).

[19] L. Agazzi, E. H. Bernhardi, K. Worhoff, and M. Pollnau, "Impact of luminescence quenching on relaxation-oscillation frequency in solid-state lasers," Applied Physics Letters **100** (2012).

[20] D. Coolbaugh, T. Adam, G. Leake, P. Nguyen, and L. Pautler, "Integrated silicon photonics fabrication on a 300 mm platform," Chipscale Magazine May-June (2013).

[21] Y. Okawachi, K. Saha, J. S. Levy, Y. H. Wen, M. Lipson, and A. L. Gaeta, "Octave-spanning frequency comb generation in a silicon nitride chip," Optics Letters **36**, 3398–3400 (2011).

[22] J. D. B. Bradley, E. S. Hosseini, Purnawirman, Z. Su, T. N. Adam, G. Leake, D. Coolbaugh, and M. R. Watts, "Monolithic erbium- and ytterbium-doped microring lasers on silicon chips," Optics Express **22**, 12226–12237 (2014).

[23] Purnawirman, J. Sun, T. N. Adam, G. Leake, D. Coolbaugh, J. D. B. Bradley, E. S. Hosseini, and M. R. Watts, "C- and l-band erbium-doped waveguide lasers with wafer-scale silicon nitride cavities," Optics Letters **38**, 1760–1762 (2013).

[24] Z. Su, N. Li, E. S. Magden, M. Byrd, Purnawirman, T. N. Adam, G. Leake, D. Coolbaugh, J. D. B. Bradley, and M. R. Watts, "Ultra-compact and low-threshold thulium microcavity lasermonolithically integrated on silicon," Opt. Lett. **41**, 5708–5711 (2016).

[25] J. Orcutt and F. Purnawirman, "Continuous evanescent perturbation gratings in a silicon photonic device," (2016). US Patent App. 14/744,740.

[26] Purnawirman, E. S. Hosseini, A. Baldycheva, J. Sun, J. D. B. Bradley, T. N. Adam, G. Leake, D. Coolbaugh, M. R. Watts, and Ieee, "Erbium-doped laser with multi-segmented silicon nitride structure," 2014 Optical Fiber Communications Conference and Exhibition (Ofc) (2014).

[27] H. Kogelnik and C. V. Shank, "Coupled-wave theory of distributed feedback lasers," Journal of Applied Physics **43**, 2327 (1972).

[28] S. Keyvaninia, S. Verstuyft, L. Van Landschoot, F. Lelarge, G. H. Duan, S. Messaoudene, J. M. Fedeli, T. De Vries, B. Smalbrugge, E. J. Geluk, J. Bolk, M. Smit, G. Morthier, D. Van Thourhout, and G. Roelkens, "Heterogeneously integrated iii-v/silicon distributed feedback lasers," Optics Letters **38**, 5434–5437 (2013).

[29] P. Horak and W. H. Loh, "On the delayed self-heterodyne interferometric technique for determining the linewidth of fiber lasers," Opt. Express **14**, 3923–3928 (2006).

[30] K. Kikuchi and T. Okoshi, "Dependence of semiconductor laser linewidth on measurement time: evidence of predominance of 1/f noise," Electronics Letters **21**, 1011–1012 (1985).

[31] L. B. Mercer, "1/f frequency noise effects on self-heterodyne linewidth measurements," Journal of Lightwave Technology **9**, 485–493 (1991).

[32] E. Bernhardi, "Bragg-grating-based rare-earth-ion-doped channel waveguide lasers and their applications," Ph.D. thesis, University of Twente (2012).

[33] T. Okoshi, K. Kikuchi, and A. Nakayama, "Novel method for high resolution measurement of laser output spectrum," Electronics Letters **16**, 630–631 (1980).

[34] H. Tsuchida, "Simple technique for improving the resolution of the delayed self-heterodyne method," Opt. Lett. **15**, 640–642 (1990).

[35] M. Okai, "Spectral characteristics of distributed feedback semiconductor lasers and their improvements by corrugationpitchmodulated structure," Journal of Applied Physics **75**, 1–29 (1994).

[36] H. Abe, S. G. Ayling, J. H. Marsh, R. M. D. L. Rue, and J. S. Roberts, "Single-mode operation of a surface grating distributed feedback gaas-algaas laser with variable-width waveguide," IEEE Photonics Technology Letters **7**, 452–454 (1995).

[37] K. Tada, Y. Nakano, and A. Ushirokawa, "Proposal of a distributed feedback laser with nonuniform stripe width for complete single-mode oscillation," Electronics Letters **20**, 82–84 (1984).

[38] T. E. Murphy, "Design, Fabrication and Measurement of Integrated Bragg Grating Optical Filters," Ph.D. thesis, Massachusetts Institute of Technology (2001).

[39] Z. Li, I. Shubin, and X. Zhou, "Optical interconnects: recent advances and future challenges," Opt. Express **23**, 3717–3720 (2015).

[40] M. J. R. Heck, J. F. Bauters, M. L. Davenport, J. K. Doylend, S. Jain, G. Kurczveil, S. Srinivasan, Y. Tang, and J. E. Bowers, "Hybrid silicon photonic integrated circuit technology," IEEE Journal of Selected Topics in Quantum Electronics **19**, 6100117–6100117 (2013).

[41] L. Stampoulidis, K. Vyrsokinos, K. Voigt, L. Zimmermann, F. Gomez-Agis, H. J. S. Dorren, Z. Sheng, D. Van Thourhout, L. Moerl, J. Kreissl, B. Sedighi, J. C. Scheytt, A. Pagano, and E. Riccardi, "The european boom project: Silicon photonics for high-capacity optical packet routers," Ieee Journal of Selected Topics in Quantum Electronics **16**, 1422–1433 (2010).

[42] A. Alduino, "Demonstration of a high speed 4-channel integrated silicon photonics wdm link with hybrid silicon lasers," 2010 IEEE Hot Chips 22 Symposium (HCS) pp. 1–29 (2010).

[43] S. S. Sui, M. Y. Tang, Y. D. Yang, J. L. Xiao, Y. Du, and Y. Z. Huang, "Sixteen-wavelength hybrid algainas/si microdisk laser array," IEEE Journal of Quantum Electronics **51**, 1–8 (2015).

[44] S. Tanaka, S. H. Jeong, S. Sekiguchi, T. Akiyama, T. Kurahashi, Y. Tanaka, and K. Morito, "Four-wavelength silicon hybrid laser array with ring-resonator based mirror for efficient cwdm transmitter," 2013 Optical Fiber Communication Conference and Exposition and the National Fiber Optic Engineers Conference pp. 1–3 (2013).

[45] G. Kurczveil, M. J. R. Heck, J. D. Peters, J. M. Garcia, D. Spencer, and J. E. Bowers, "An integrated hybrid silicon multiwavelength awg laser," IEEE Journal of Selected Topics in Quantum Electronics **17**, 1521–1527 (2011).

[46] L. Tao, L. Yuan, Y. Li, H. Yu, B. Wang, Q. Kan, W. Chen, J. Pan, G. Ran, and W. Wang, "4-λ ingaasp-si distributed feedback evanescent lasers with varying silicon waveguide width," Opt. Express **22**, 5448–5454 (2014).

[47] M. Belt and D. J. Blumenthal, "Erbium-doped waveguide dbr and dfb laser arrays integrated within an ultra-low-loss si3n4 platform," Opt. Express **22**, 10655–10660 (2014).

[48] B. R. Koch, E. J. Norberg, B. Kim, J. Hutchinson, J. H. Shin, G. Fish, and A. Fang, "Integrated silicon photonic laser sources for telecom and datacom," 2013 Optical Fiber Communication Conference and Exposition and the National Fiber Optic Engineers Conference pp. 1–3 (2013).

[49] S. Tanaka, S.-H. Jeong, S. Sekiguchi, T. Kurahashi, Y. Tanaka, and K. Morito, "High-output-power, single-wavelength silicon hybrid laser using precise flip-chip bonding technology," Opt. Express **20**, 28057–28069 (2012).

[50] T. Creazzo, E. Marchena, S. B. Krasulick, P. K. L. Yu, D. V. Orden, J. Y. Spann, C. C. Blivin, L. He, H. Cai, J. M. Dallesasse, R. J. Stone, and A. Mizrahi, "Integrated tunable cmos laser," Opt. Express **21**, 28048–28053 (2013).

[51] F. F. Lupi, D. Navarro-Urrios, J. Rubio-Garcia, J. Monserrat, C. Dominguez, P. Pellegrino, and B. Garrido, "Visible light emitting si-rich si3n4μ-disk resonators for sensoristic applications," J. Lightwave Technol. **30**, 169–174 (2012).

[52] A. H. J. Yang, S. D. Moore, B. S. Schmidt, M. Klug, M. Lipson, and D. Erickson, "Optical manipulation of nanoparticles and biomolecules in sub-wavelength slot waveguides," Nature **457**, 71–75 (2009). 10.1038/nature07593.

[53] D. K. Armani, T. J. Kippenberg, S. M. Spillane, and K. J. Vahala, "Ultra-high-q toroid microcavity on a chip," Nature **421**, 925–928 (2003). 10.1038/nature01371.

[54] M. Borselli, T. J. Johnson, and O. Painter, "Beyond the rayleigh scattering limit in high-q silicon microdisks: theory and experiment," Opt. Express **13**, 1515–1530 (2005).

[55] T. J. Kippenberg, J. Kalkman, A. Polman, and K. J. Vahala, "Demonstration of an erbium-doped microdisk laser on a silicon chip," Physical Review A **74** (2006).

[56] H.-S. Hsu, C. Cai, and A. M. Armani, "Ultra-low-threshold er:yb sol-gel microlaser on silicon," Optics Express **17**, 23265–23271 (2009).

[57] A. J. Maker and A. M. Armani, "Nanowatt threshold, alumina sensitized neodymium laser integrated on silicon," Optics Express **21**, 27238–27245 (2013).

[58] D. S. Gardner and M. L. Brongersma, "Microring and microdisk optical resonators using silicon nanocrystals and erbium prepared using silicon technology," Optical Materials **27**, 804–811 (2005).

[59] D. W. Prather, B. Redding, T. Creazzo, E. Marchena, and S. Shi, "Integration of silicon nanocrystals and erbium ring cavities for a silicon pumped er:sio2 laser," Journal of Nanoscience and Nanotechnology **10**, 1643–1649 (2010).

[60] J. S. Chang, S. C. Eom, G. Y. Sung, and J. H. Shin, "On-chip, planar integration of er doped silicon-rich silicon nitride microdisk with su-8 waveguide with submicron gap control," Optics Express **17**, 22918–22924 (2009).

[61] M. Ghulinyan, R. Guider, G. Pucker, and L. Pavesi, "Monolithic whispering-gallery mode resonators with vertically coupled integrated bus waveguides," Ieee Photonics Technology Letters **23**, 1166–1168 (2011).

[62] Z. Su, "Advanced Silicon Photonic Microcavities for Routing, Detection and Lasing Application," Ph.D. thesis, Massachusetts Institute of Technology (2016).

[63] G. N. van den Hoven, R. Koper, A. Polman, C. vanDam, J. W. M. vanUffelen, and M. K. Smit, "Net optical gain at 1.53 mu m in er-doped al2o3 waveguides on silicon," Applied Physics Letters **68**, 1886–1888 (1996).

[64] E. P. Ostby and K. J. Vahala, "Yb-doped glass microcavity laser operation in water," Optics Letters **34**, 1153–1155 (2009).

[65] L. He, S. K. Oezdemir, J. Zhu, W. Kim, and L. Yang, "Detecting single viruses and nanoparticles using whispering gallery microlasers," Nature Nanotechnology **6**, 428–432 (2011).

[66] L. Agazzi, K. Worhoff, and M. Pollnau, "Energy-transfer-upconversion models, their applicability and breakdown in the presence of spectroscopically distinct ion classes: A case study in amorphous al2o3:er3+," Journal of Physical Chemistry C **117**, 6759–6776 (2013).

[67] G. Singh, Purnawirman, J. D. B. Bradley, N. Li, E. S. Magden, M. Moresco, T. N. Adam, G. Leake, D. Coolbaugh, and M. R. Watts, "Resonant pumped erbium-doped waveguide lasers using distributed bragg reflector cavities," Opt. Lett. **41**, 1189–1192 (2016).

[68] H. A. Haus, "Waves and fields in optoelectronics," Prentice-Hall pp. 197–234 (1984).